CORA Cork Open Research Archive
Cartlann Taighde Oscailte Chorcaí

Title	Mathematical aspects of internal wave-current interactions
Authors	McCarney, Jordan
Publication date	2026-05-06
Original Citation	McCarney, J. 2026. Mathematical aspects of internal wave-current interactions. PhD Thesis, University College Cork.
Type of publication	Doctoral thesis
Rights	© 2026, Jordan McCarney. - https://creativecommons.org/licenses/by/4.0/
Download date	2026-11-07 11:31:30
Item downloaded from	https://hdl.handle.net/10468/19316

UCC
University College Cork, Ireland
Coláiste na hOllscoile Corcaigh

Ollscoil na hÉireann, Corcaigh

National University of Ireland, Cork

Mathematical Aspects of Internal Wave-Current Interactions

Thesis presented by

Jordan McCarney

for the degree of

Doctor of Philosophy

University College Cork

School of Mathematical Sciences

Head of School: Dr Martin Kilian

Supervisor: Dr David Henry

2026

Contents

Declaration iii

Acknowledgments iv

Abstract vi

List of publications vii

List of figures ix

Introduction x

1 Preliminaries 1

1.1 Internal gravity waves 1

1.2 Governing equations 2

1.2.1 Conservation of mass 2

1.2.2 Conservation of momentum 3

1.2.3 Thermodynamics for atmospheric mountain waves 3

1.3 The Lagrangian framework and Gerstner's solution 5

1.3.1 The Lagrangian perspective 5

1.3.2 Gerstner's wave 7

2 Exact internal waves in the presence of zonal currents and the Earth's rotation 8

2.1 Governing equations 9

2.2 The hydrostatic model 13

2.2.1 Boundary conditions 13

2.2.2 The exact solution 14

2.2.3 Solution of the dispersion relation 20

2.2.4 Linear analysis 23

2.2.5 Global diffeomorphism of the Lagrangian flow-map 26

2.3 The nonhydrostatic model 31

2.3.1 Boundary conditions 31
2.3.2 The exact solution 33
2.3.3 Perturbative analysis of the dispersion relation 40

3 Temperature dependent precipitation in exact nonlinear mountain waves 44
3.1 Governing equations 47
3.2 Thermodynamics of moist air 48
3.3 Explicit flow dynamics 50
3.3.1 The laminar flow layer 50
3.3.2 The dispersion relation and pressure distribution 52
3.4 Saturated air flows 53
3.5 Linear temperature-dependent enthalpy 54
3.5.1 Saturation temperature and pressure distributions 55
3.5.2 Adiabatic cooling to saturation 57
3.5.3 Precipitation as a heat change within the flow 59
3.5.4 Real world example - *Feldberg, Germany* 61
3.5.5 Entropy in a saturated atmosphere 63
3.5.6 Dry air flows 64
3.6 Nonlinear temperature-dependent enthalpy 67
3.6.1 Precipitation in nonlinear mountain waves 69
3.6.2 Entropy 70
3.6.3 Dew-point temperature in the flow 72
3.6.4 Deposition 74

4 Flow underlying coupled surface and internal waves with lower layer vorticity 76
4.1 Equations of motion 77
4.2 Linearisation of the equations 80
4.3 Travelling wave solutions 82
4.4 Dispersion relation 84
4.5 Phase plane analysis 87
4.5.1 Lower layer 88
4.5.2 Upper layer 94
4.6 Physical particle trajectories 99
4.6.1 Lower layer 101
4.6.2 Upper layer 105

5 Conclusions and future work 110

Declaration

This is to certify that the work I am submitting is my own and has not been submitted for another degree, either at University College Cork or elsewhere. All external references and sources are clearly acknowledged and identified within the contents. I have read and understood the regulations of University College Cork concerning plagiarism and intellectual property.

Signature of the candidate:

Jordan McCarney

May, 2026

Acknowledgments

First and foremost, I would like to thank my supervisor Dr David Henry for the boundless support, patience and guidance he has given me over the course of my doctoral studies. I have been fortunate enough to benefit from your vast mathematical knowledge and expertise, and have gained so much from all of the time that you have so generously afforded me. I am sure that these past few years have been as taxing and thankless for you as they have been enjoyable and enriching for me. So thank you for everything, I really appreciate it.

I would like to thank Dr Tony Lyons and Dr Daniel Devine for their time and the many insightful conversations during our collaborations together on projects during my studies. I learned a great deal working with you both and I hope that we may work together again in the future.

I would like to thank Prof. Rossen Ivanov in Technological University of Dublin for so generously sharing his time and wisdom with me throughout the years.

Thank you to everyone in the School of Mathematical Sciences for all of the help you have given me during this time, for the many delightful corridor conversations, and for making my time as a postgraduate student such a pleasant one. A special thank you to Dr Martin Kilian for providing many kind words of advice.

Thank you to each of my fellow postgraduate students who have passed through the research office over this time, however briefly, for all of the interesting discussions and for sharing their time and knowledge so willingly. To David and Frank who were there for the early years, Fergal in his brief cameo, and Ruaraí throughout, thank you for making the office such a great place to be.

I have been very fortunate to travel often during my studies and I would like to take the opportunity to thank Prof. Adrian Constantin for his kind hospitality during my visit to the Erwin Schrödinger Institute in Vienna in May 2023. I

would also like to thank Prof. Joachim Escher and Dr Luigi Roberti for extending such a warm welcome during my visit to Leibniz Universität Hannover in November 2025.

Thank you to Mikey, Ash, Pádraig, Niall, Béibhinn, Sam and Lu, for being such great friends. If the people make the place, then Cork has been really special.

Thank you to Colm, Audrey and Lauren for all of your hospitality throughout the years, and for always making me feel at home.

To my parents, Mark and Catherine, for all that you have done for me. All of the opportunities that I have been fortunate enough to have had, have been because of you and your endless love and support. I hope you know how much I have appreciated it, thank you both for everything.

To my siblings, Sam, Ollie, Paddy and Pierce, I was blessed to be the youngest and to have always had each of you to look up to. Whatever good qualities that I may have, I learned them all from you.

To Ciara, for whom words can't adequately express how thankful I am, and who has been with me through it all. I hope that these past few years have been just as wonderful for you, as you keep making them for me.

Thank you to Dr Bogdan-Vasile Matioc and Dr Ben McKay for their careful examination of this thesis and for their useful suggestions to improve it.

This work was supported by Taighde Éireann - Research Ireland (formerly Science Foundation Ireland), under the grant number SFI 21/FFP-A/9150.

Abstract

In this thesis we study various aspects of the mathematical theory of internal wave-current interactions in both the ocean and the atmosphere. In Chapter 2 we construct exact, nonlinear, three-dimensional solutions in Lagrangian coordinates describing internal ocean waves propagating on zonal currents in the presence of the Earth's rotation. In Chapter 3 we extend a recent exact nonlinear solution for vertically propagating mountain waves to incorporate the thermodynamics of a moist atmosphere and the the latent heat released during phase transitions of water vapour. Finally, in Chapter 4 we study coupled surface and internal small-amplitude water waves in a two-layer fluid with constant vorticity in the lower layer and an irrotational upper layer, and present results concerning particle trajectories.

Publications associated with this thesis

The following publications arose from the work presented in this thesis.

(i) McCarney, J., Exact internal waves in the presence of mean currents and rotation, *Journal of Mathematical Physics*, **64** 073101, 2023.

(ii) McCarney, J., Nonhydrostatic internal waves in the presence of mean currents and rotation, *Journal of Mathematical Physics*, **65** 043101, 2024.

(iii) Lyons, T., McCarney, J., Temperature dependent precipitation in exact nonlinear mountain waves, *Journal of Mathematical Fluid Mechanics*, **27** 41, 2025.

(iv) Lyons, T., McCarney, J., Nonlinear temperature dependent enthalpies in exact nonlinear mountain waves, *Differential and Integral Equations*, **39** 7-8, 2026.

The following manuscript is in an advanced stage of preparation.

(v) Devine, D., McCarney, J., Flow underlying coupled surface and internal water waves with a rotational lower layer.

List of Figures

1.1 Schematic of a Gerstner wave 7

2.1 Locally Cartesian coordinate system on a rotating Earth 10
2.2 Schematic of a stably stratified, hydrostatic ocean model with a zonal current 13
2.3 Particle trajectories in the (y, z)-plane for Pollard-like internal waves at different latitudes 15
2.4 Schematic of a stably stratified, nonhydrostatic ocean model with a zonal current and a series of transitional fluid layers beneath the thermocline 32
2.5 Plot of the dispersion relation $P(X)$, illustrating the existence of four real roots 41

3.1 A lenticular cloud formation above Croagh Patrick, Ireland 47
3.2 Particle paths for exact, vertically propagating mountain waves . 51
3.3 Comparison of the saturation temperature profile derived from a linear enthalpy with Bolton's approximation 58
3.4 Surface plot demarcating the region in which precipitation is thermodynamically admissible 66
3.5 Contour plot delineating the region where precipitation is thermodynamically admissible 67
3.6 Particle trajectories in the physical domain, indicating regions where precipitation is admissible 68
3.7 Comparison of three approximations for the saturation temperature profile 70
3.8 Estimated dew-point temperature and vapour pressure profiles . . 73

4.1 Schematic of a stably stratified two-layer fluid model in in-phase and out-of-phase configurations 84
4.2 Dispersion relation $\mathcal{P}(c) = 0$, irrotational case $(\gamma = 0)$ 86
4.3 Dispersion relation $\mathcal{P}(\mathfrak{c}) = 0$, rotational case $(\gamma \neq 0)$ 87

4.4 Phase portrait for the lower-fluid layer, $\gamma \leq 0$ 91
4.5 Phase portrait for the lower-fluid layer, $\gamma > 0$ 93
4.6 Phase portrait for the lower-fluid layer, $\gamma > 0$, $\mathfrak{c} < 0$ 94
4.7 Phase portrait for the upper-fluid layer, $A < 1$ 96
4.8 Phase portrait for the upper-fluid layer, $A < 1$, $\mathfrak{c} < 0$ 97
4.9 Phase portrait for the upper-fluid layer, $A = 1$ 98
4.10 Phase portrait for the upper-fluid layer, $A > 1$ 100
4.11 Particle trajectory with forward drift 104
4.12 Closed particle trajectories the lower layer arising from large negative vorticity 105
4.13 Particle trajectories for $A > 1$, $kh_1 > \overline{Y}_1$ 107

Introduction

In this thesis we study various aspects of the mathematical theory of internal wave-current interactions in both the ocean and the atmosphere.

In Chapter 2 we present exact, nonlinear, three-dimensional Gerstner-like solutions to the governing equations for geophysical ocean flows, modelling internal waves propagating on zonal currents in the presence of the Earth's rotation. Working in Lagrangian coordinates, solutions are constructed for two stably stratified ocean models of varying sophistication: a hydrostatic model in which the fluid below the internal interface is taken to be motionless, and a nonhydrostatic model incorporating transitional layers beneath the internal interface through which particle velocities decay with depth to a still deep-water region. In both cases, the oscillation of the thermocline is parameterised explicitly, and the resulting dispersion relations are subjected to perturbative analysis, revealing two distinct modes of wave motion. We also prove that the Lagrangian flow map is a global diffeomorphism in the hydrostatic setting, and therefore the flow is dynamically possible.

In Chapter 3 we extend a recently-derived exact nonlinear solution for vertically propagating mountain waves to incorporate the thermodynamics of a moist atmosphere and the release of latent heat during phase transitions of water vapour to liquid and ice. We exploit the kinematic detail afforded by the Lagrangian description to derive an integral representation of the atmospheric pressure distribution in terms of the temperature profile within a prescribed laminar flow layer, and by imposing compatibility between this pressure distribution and the Clausius-Clapeyron equation we obtain an explicit description of the saturation temperature and vapour pressure throughout a deduced saturated domain. In the first part of this chapter we consider a linear temperature-dependence for the enthalpy of vapourisation and use the resulting framework to compute precipitation rates which we compare with meteorological field data. In the second part of the chapter we extend the analysis by considering a nonlinear enthalpy of vapourisation, which achieves greater accuracy across meteorologically relevant temperatures, and we derive the corresponding saturation temperature, dew-point tem-

perature and vapour pressure distributions throughout the troposphere. In both cases, applying the second law of thermodynamics and accounting for the contributions of thermal diffusion and latent heat due to condensation, we establish the existence of an implicit curve in the Lagrangian labelling domain which demarcates the upper boundary of the precipitating region within the troposphere. In the final part of the chapter we model the phase transition of deposition as a mechanism for snowfall formation using a highly nonlinear approximation for the temperature-dependent enthalpy.

Finally, in Chapter 4 we study the flow induced by coupled surface and internal small-amplitude water waves in a stably stratified two layer fluid model in which the lower layer has a constant, non-zero vorticity and the upper layer is irrotational. We obtain a detailed Eulerian description of the underlying flow through a phase-plane approach, and establish the qualitative motion of individual fluid particles through a Lagrangian analysis of the appropriate nonlinear dynamical systems.

Chapter 1

Preliminaries

1.1 Internal gravity waves

Internal gravity waves propagate within the interior of a density-stratified fluid and owe their existence to the restoring force generated when a fluid parcel is displaced vertically from its neutral buoyancy level. In the ocean, stratification arises primarily from gradients in temperature and salinity, which combine to produce a density profile that typically increases with depth. The sharpest density gradient is concentrated in a relatively thin layer known as the pycnocline, or the thermocline when the density variation is driven principally by temperature. It is along this interface that internal waves are most prominently supported, and it is the oscillation of the thermocline that provides the physical setting for the theoretical work of Chapters 2 and 4 in this thesis.

Internal waves play a fundamental role in any meaningful description of large-scale ocean dynamics, contributing centrally to the mixing that sustains the meridional overturning circulation and to the vertical transport of heat, momentum, and nutrients. The existence of waves at the interface between fluids of differing densities has been recognised since the nineteenth century, with an early theoretical treatment due to Stokes [102]. Their physical significance was first observed in the scientific literature by Nansen during the *Fram* expedition of 1893-96, in which ships moving through stratified polar waters experienced an anomalous resistance now known as 'dead-water'. Ekman subsequently identified the cause of this drag as being due to the generation of internal waves along a shallow pycnocline [37]. Advances in observational oceanography have since established that internal waves are ubiquitous features of the world's oceans, generated by mechanisms including the interaction of tides with submarine topography, wind forcing at the sea surface, and pressure fluctuations. However, internal waves remain inherently difficult to observe and measure due to their na-

ture and location, highlighting the relevance of pursuing theoretical investigations into their motion.

In the atmosphere, stable stratification is established by a density profile that decreases with altitude sufficiently rapidly to provide a buoyant restoring force on vertically displaced air parcels. An example of internal gravity waves in this setting is the forcing of stratified air over orography, that is when a stratified airstream encounters a mountain range, the air parcels are forced upwards by the topography, and the resulting buoyancy oscillations propagate away from the obstacle as mountain waves. It is this setting that provides the physical motivation for the theoretical work of Chapter 3.

1.2 Governing equations

The flows studied throughout this thesis, both in the ocean and in the atmosphere, are modelled as inviscid fluids, and are governed by the classical conservation laws of mass and momentum. We will now briefly review these governing equations in the form in which they will be used, and highlight the key distinctions between the oceanic and atmospheric settings.

1.2.1 Conservation of mass

For a fluid of density $\rho = \rho(x, y, z, t)$ and velocity field $\mathbf{u} = (u, v, w)$, conservation of mass is expressed by the continuity equation

$$\frac{\partial \rho}{\partial t} + \nabla \cdot (\rho \mathbf{u}) = 0, \tag{1.1}$$

which states that the rate of change of density within any fluid element is balanced by the net flux of mass through its boundary. Equivalently, (1.1) can be rewritten in terms of the material derivative as

$$\frac{D\rho}{Dt} + \rho \nabla \cdot \mathbf{u} = 0,$$

where

$$\frac{D}{Dt} = \frac{\partial}{\partial t} + \mathbf{u} \cdot \nabla \tag{1.2}$$

denotes the rate of change of a quantity following a fluid particle along its trajectory.

For the ocean flows considered in this thesis, the fluid is treated as incompressible, meaning the density of a given fluid parcel remains constant along its trajectory, and thus $D\rho/Dt = 0$. In this case (1.1) reduces to the requirement

that the velocity field be divergence-free:

$$\nabla \cdot \mathbf{u} = 0. \tag{1.3}$$

For atmospheric flows, incompressibility is not generally a physically realistic assumption, since significant density variations accompany the large vertical extent of the atmosphere and the associated changes in pressure and temperature. The full compressible form (1.1) must therefore be retained in principle. However, as we shall see in Chapter 3, the Gerstner-like Lagrangian prescription used to construct exact solutions for atmospheric mountain waves turns out to impose (1.3) as a structural consequence of the parameterisation, so that the resulting flows are incompressible even in the atmospheric setting.

1.2.2 Conservation of momentum

In the absence of viscosity, conservation of momentum is expressed by the Euler equations

$$\frac{D\mathbf{u}}{Dt} = -\frac{1}{\rho}\nabla P + \mathbf{g}, \tag{1.4}$$

where P denotes the pressure and $\mathbf{g}$ the gravitational acceleration; a detailed derivation can be found in any fluid dynamics textbook, see for example [4, 63]. In a frame of reference rotating with the Earth, (1.4) must be supplemented by the Coriolis force arising from the non-inertial nature of the rotating reference frame, leading to the geophysical Euler equations used Chapter 2. The precise form of the rotating Euler equations, along with the f-plane approximation employed to render the analysis tractable at fixed latitudes, will be introduced once it is required.

1.2.3 Thermodynamics for atmospheric mountain waves

For the incompressible ocean flows considered in Chapters 2 and 4, the system (1.3), (1.4), supplemented by appropriate boundary conditions, relevant physical modifications and a prescription for the stratified density distribution, is sufficient to determine the flow. In the atmospheric setting, however, the retention of compressibility in the governing equations introduces the density ρ as an additional unknown, and further relations are required to fully determine the system.

The first of these is the equation of state. Under typical atmospheric conditions, dry air behaves to good approximation as an ideal gas, so that

$$P = \rho R_d T, \tag{1.5}$$

where T is the absolute temperature and $R_d \approx 287\,\mathrm{J\,kg^{-1}\,K^{-1}}$ is the specific gas constant for dry air. The treatment of moist air in Chapter 3 introduces a modified temperature variable, known as the virtual temperature, that recasts the equation of state for moist air in a form identical to (1.5), see for example [107].

The equation of state (1.5) introduces an additional unknown in the temperature T, and thus requires a further equation to close the system. This is provided by the first law of thermodynamics, which expresses conservation of energy for a fluid parcel and relates the material rates of change of temperature and pressure to a net heating rate $\dot{Q}$

$$\frac{DT}{Dt} - \frac{\mu}{\rho}\frac{DP}{Dt} = \dot{Q}, \tag{1.6}$$

where $\mu = R_d/C_p \approx 0.287$ and $C_p \approx 1000\,\mathrm{J\,kg^{-1}\,K^{-1}}$ is the specific heat capacity of dry air at constant pressure, see [4, 41]. In the adiabatic setting, considered prior to the onset of saturation, $\dot{Q} = 0$ and (1.6) reduces to a statement of the reversible exchange between thermal and mechanical energy within a rising air parcel. The explicit form of $\dot{Q}$ in the presence of phase transitions will be introduced in Chapter 3.

A distinguishing feature of the atmospheric flows studied in this thesis is the role played by phase transitions of water. Rain forms when water vapour condenses into liquid, and one possible mechanism for the formation of snow is the direct deposition of water vapour to form ice. Such transitions are accompanied by the release of latent heat, quantified by an enthalpy function ΔH which contributes to the heating rate $\dot{Q}$. The enthalpy also governs the equilibrium between the vapour and condensed phases of water at saturation, through the Clausius–Clapeyron equation

$$\frac{1}{e_s}\frac{de_s}{dT} = \frac{\Delta H}{T^2}, \tag{1.7}$$

which relates the saturation vapour pressure e_s to the temperature T. A more comprehensive exposition on the first law of thermodynamics and the Clausius-Clapeyron equation can be found in many textbooks that cover thermodynamics, and particualr examples in the context of the atmosphere include [1, 29, 41]. Together with the pressure distribution derived directly from the kinematics of the flow, (1.7) provides the key link between the wave solution and its thermodynamic state.

Taken together, the continuity equation (1.1), the Euler equations (1.4), the equation of state (1.5), and the first law of thermodynamics (1.6) fully determine the atmospheric flows considered in this thesis in the absence of phase changes.

The thermodynamic processes of precipitation and deposition occurring within these flows are then characterised by the Clausius–Clapeyron equation (1.7), together with entropy considerations arising from the second law of thermodynamics.

1.3 The Lagrangian framework and Gerstner's solution

The exact solutions considered in Chapters 2 and 3 of this thesis are formulated in a Lagrangian rather than Eulerian framework, and take as their common starting point the classical wave solution of Gerstner [40], while in Chapter 4 the qualitative motion of particle trajectories is uncovered by pursuing a Lagrangian analysis of the dynamical systems governing the flow. In this section we briefly review the Lagrangian description of fluid motion and introduce Gerstner's solution.

1.3.1 The Lagrangian perspective

In the Eulerian description outlined in Section 1.2, the velocity field $\mathbf{u}(\mathbf{x}, t)$ gives the velocity of the fluid particle instantaneously occupying the spatial location $\mathbf{x}$ at time t. In the Lagrangian description, by contrast, individual fluid particles are each labelled uniquely by a set of time-independent labelling variables $\mathbf{q} = (q, r, s)$, and the flow is specified by prescribing the flow map

$$\mathbf{x} = \mathbf{X}(\mathbf{q}, t), \tag{1.8}$$

which gives the spatial position at time t of the particle labelled $\mathbf{q}$. Differentiating with respect to time at fixed label yields the velocity of the particle,

$$\mathbf{V}(\mathbf{q}, t) = \left.\frac{\partial \mathbf{X}}{\partial t}\right|_{\mathbf{q}},$$

and its acceleration follows similarly as $\partial^2\mathbf{X}/\partial t^2$ at fixed $\mathbf{q}$. The material derivative, which in the Eulerian description takes the form (1.2), therefore reduces in the Lagrangian description to a simple partial derivative with respect to time at fixed label.

The Eulerian and Lagrangian descriptions are related by the flow map (1.8), that is the Eulerian velocity at the spatial location $\mathbf{x} = \mathbf{X}(\mathbf{q}, t)$ and time t coincides with the Lagrangian velocity of the particle labelled $\mathbf{q}$, so that

$$\mathbf{u}\Big(\mathbf{X}(\mathbf{q}, t), t\Big) = \mathbf{V}(\mathbf{q}, t).$$

For the flow to be physically meaningful, the flow map (1.8) is required to be a global diffeomorphism at each time t, which we will discuss in detial for the hydrostatic case in Section 2.2.5. The Jacobian matrix

$$J = \frac{\partial \mathbf{x}}{\partial \mathbf{q}}$$

encodes the deformation of an infinitesimal fluid element as it is transported by the flow, and its determinant $\det J$ quantifies the change in volume. The continuity equation (1.1) takes a particularly simple form in Lagrangian variables. Consider an infinitesimal fluid element labelled by $\mathbf{q} = (q, r, s)$, occupying in label space a small volume $dV_0 = dq\, dr\, ds$. At time t the element has been transported by the flow to the spatial region of volume

$$dV = \det J(\mathbf{q}, t)\, dV_0. \tag{1.9}$$

Evaluating this mass at a time t and a reference time t_0 gives, by the conservation of mass,

$$\rho(\mathbf{q}, t)\, dV(\mathbf{q}, t) = \rho(\mathbf{q}, t_0)\, dV(\mathbf{q}, t_0).$$

Substituting the transport relation (1.9) into the above and canceling the common factor dV_0 yields the Lagrangian form of mass conservation

$$\rho(\mathbf{q}, t)\ \det J(\mathbf{q}, t) = \rho(\mathbf{q}, t_0)\ \det J(\mathbf{q}, t_0), \tag{1.10}$$

valid for any reference time t_0. For incompressible flows, in which the density at a fixed label is constant in time, (1.10) reduces to the requirement that $\det J$ itself be independent of time,

$$\frac{\partial}{\partial t} \det J(\mathbf{q}, t) = 0, \tag{1.11}$$

at a fixed label $\mathbf{q}$. This condition is equivalent to the Eulerian divergence-free condition (1.3) and forms the basis of the incompressibility verification used throughout the exact solution constructions developed in chapters 2 and 3, that is, once a Lagrangian parameterisation of the flow is prescribed, $\det J$ can be computed explicitly, and (1.11) then yields algebraic constraints on the parameters of the prescribed flow. See [5] for a detailed treatment of the Lagrangian formulation of fluid dynamics.

1.3.2 Gerstner's wave

The Lagrangian framework is particularly suited to describe the exact nonlinear solution for wave trains on deep water first put forward by Gerstner in 1802 [40]. The solution presupposes that each particle in the fluid traces out a circular path, and the radii of these circles decrease with depth below the free surface, see Figure 1.1. The Gerstner wave is obtained for Lagrangian labelling variables $\{(a,b) : a \in \mathbb{R}, b \leq b_0\}$ where $b_0 \leq 0$, by specifying at each time t the particle positions

$$x(a,b,t) = a - \frac{1}{k}e^{kb}\sin(k(a-ct))\,, \tag{1.12}$$

$$z(a,b,t) = b + \frac{1}{k}e^{kb}\cos(k(a-ct))\,, \tag{1.13}$$

where $k > 0$ is the wavenumber and $c = \sqrt{g/k}$ is the wave speed which coincides with the classical deep-water dispersion relation. It should be noted that (a,b) is not the initial position of the particle labelled (a,b), it is instead the centre of this particle's circular trajectory. In particular, as time evolves a particle labelled (a_1,b_1) traces out a circle centred at (a_1,b_1) with a radius e^{kb_1}/k in the clockwise direction with an angular speed $\sqrt{gk}$. The free surface corresponds to fixing $b = b_0$ and as b decreases from b_0 the radii of the particle paths decrease exponentially. For $b < 0$, the positions (1.12)–(1.13) parametrise an inverted trochoid and in the limiting case $b_0 = 0$, the free surface is an inverted cycloid. A detailed exposition of Gerstner's solution and its place within the broader theory of water waves is given in [12].

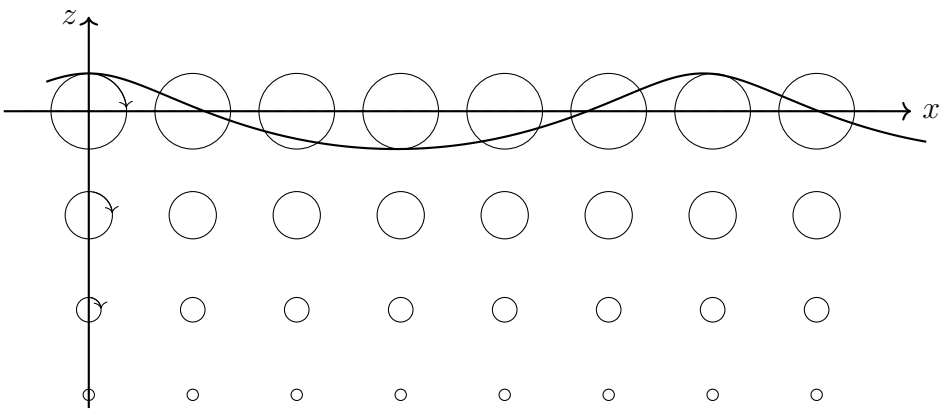

Figure 1.1: Schematic of a Gerstner wave. Each fluid particle traces a closed circular orbit about its undisturbed position, with orbit radii decreasing exponentially with depth. The free surface, shown as the solid curve, is the trochoid traced by the uppermost particles; in the limiting case $b_0 = 0$ it becomes a cycloid with sharp cusps at the crests.

Chapter 2

Exact internal waves in the presence of mean zonal currents and the Earth's rotation

In this chapter we present two exact, nonlinear, three-dimensional Gerstner-like solutions to the governing equations for geophysical ocean flows, both modelling internal ocean waves in the presence of a zonal current and the Earth's rotation. The ocean model under consideration is that of two stably stratified immiscible fluid layers, separated by an oscillating internal interface. The first solution, presented in Section 2.2, employs a hydrostatic model in which the fluid below the thermocline is assumed to be motionless. The second solution, presented in Section 2.3, extends this to a more physically realistic nonhydrostatic model which incorporates a series of transitional layers beneath the thermocline, allowing for a smooth decay in particle velocities from the uniform horizontal speed experienced on the thermocline to a state of rest in the deep-water region. The chapter combines the results of two published works, the hydrostatic results presented in Section 2.2 are based on [85], while the nonhydrostatic results presented in Section 2.3 are based on [86].

The nonlinear equations governing water wave motion are highly intractable, and exact solutions are consequently rare. The two-dimensional nonlinear solution presented by Gerstner [40] in 1802, describing gravity waves with a non-flat free surface, remains the only known explicit solution of its kind. In 1970, Pollard [93] extended this solution to incorporate the effects of the Earth's rotation and the associated Coriolis forces, constructing a nonlinear, three-dimensional solution to the governing equations for geophysical ocean flows. Pollard's solution is given within the f-plane approximation and is therefore valid for arbitrary but approximately fixed latitudes, excluding the poles. Whereas Gerstner waves describe the purely two-dimensional motion of particles in vertical planes, the plan-

etary vorticity present in Pollard-like solutions gives rise to a three-dimensional flow with a cross-wave tilt to particle trajectories, the magnitude of which is proportional to the displacement from the Equator. Pollard-like solutions are therefore particularly suited to describing global flows at latitudes away from the Equator. Instability analyses have been carried out for both Gerstner [18, 39, 62] and Pollard-like [61] waves, while the mass-transport properties of Pollard waves have been investigated in [68]. Furthermore, it was shown in [84] that in the f-plane equatorial deep-water setting, the Gerstner-type waves are characterised as the unique solutions with isobaric streamlines and no stagnation points.

A substantial body of work has employed such explicit solutions to model a variety of ocean flows. Equatorial flows have been studied in [13, 14, 15, 47, 49, 60, 73, 81], while geophysical internal wave solutions have been investigated in [14, 48, 64, 65, 66, 78, 82, 98]. A variety of wave-current interactions have been modelled in [19, 20, 21, 25, 47, 53, 83, 97]. A prominent physical example to which the considerations of this chapter are relevant is the Antarctic Circumpolar Current (ACC), a large-scale ocean flow propagating primarily in an azimuthal direction [22, 44, 79, 80, 95], which possesses many of the salient features described by zonally propagating Pollard-like solutions.

The aim of this chapter is twofold. First, in Section 2.2 we extend the Pollard-like internal wave framework to include a piecewise constant zonal current in a hydrostatic setting, constructing a new exact internal wave solution. A perturbative analysis of the resulting dispersion relation reveals that the incorporation of a zonal current mediates a new type of slow inertial wave motion. Furthermore, this analysis indicates that the existence of such a current is necessary for the vertical amplitude of this wave motion to decay sufficiently with height above the thermocline. Second, in Section 2.3 we extend this hydrostatic model to incorporate nonhydrostatic transitional layers beneath the thermocline, following the approach of [66]. The resulting perturbative analysis shows that the inertial wave modes found in the hydrostatic setting are retained, however the dynamics of the particle trajectories are altered by the presence of the transitional layers, which in particular compel the wave amplitude to decay more rapidly with height above the thermocline.

2.1 Governing equations

The flows being investigated are described with respect to a rotating Cartesian coordinate system that is fixed to the Earth's surface, see Fig 2.1. In this framework we take the zonal coordinate x to point eastwards, the meridional coordinate y to point northwards, and the vertical coordinate z to point upwards locally normal

to the Earth's surface. This reference frame is not inertial so the Coriolis force acts on all particles within the rotating frame of reference. We will now derive the governing equations of motion for geophysical ocean waves following [30, 41].

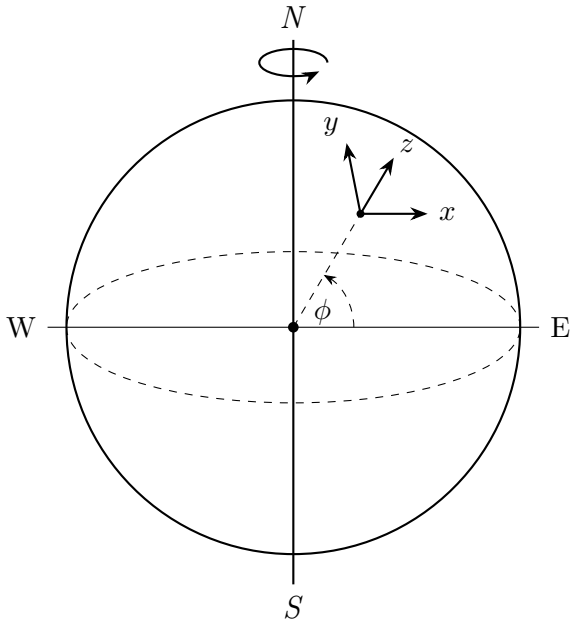

Figure 2.1: A locally Cartesian coordinate system on a rotating, spherical Earth. The x-, y- and z-coordinates are directed eastwards, northwards and vertically upwards respectively, and ϕ denotes latitude.

The Euler equations for an inviscid fluid in a non-rotating (inertial) frame are given by

$$\frac{\partial \boldsymbol{u}_I}{\partial t} + (\boldsymbol{u}_I \cdot \nabla)\, \boldsymbol{u}_I = -\frac{1}{\rho}\nabla P + \boldsymbol{g}^*, \tag{2.1}$$

where t is time, $\boldsymbol{u}_I$ is the fluid velocity measured in the inertial frame, P is pressure, $\boldsymbol{g}^* = (0, 0, -g^*)$ is the Newtonian gravitational acceleration on the Earth's surface, and ρ is the density of the fluid. We let the subscripts I and R refer to time derivatives taken relative to the inertial and rotating frames, respectively. We denote the angular velocity of the rotating reference frame by $\boldsymbol{\Omega}$, directed along the axis of rotation with magnitude $\Omega = 7.29 \times 10^{-5}\,\mathrm{rad\,s^{-1}}$. For any vector $\boldsymbol{A}$, the time derivatives in the inertial and rotating frames are related by

$$\left(\frac{d\boldsymbol{A}}{dt}\right)_I = \left(\frac{d\boldsymbol{A}}{dt}\right)_R + \boldsymbol{\Omega} \times \boldsymbol{A}, \tag{2.2}$$

see [41]. Thus, the motion of a point $\boldsymbol{x}$ with respect to the fixed frame is related to its motion relative to the rotating frame by

$$\left(\frac{d\boldsymbol{x}}{dt}\right)_I = \left(\frac{d\boldsymbol{x}}{dt}\right)_R + \boldsymbol{\Omega} \times \boldsymbol{x},$$

and applying (2.2) a second time we find the acceleration in the fixed frame,

$$\left(\frac{d^2\boldsymbol{x}}{dt^2}\right)_I = \left(\frac{d}{dt}\right)_R \left(\left(\frac{d\boldsymbol{x}}{dt}\right)_R + \boldsymbol{\Omega}\times\boldsymbol{x}\right) + \boldsymbol{\Omega}\times\left(\left(\frac{d\boldsymbol{x}}{dt}\right)_R + \boldsymbol{\Omega}\times\boldsymbol{x}\right)$$

$$= \left(\frac{d^2\boldsymbol{x}}{dt^2}\right)_R + 2\boldsymbol{\Omega}\times\left(\frac{d\boldsymbol{x}}{dt}\right)_R + \boldsymbol{\Omega}\times(\boldsymbol{\Omega}\times\boldsymbol{x})\,. \tag{2.3}$$

Consideration of a non-inertial reference frame invariably leads to the introduction of fictitious forces, which arise due to the acceleration of the observer's frame of reference. The second and third terms on the right-hand side of (2.3) are the Coriolis acceleration and the centripetal acceleration, respectively. The centripetal term can be rewritten as the gradient of a scalar field,

$$-\boldsymbol{\Omega}\times(\boldsymbol{\Omega}\times\boldsymbol{x}) = \nabla\left(\frac{1}{2}|\boldsymbol{\Omega}\times\boldsymbol{x}|^2\right),$$

allowing (2.3) to be rewritten as

$$\left(\frac{d\boldsymbol{u}_I}{dt}\right)_I = \left(\frac{d\boldsymbol{u}_R}{dt}\right)_R + 2\boldsymbol{\Omega}\times\boldsymbol{u}_R - \nabla\left(\frac{1}{2}|\boldsymbol{\Omega}\times\boldsymbol{x}|^2\right).$$

By interpreting $\boldsymbol{x}$ as a material fluid volume element, the time derivative $\frac{d}{dt}$ coincides with the material derivative $\frac{D}{Dt} = \frac{\partial}{\partial t} + \boldsymbol{u}\cdot\nabla$ (see [5]), and we can rewrite (2.1) as

$$\frac{D\boldsymbol{u}_R}{Dt} + 2\boldsymbol{\Omega}\times\boldsymbol{u}_R - \nabla\left(\frac{1}{2}|\boldsymbol{\Omega}\times\boldsymbol{x}|^2\right) = -\frac{1}{\rho}\nabla P - \nabla\Phi^*,$$

where $\boldsymbol{g}^* = -\nabla\Phi^*$. We now define the effective gravity

$$\boldsymbol{g} \coloneqq \boldsymbol{g}^* + \nabla\left(\frac{1}{2}|\boldsymbol{\Omega}\times\boldsymbol{x}|^2\right), \tag{2.4}$$

which represents the gravitational acceleration measured on the Earth's surface. Due to the centrifugal contribution, $\boldsymbol{g}$ varies slightly with latitude, and its equipotential surfaces define the geoid, that is the true shape of the Earth, rather than a perfect sphere. In what follows, we adopt the common simplifying approximation of a spherical Earth, under which we neglect this latitudinal variation of its shape and treat gravity as pointing purely in the vertical direction, $\boldsymbol{g} = (0, 0, -g)$ with $g = 9.81$ ms^{-2} constant. This is equivalent to neglecting the centrifugal correction in (2.4) and, consequently, the small oblateness of the geoid. Substituting into the rotating-frame momentum equation and dropping the subscript R, we

obtain the Euler equations in the rotating frame

$$\frac{D\boldsymbol{u}}{Dt} + 2\boldsymbol{\Omega} \times \boldsymbol{u} = -\frac{1}{\rho}\nabla P + \boldsymbol{g}. \tag{2.5}$$

In this locally Cartesian framework, the vector representing the Earth's rotation is given by

$$\boldsymbol{\Omega} = (0, \Omega\cos\phi, \Omega\sin\phi)\,,$$

where ϕ denotes latitude. We are now in a position to rewrite the momentum equations (2.5) in this rotating reference frame as

$$\begin{aligned} u_t + uu_x + vu_y + wu_z + 2\Omega w\cos\phi - 2\Omega v\sin\phi &= -\frac{1}{\rho}P_x, \\ v_t + uv_x + vv_y + wv_z + 2\Omega u\sin\phi &= -\frac{1}{\rho}P_y, \\ w_t + uw_x + vw_y + ww_z - 2\Omega u\cos\phi &= -\frac{1}{\rho}P_z - g. \end{aligned} \tag{2.6}$$

Introducing the Coriolis parameters,

$$f = 2\Omega\sin\phi, \quad \hat{f} = 2\Omega\cos\phi,$$

and adopting the f-plane approximation, we restrict the analysis to narrow bands of latitude where f and $\hat{f}$ can be taken as constant, allowing (2.6) to be rewritten as

$$\begin{aligned} P_x &= -\rho\left[\frac{Du}{Dt} + \hat{f}w - fv\right], \\ P_y &= -\rho\left[\frac{Dv}{Dt} + fu\right], \\ P_z &= -\rho\left[\frac{Dw}{Dt} - \hat{f}u + g\right]. \end{aligned} \tag{2.7}$$

The governing equations include the condition of incompressibility

$$\nabla\cdot\boldsymbol{u} = u_x + v_y + w_z = 0, \tag{2.8}$$

and the equation of mass conservation

$$\frac{D\rho}{Dt} = \rho_t + u\rho_x + v\rho_y + w\rho_z = 0. \tag{2.9}$$

2.2 The hydrostatic model

2.2.1 Boundary conditions

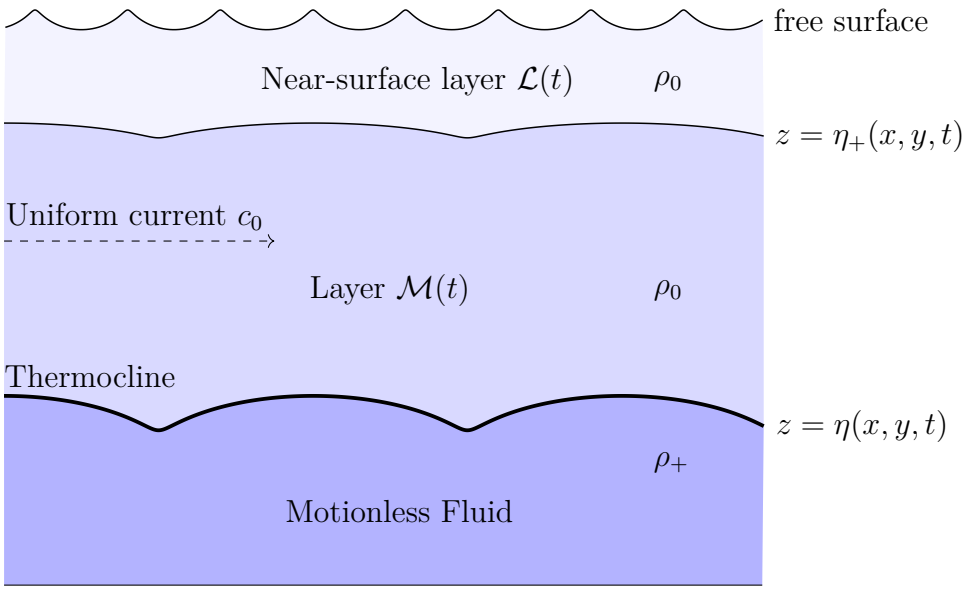

Figure 2.2: Schematic of a stably stratified, hydrostatic two-layer ocean model with an underlying uniform zonal current in the layer $\mathcal{M}(t)$, cf. [64].

For the hydrostatic setting, the solution that we construct models an internal wave describing the oscillation of a thermocline separating fluid layers of different densities within the ocean. We assume that the fluid is stably stratified with $\rho_0 < \rho_+$. The fluid below the thermocline, which is denoted by $z = \eta(x, y, t)$, has density ρ_+ and is assumed to be motionless. That is, $(u, v, w) = (0, 0, 0)$ for all $z < \eta(x, y, t)$. Above the thermocline the fluid has density ρ_0, and is further subdivided into two layers, $\mathcal{M}(t)$ and $\mathcal{L}(t)$. The near-surface layer $\mathcal{L}(t)$ is the layer to which wind driven motion is confined, and the dynamics of which are not addressed in this thesis. A typical value [14] in the mid-Pacific for the mean depth of this layer is 80m. Below this is the layer $\mathcal{M}(t)$, which is the region in which the fluid motion is entirely dictated by zonally propagating waves. A typical depth for the thermocline in the mid-Pacific is 120m below the free surface. The fact that the fluid is motionless below the thermocline gives rise by way of the Euler equations to a natural boundary condition,

$$P = P_0 - \rho_+ g z \quad \text{on the thermocline } z = \eta(x, y, t), \tag{2.10}$$

for some constant P_0. We also assume that no mixing occurs between the motionless region and the layer $\mathcal{M}(t)$, that is, a particle on the boundary stays on

the boundary for all time. This restriction gives rise to the kinematic boundary condition

$$w = \eta_t + u\eta_x + v\eta_y \quad \text{on the thermocline } z = \eta(x, y, t). \tag{2.11}$$

No mixing between the layers ensures that (2.9) holds in each layer as this two-layer ocean model is stably stratified by two regions of differing but constant densities.

2.2.2 The exact solution

In this section we present an exact solution to the governing equations for the internal water waves in the layer $\mathcal{M}(t)$ in the presence of a depth-invariant mean current. Here, we present a parametrisation for the particle paths that we will show is an explicit solution to the equations (2.7) - (2.11). It is convenient to prescribe the solution in terms of the Lagrangian labelling variables (q, r, s), time t and the real parameters a, b, c, d, k, m, c_0, as follows:

$$\begin{aligned} x &= q - be^{-ms}\sin[k(q - ct)] - c_0 t, \\ y &= r - de^{-ms}\cos[k(q - ct)], \\ z &= s - ae^{-ms}\cos[k(q - ct)], \end{aligned} \tag{2.12}$$

where the Lagrangian variables are given by

$$(q, r, s) \in \mathbb{R} \times [-r_0, r_0] \times [s_0(r), s_+(r)],$$

with r_0 chosen to satisfy the constraints imposed by the $f-$plane approximation and where $s = s_0(r) \geq s^* > 0$ represents the thermocline and $s = s_+(r) > s_0(r)$ represents the interface between the layers $\mathcal{M}(t)$ and $\mathcal{L}(t)$. The vertical amplitude of the internal wave, its wavenumber and the mean current velocity are given by $a > 0$, $k > 0$ and c_0 respectively, and we restrict $m > 0$ to ensure that the amplitude of the wave decreases exponentially with height above the thermocline. In seeking to prove that (2.12) is a solution to the governing equations we uncover relations that determine the values of the real parameters b, d, c in terms of a, k, m.

The advantage of the explicit Lagrangian formulation (2.12) is that, despite the fully nonlinear nature of the governing equations, the particle trajectories can be read off directly from the prescribed parametrisation. Obtaining such explicit kinematic information is non-trivial even in the linear setting, where considerable effort is required to determine the trajectories that particles follow [54, 55]. That the Pollard-like framework affords the same directness of access to particle trajec-

tories in the fully nonlinear regime is therefore a significant feature of the solution (2.12). The prescription on the position of particles (2.12), is a parametrisation of a wave propagating zonally, with crests parallel to the meridional direction and with the particles moving in trochoidal orbits [25]. Anticipating relation (2.18) derived below, $d = {}^{-bf}/_{kc}$, gives insight into the particle trajectories. Here, $d < 0$ in the Northern Hemisphere, $d > 0$ in the Southern Hemisphere and $d = 0$ on the Equator. In particular, where Gerstner-like solutions describe two-dimensional circular trajectories in the vertical plane, an interesting feature of Pollard-like solutions is that the particles paths are three-dimensional and acquire a tilt in the meridional direction. For internal waves this inclination is at an angle of $\alpha = \arctan({}^{-d}/_{a})$, such that the top of the particles' path is closer to the Equator, see Figure 2.3, whereas for surface waves the top of the particles' path is closer to the pole of the respective hemisphere in which the particle resides, cf. [25, 60, 65, 93]. We now seek to verify that (2.12) is a solution to the governing

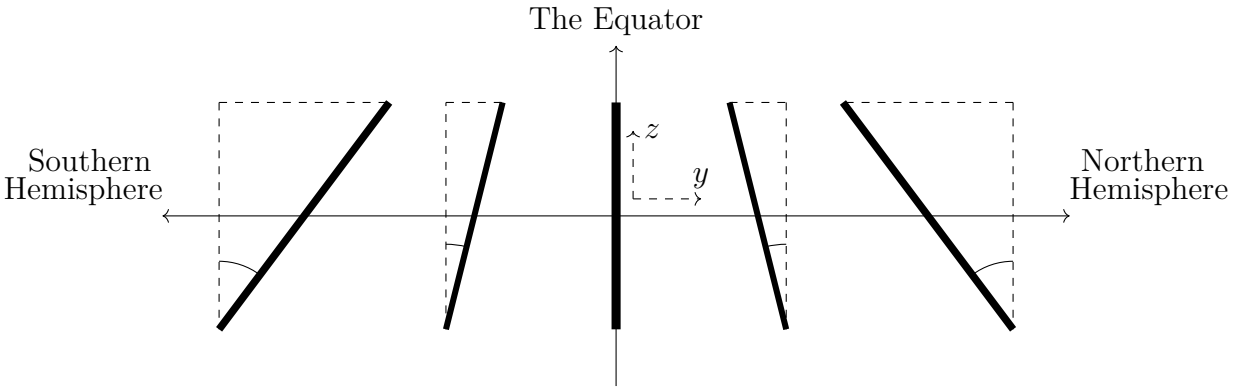

Figure 2.3: Projection of particle trajectories onto the (y, z)-plane for Pollard-like internal waves at different latitudes, at a representative depth $z = z_0$. The inclination relative to the vertical grows with distance from the Equator, cf. [65].

equations. For convenience in what follows we let

$$\theta = k\,(q - ct)\,.$$

The mapping from the particles position in our rotating Cartesian reference frame to the Lagrangian labelling variables has transposed Jacobian

$$\begin{pmatrix} \dfrac{\partial x}{\partial q} & \dfrac{\partial y}{\partial q} & \dfrac{\partial z}{\partial q} \\ \dfrac{\partial x}{\partial r} & \dfrac{\partial y}{\partial r} & \dfrac{\partial z}{\partial r} \\ \dfrac{\partial x}{\partial s} & \dfrac{\partial y}{\partial s} & \dfrac{\partial z}{\partial s} \end{pmatrix} = \begin{pmatrix} 1 - kbe^{-ms}\cos\theta & kde^{-ms}\sin\theta & kae^{-ms}\sin\theta \\ 0 & 1 & 0 \\ mbe^{-ms}\sin\theta & mde^{-ms}\cos\theta & 1 + mae^{-ms}\cos\theta \end{pmatrix} \tag{2.13}$$

with determinant

$$J = 1 + (am - bk)e^{-ms}\cos\theta - kmabe^{-2ms}.$$

The continuity equation (2.8) can be rewritten as $J_t/J = 0$, cf. [12], and so for this flow to be incompressible, the determinant of the Jacobian must be time-independent and non-zero. From this we find that

$$am = bk, \tag{2.14}$$

and

$$ambke^{-2ms} \neq 1. \tag{2.15}$$

The above constraint that $J \neq 0$ ensures that (2.12) is a valid local diffeomorphic change of coordinates by means of the inverse function theorem. Since $s \geq s^* > 0$, and we have that $am = bk$ from (2.14), then

$$a^2m^2e^{-2ms^*} < 1. \tag{2.16}$$

Since ae^{-ms^*} is the vertical amplitude of the internal wave evaluated at the thermocline depth s^*, it follows from (2.15) that there is a natural upper bound on the vertical amplitude, namely $a_{\max} = 1/m$. The velocity and acceleration can be computed directly through differentiation with respect to time of the Lagrangian particle positions stated in the proposed solution (2.12), cf [5], which yields

$$\begin{aligned} u &= \frac{Dx}{Dt} = kcbe^{-ms}\cos\theta - c_0, \\ v &= \frac{Dy}{Dt} = -kcde^{-ms}\sin\theta, \\ w &= \frac{Dz}{Dt} = -kcae^{-ms}\sin\theta, \end{aligned}$$

and

$$\begin{aligned} \frac{Du}{Dt} &= k^2c^2be^{-ms}\sin\theta, \\ \frac{Dv}{Dt} &= k^2c^2de^{-ms}\cos\theta, \\ \frac{Dw}{Dt} &= k^2c^2ae^{-ms}\cos\theta. \end{aligned}$$

Substitution of the above particle velocities and accelerations into (2.7) leads to

the following pressure gradient

$$
\begin{aligned}
P_x &= -\rho_0 \left[kc \left(bkc - a\hat{f} + df \right) e^{-ms} \sin\theta \right], \\
P_y &= -\rho_0 \left[kc \left(dkc + bf \right) e^{-ms} \cos\theta - fc_0 \right], \\
P_z &= -\rho_0 \left[kc \left(akc - \hat{f}b \right) e^{-ms} \cos\theta + \hat{f}c_0 + g \right].
\end{aligned}
$$

The pressure gradient with respect to the Lagrangian labels (q, r, s) is given by the change of variables

$$
\begin{pmatrix} P_q \\ P_r \\ P_s \end{pmatrix} = \begin{pmatrix} \dfrac{\partial x}{\partial q} & \dfrac{\partial y}{\partial q} & \dfrac{\partial z}{\partial q} \\ \dfrac{\partial x}{\partial r} & \dfrac{\partial y}{\partial r} & \dfrac{\partial z}{\partial r} \\ \dfrac{\partial x}{\partial s} & \dfrac{\partial y}{\partial s} & \dfrac{\partial z}{\partial s} \end{pmatrix} \cdot \begin{pmatrix} P_x \\ P_y \\ P_z \end{pmatrix}.
$$

Thus, the pressure gradient with respect to the Lagrangian labelling variables is given by

$$
\begin{aligned}
P_q &= -\rho_0 \Big[k^3 c^2 \left(a^2 + d^2 - b^2 \right) e^{-2ms} \cos\theta \sin\theta \\
&\qquad + (bk^2c^2 - a\hat{f}kc + a\hat{f}kc_0 - dfkc_0 + dkfc + gak) e^{-ms} \sin\theta \Big], \\
P_r &= -\rho_0 \Big[kc \left(dkc + bf \right) e^{-ms} \cos\theta - fc_0 \Big], \\
P_s &= -\rho_0 \Big[\left(ak^2c^2 + \hat{f}amc_0 - fdmc_0 - \hat{f}bkc + gam \right) e^{-ms} \cos\theta \\
&\qquad + mkc(kcb^2 - \hat{f}ab + fbd) e^{-2ms} \\
&\qquad + mk^2c^2(a^2 + d^2 - b^2) e^{-2ms} \cos^2\theta + g + \hat{f}c_0 \Big].
\end{aligned}
\tag{2.17}
$$

Assuming that the pressure in $\mathcal{M}(t)$ is a C^2 function allows for some simplifications. Namely, from $P_{qr} = P_{rq}$ (alternatively, the same relation can be found from $P_{sr} = P_{rs}$), it is found that

$$
dkc + bf = 0. \tag{2.18}
$$

While $P_{qs} = P_{sq}$ gives the relation

$$
mkc^2 b + mcdf = k^2 c^2 a. \tag{2.19}
$$

The pressure is found to be

$$P(q,r,s) = \widetilde{P}_0 - \rho_0 \Big[-fc_0 r + \left(g + \hat{f}c_0\right) s - \frac{1}{2}\left(b^2k^2c^2 - \hat{f}abkc + fbdkc\right) e^{-2ms} \\ - (bkc^2 - a\hat{f}c + a\hat{f}c_0 - dfc_0 + dfc + ga) e^{-ms}\cos\theta \\ - \frac{1}{2}k^2c^2\left(a^2 + d^2 - b^2\right) e^{-2ms}\cos^2\theta \Big], \tag{2.20}$$

as the gradient of this pressure distribution is exactly that found above for (P_q, P_r, P_s). Notice that the dynamic boundary condition (2.10) is given by

$$P = P_0 - \rho_+ g\left(s_0 - ae^{-ms_0}\cos\theta\right) \quad \text{on the thermocline,} \tag{2.21}$$

and so for the pressure to be continuous on the thermocline, the coefficients of the $\cos\theta$ terms in (2.20) and (2.21) must be equal. That is,

$$\rho_+ ga = \rho_0\left(bkc^2 - a\hat{f}c + a\hat{f}c_0 - dfc_0 + dfc + ga\right). \tag{2.22}$$

Similarly for the $\cos^2\theta$ term, which leads us to the relation

$$a^2 + d^2 - b^2 = 0.$$

The dynamic boundary condition is thus satisfied by defining

$$\widetilde{P}_0 = P_0 - \rho_+ g s_0 + \rho_0\Big[-fc_0 r + \left(g + \hat{f}c_0\right)s_0 - \frac{1}{2}\left(b^2k^2c^2 - \hat{f}abkc + fbdkc\right)e^{-2ms_0}\Big],$$

where the thermocline at a given latitude $s_0(r)$ is obtained by solving the above implicit equation. It is convenient to combine and rewrite the relations (2.14), (2.18) and (2.19) as

$$b = \frac{ma}{k}, \tag{2.23}$$

$$d = \frac{-fma}{k^2c}, \tag{2.24}$$

$$m^2 = \frac{k^4c^2}{(k^2c^2 - f^2)}. \tag{2.25}$$

It is straightforward to verify that the relations (2.23)–(2.25) are mutually consistent with the constraint $a^2 + d^2 = b^2$. Indeed, substitution of (2.23) and (2.24) into this constraint yields

$$a^2\left(1 + \frac{f^2m^2}{k^4c^2}\right) = \frac{m^2a^2}{k^2},$$

which, upon division by $a^2 > 0$ and rearrangement, is equivalent to (2.25). We

note that (2.25) requires $k^2c^2 > f^2$ in order that $m^2 > 0$, and hence that $m \in \mathbb{R}$. This constitutes a physical constraint on the admissible wave parameters: the phase speed c of the wave must satisfy $|c| > {}^{|f|}/_{k}$, that is, the wave must propagate faster than the ratio of the Coriolis parameter to the wavenumber. The equation of continuity of pressure across the thermocline, (2.22), through the use of (2.23)–(2.25), gives rise to the following dispersion relation

$$\rho_0^2 \left[k^2c^3 - f^2(c - c_0)\right]^2 = \left[k^2c^2 - f^2\right] \left[g(\rho_+ - \rho_0) + \rho_0\hat{f}(c - c_0)\right]^2.$$

The above equation can be simplified through the introduction of the reduced gravity coefficient

$$\widetilde{g} = \frac{\rho_+ - \rho_0}{\rho_0} g, \tag{2.26}$$

where a typical value for $\widetilde{g}$ at the Equator is given by 6×10^{-3} ms^{-2} [38], to yield the following dispersion relation

$$\left[k^2c^3 - f^2(c - c_0)\right]^2 = \left[k^2c^2 - f^2\right] \left[\widetilde{g} + \hat{f}(c - c_0)\right]^2. \tag{2.27}$$

For equatorial waves, where

$$f = 0, \quad \hat{f} = 2\Omega,$$

(2.27) reduces to

$$kc^2 - \widetilde{g} - 2\Omega(c - c_0) = 0,$$

with solutions for the wavespeed of

$$c = \frac{\Omega \pm \sqrt{\Omega^2 + k\left(\widetilde{g} - 2\Omega c_0\right)}}{k}. \tag{2.28}$$

In the absence of underlying currents ($c_0 = 0$), (2.28) reduces to

$$c = \frac{\Omega \pm \sqrt{\Omega^2 + \widetilde{g}k}}{k},$$

as found for equatorial internal waves in [59]. At mid-latitudes however, we have $f \neq 0$ and it is convenient to rewrite the dispersion relation (2.27) in terms of the following non-dimensional variables

$$X = c\sqrt{\frac{k}{\widetilde{g}}}, \quad X_0 = c_0\sqrt{\frac{k}{\widetilde{g}}}, \quad \varepsilon = \frac{f}{\sqrt{\widetilde{g}k}}, \quad F = \frac{\hat{f}}{f},$$

which allows (2.27) to be rewritten as

$$\left[X^3 - \varepsilon^2 (X - X_0)\right]^2 - \left[X^2 - \varepsilon^2\right] [1 + \varepsilon F(X - X_0)]^2 = 0.$$

The non-dimensionalised dispersion relation above gives, when expanded out, a polynomial of degree six, $P(X) = 0$ with

$$\begin{aligned} P(X) = X^6 &- \varepsilon^2 \left(2 + F^2\right) X^4 + 2\varepsilon \left[-F + \varepsilon \left(1 + F^2\right) X_0\right] X^3 \\ &+ \left[-1 + 2\varepsilon F X_0 - \varepsilon^2 F^2 X_0^2 + \varepsilon^4 \left(1 + F^2\right)\right] X^2 \\ &+ 2\varepsilon^3 \left[F - \varepsilon \left(1 + F^2\right) X_0\right] X \\ &+ \varepsilon^2 \left[1 - 2\varepsilon F X_0 + \varepsilon^2 \left(1 + F^2\right) X_0^2\right]. \end{aligned} \tag{2.29}$$

2.2.3 Solution of the dispersion relation

We can gain an insight into the dynamics of internal waves in the presence of an underlying current by performing an analysis of the roots of the dispersion relation along the lines of [25]. An approximation of the roots to the polynomial $P(X)$ can be found through a perturbation expansion in the small parameter ε:

$$X = x_0 + \varepsilon x_1 + \varepsilon^2 x_2 + \varepsilon^3 x_3 + ...$$

Substituting the above expansion into (2.29) and collecting like powers of ε together, it is found that at $O(\varepsilon^0)$

$$\left(x_0^6 - x_0^2\right) = 0,$$

and therefore,

$$x_0 \in \{0, \pm 1, \pm i\}.$$

The solutions near to ± 1 correspond to Gerstner waves that are slightly altered by the Earth's rotation. Furthermore, we are only concerned with real solutions, so assuming that $x_0 = 0$ results in the existence of two possible small roots that are produced by the presence of a mean zonal current and are approximately given by

$$X = \pm\varepsilon \left(1 + \frac{\varepsilon^2 X_0^2}{2}\right) + O\left(\varepsilon^4\right), \tag{2.30}$$

which matches the result found in [25]. Analysis of these small roots of the dispersion relation leads to similar results to those found in [25], which are summarised in this section, however in the context of internal waves we have introduced the coefficient of reduced gravity (2.26). The roots (2.30), to $O(\varepsilon^2)$, give a wavespeed

of

$$c \approx \pm \frac{f}{k}, \tag{2.31}$$

which can be used to evaluate the period of the wave as

$$T = \frac{\lambda}{c} \approx \pm \frac{2\pi}{f} = T_i,$$

where T_i is the inertial period of the Earth, and so the wave motion described by (2.30) is an inertial wave. Then, using the correction to X at $O(\varepsilon^3)$ combined with (2.25) gives an expression for the vertical decay scale in the presence of a mean zonal current of

$$m \approx \pm \widetilde{g} \frac{k}{f c_0}. \tag{2.32}$$

If however we assume that there is no current, then we have the standard deep water dispersion relation for internal waves, $c^2 \approx \widetilde{g}/k$, and using (2.25), together with (2.27) yields

$$m \approx \pm \widetilde{g} \frac{k}{\widetilde{g} - \hat{f} c}. \tag{2.33}$$

To compare the decay scales (2.32) and (2.33), we note that since $f = 2\Omega \sin \phi$ and $\hat{f} = 2\Omega \cos \phi$, both Coriolis parameters are proportional to $\Omega = 7.29 \times 10^{-5}$ rad s^{-1}, which is small relative to the reduced gravity $\widetilde{g} \sim O(10^{-2})$ ms^{-2}. In particular, $|\hat{f} c| \ll \widetilde{g}$, so that $\widetilde{g} - \hat{f} c \approx \widetilde{g}$, and similarly $|f c_0| \ll \widetilde{g}$. It follows that

$$\frac{\widetilde{g}}{f c_0} \gg \frac{\widetilde{g}}{\widetilde{g} - \hat{f} c},$$

and hence the decay scale m^{-1} is significantly smaller in the presence of a mean current than without one. In particular, without a mean current the expression (2.33) may become unbounded as $\widetilde{g} \to \hat{f} c$, whereas (2.32) remains finite provided $c_0 \neq 0$. Thus a mean current is necessary for the wave motion governed by (2.30) to possess a finite decay scale, and hence to be physically realisable. The lateral amplitude d can be computed to $O(\varepsilon)$ through the manipulation of (2.24), (2.31) and (2.32),

$$d \approx \pm a \frac{\widetilde{g}}{f c_0}.$$

Similarly, the longitudinal amplitude b can be found through (2.23), (2.24) and (2.31), yielding

$$b \approx \pm a \frac{\widetilde{g}}{f c_0}.$$

Thus, the vertical displacement of a particle undergoing this motion is small compared to its lateral and longitudinal displacement. Recalling also from (2.16) that $a_{max} = 1/m$ gives a maximum value for the lateral (and longitudinal) displacement

of

$$d_{max} \approx \frac{\widetilde{g}}{mfc_0} \approx \frac{1}{k} \quad (\approx b_{max}),$$

through the use of (2.32). At this point we revert to Cartesian coordinates to highlight the independence of the flow on the variable y. The dependence on the flow's velocity with respect to the Cartesian coordinates is given by

$$\frac{\partial(u,v,w)}{\partial(x,y,z)} = \left(\frac{\partial(q,r,s)}{\partial(x,y,z)}\right)\left(\frac{\partial(u,v,w)}{\partial(q,r,s)}\right).$$

The first term on the right-hand side can be found by inverting (2.13), yielding

$$\begin{pmatrix} q_x & r_x & s_x \\ q_y & r_y & s_y \\ q_z & r_z & s_z \end{pmatrix} = \begin{pmatrix} \dfrac{1+ame^{-ms}\cos\theta}{1-a^2m^2e^{-2ms}} & \dfrac{-dke^{-ms}\sin\theta}{1-a^2m^2e^{-2ms}} & \dfrac{-ake^{-ms}\sin\theta}{1-a^2m^2e^{-2ms}} \\ 0 & 1 & 0 \\ \dfrac{-bme^{-ms}\sin\theta}{1-a^2m^2e^{-2ms}} & \dfrac{bmkde^{-2ms}-dme^{-ms}\cos\theta}{1-a^2m^2e^{-2ms}} & \dfrac{1-ame^{-ms}\cos\theta}{1-a^2m^2e^{-2ms}} \end{pmatrix}$$

Utilising the above two equations, we can show that

$$\boldsymbol{u}_y = \mathbf{u}_q q_y + \mathbf{u}_r r_y + \mathbf{u}_s s_y = \mathbf{u}_r$$

and thus the components of the velocity differentiated with respect to y are found to be

$$\boldsymbol{u}_y = (0,0,0), \tag{2.34}$$

and therefore the flow is independent of the meridional displacement y. Also,

$$P_y = P_q q_y + P_r r_y + P_s s_y = P_r$$

which through (2.17) and (2.18), has been found to equal $\rho_0 f c_0$. Therefore,

$$P_y = \rho_0 f c_0,$$

and so the pressure only depends on y in the presence of a mean current, cf. [65], where there is no mean current and the pressure is found to be independent of y.

2.2.4 Linear analysis

The linearised Euler equations for an oceanic flow with an underlying zonally propagating current, i.e. $\boldsymbol{u} = (u - c_0, v, w)$, can be written as

$$\begin{aligned} u_t - c_0 u_x + \hat{f} w - f v &= -\frac{1}{\rho} P_x, \\ v_t - c_0 v_x + f u - f c_0 &= -\frac{1}{\rho} P_y, \\ w_t - c_0 w_x - \hat{f} u + \hat{f} c_0 &= -\frac{1}{\rho} P_z - g. \end{aligned} \tag{2.35}$$

Due to the flows independence on y from (2.34), and because the flow is assumed incompressible, we can introduce a streamfunction $\psi(x, z, t)$ defined by

$$\begin{aligned} u &= \psi_z, \\ w &= -\psi_x. \end{aligned}$$

The kinematic boundary condition (2.11) can be rewritten in terms of the streamfunction as

$$-\psi_x = \eta_t + (u - c_0)\eta_x \quad \text{on } z = \eta(x, y, t),$$

and upon linearisation becomes

$$-\psi_x = \eta_t - c_0 \eta_x \quad \text{on } z = 0. \tag{2.36}$$

We can linearise the dynamic boundary condition (2.10) by taking the gradient of the pressure along the thermocline,

$$\nabla P \cdot \boldsymbol{\tau} = \nabla \left(P_0 - \rho_+ g z \right) \cdot \boldsymbol{\tau} \quad \text{on } z = \eta(x, y, t),$$

where $\boldsymbol{\tau}$ is a vector parallel to the thermocline, which yields the boundary condition

$$P_x + P_z \eta_x = -\rho_+ g \eta_x \quad \text{on } z = \eta(x, y, t).$$

Using (2.35) to substitute for P_x and P_z, and evaluating on the linearised thermocline $z = 0$, the dynamic boundary condition becomes

$$\rho_0 \Big[u_t - c_0 u_x + \hat{f} w - f v + \eta_x \Big(w_t - c_0 w_x - \hat{f} u + \hat{f} c_0 + g \Big) \Big] = \rho_+ g \eta_x \quad \text{on } z = 0,$$

where the right-hand side arises from linearising the dynamic boundary condition (2.10): differentiating $P_0 - \rho_+ g z$ with respect to x along the thermocline and evaluating at $z = 0$ to leading order gives $-\rho_+ g \eta_x$ on the right-hand side, which

after rearrangement contributes $\rho_+ g\eta_x$ to the equation above. Dividing through by ρ_0, using the definition of the reduced gravity coefficient (2.26) and retaining only first-order terms, yields

$$u_t - c_0 u_x + \hat{f}w - fv + c_0\hat{f}\eta_x - \widetilde{g}\eta_x = 0 \quad \text{on } z = 0. \tag{2.37}$$

By taking the z-derivative of the first equation in (2.35), and the x-derivative of the third equation, we can equate the mixed second order partial derivative $P_{xz} = P_{zx}$, to find

$$(\Delta\psi)_t - c_0 (\Delta\psi)_x - fv_z = 0. \tag{2.38}$$

Similarly, equating $P_{xy} = P_{yx}$ from the governing equations (2.35) leads to

$$v_{xt} - c_0 v_{xx} = -f\psi_{xz}. \tag{2.39}$$

By seeking travelling wave solutions of the form

$$\psi = \psi_0 e^{-mz} \cos\left[k\left(x - ct\right)\right],$$
$$v = V_0 e^{-mz} \sin\left[k\left(x - ct\right)\right],$$

and assuming that the thermocline is described by

$$\eta = \eta_0 \cos[k(x - ct)],$$

(2.39) yields

$$V_0 = \frac{-fm}{k\mathfrak{c}}\psi_0, \tag{2.40}$$

and (2.38) reduces to

$$V_0 = \frac{-k\mathfrak{c}\left[m^2 - k^2\right]}{fm}\psi_0, \tag{2.41}$$

where $\mathfrak{c} = c + c_0$. By the ansätze for ψ and η, the kinematic boundary condition (2.36) becomes

$$\psi_0 = \mathfrak{c}\eta_0. \tag{2.42}$$

Rewriting the dynamic boundary condition (2.37), using (2.40) and (2.42), gives rise to the following dispersion relation in the linear regime,

$$mk^2\mathfrak{c}^2 - \hat{f}k^2\mathfrak{c} - f^2 m - \widetilde{g}k^2 = 0. \tag{2.43}$$

Solving the above quadratic for the wave speed relative to the underlying current speed, $\mathfrak{c}$, gives

$$\mathfrak{c} = \frac{\hat{f}}{2m} \pm \sqrt{\frac{\hat{f}^2}{4m^2} + \frac{f^2}{k^2} + \frac{\widetilde{g}}{m}}.$$

Combination of (2.40) with (2.41) yields

$$f^2m^2 = k^2\mathfrak{c}^2\left[m^2 - k^2\right], \tag{2.44}$$

which ensures that $m = k$ for $f = 0$, and so for $f = \hat{f} = c_0 = 0$, we recover $c^2 = \widetilde{g}/k$, which matches the deep water dispersion relation for internal Gerstner waves found in [103]. Multiplying (2.43) by m and utilising (2.44) allows the dispersion relation to be rewritten as

$$\hat{f}\mathfrak{c} = \frac{f^2m^2}{m\left[m^2 - k^2\right]} - \widetilde{g}.$$

Again using (2.44) and squaring both sides, produces the following polynomial of degree four,

$$m^4\left[\widetilde{g}^2k^2 - \hat{f}^2f^2\right] - 2\widetilde{g}f^2k^2m^3 + m^2\left[f^4k^2 - 2\widetilde{g}^2k^4 + \hat{f}^2f^2k^2\right] + 2\widetilde{g}f^2k^4m + \widetilde{g}^2k^6 = 0. \tag{2.45}$$

We can rewrite the above in terms of the following non-dimensional variables,

$$\varepsilon = \frac{f}{\sqrt{\widetilde{g}k}}, \qquad \xi = \frac{m}{k}, \qquad F = \frac{\hat{f}}{f}.$$

It is then possible to rewrite (2.45) as the following quartic polynomial in ξ,

$$\left(1 - \varepsilon^4F^2\right)\xi^4 - 2\varepsilon^2\xi^3 - \left[2 - \varepsilon^4\left(1 + F^2\right)\right]\xi^2 + 2\varepsilon^2\xi + 1 = 0.$$

The authors of [25] showed using the intermediate value theorem that the above polynomial has two positive roots approximately given by $\xi = 1 + {}^{\varepsilon^2}/_2 \pm \varepsilon^3$, and furthermore showed using Viète's formulae that there are no further positive roots. Since $\xi > 0$ for physically relevant solutions, we find that

$$\xi = 1 + \frac{1}{2}\varepsilon^2 + O(\varepsilon^3). \tag{2.46}$$

The equation (2.44) can be rewritten to give the following relation

$$\mathfrak{c}^2 = \frac{\widetilde{g}}{k}\frac{\varepsilon^2\xi^2}{(\xi^2 - 1)},$$

into which substitution of (2.46) yields

$$\mathfrak{c}^2 = \frac{\widetilde{g}}{k}(1 + O(\varepsilon)).$$

The linear analysis can only uncover a slightly altered standard deep water dispersion relation for internal waves that has been adjusted by the Earth's rotation. The slower wave motion governed by (2.30) is an inherently nonlinear occurrence, and is generated by the presence of a uniform zonal current.

2.2.5 Global diffeomorphism of the Lagrangian flow-map

In order to show that the solution (2.12) describing particle motion in the layer $\mathcal{M}(t)$ is dynamically possible, we must show that the map is a global diffeomorphism. To do so, we follow the procedure first presented in [46] and subsequently in [67, 96], and begin by considering the solution at time $t = 0$. The position of particles can then be expressed as a mapping from the Lagrangian labelling domain as

$$(q, r, s) \in \mathcal{D} \to \mathcal{F}(q, r, s) = \begin{bmatrix} q - be^{-ms} \sin kq \\ r - de^{-ms} \cos kq \\ s - ae^{-ms} \cos kq \end{bmatrix},$$

where

$$\mathcal{D} = \{(q, r, s) : q \in \mathbb{R}, r \in (-r_0, r_0), s \in (s_0, s_+)\}. \tag{2.47}$$

Note that the general case $t \geq 0$ can be easily recovered by a change of variables and a linear shift in the x-component as follows

$$\mathcal{F}(q - ct, r, s) + \begin{bmatrix} (c - c_0)t \\ 0 \\ 0 \end{bmatrix}.$$

Furthermore, the y and z-components of the particle displacement are periodic in q with a period $L = {}^{2\pi}/_{k}$, while the x-component is nearly periodic but undergoes a linear translation of L. The diffeomorphic character of the map is not affected by this linear shift and so it suffices to show that if $\mathcal{F}$ is a global diffeomorphism from the domain

$$\mathcal{D}_L = \{(q, r, s) : q \in (0, L), r \in (-r_0, r_0), s \in (s_0, s_+)\}$$

into its image, then so too is $\mathcal{F}$ from the whole domain (2.47) into the interior of $\mathcal{M}(t)$. We will also show that the boundary of the domain is mapped onto the boundary of the physical fluid region $\mathcal{M}(t)$.

Proposition 2.2.1. *If*

$$1 - ame^{-ms} > 0, \tag{2.48}$$

then $\mathcal{F}$ is a local diffeomorphism from $\mathcal{D}_L$ into $\mathcal{F}(\mathcal{D}_L) \subset \mathcal{M}(t)$.

Proof. We begin by directly calculating the Jacobian matrix of $\mathcal{F}$

$$D\mathcal{F}_{(q,r,s)} = \begin{pmatrix} 1 - kbe^{-ms}\cos kq & kde^{-ms}\sin kq & kae^{-ms}\sin kq \\ 0 & 1 & 0 \\ mbe^{-ms}\sin kq & mde^{-ms}\cos kq & 1 + mae^{-ms}\cos kq \end{pmatrix}$$

and the corresponding Jacobian determinant using (2.14) reduces to

$$J = 1 - a^2m^2e^{-2ms} = (1 - ame^{-ms})(1 + ame^{-ms}).$$

Since $a, m, s > 0$ we have $1 + ame^{-ms} > 0$ always, and so $J > 0$ if and only if $1 - ame^{-ms} > 0$. Thus the hypothesis (2.48) ensures that the Jacobian determinant is strictly positive for all $s \geq s^* > 0$. Furthermore, the mapping $\mathcal{F}$ is a continuously differentiable map with a strictly positive Jacobian, and thus by the inverse function theorem $\mathcal{F}$ is a local diffeomorphism from $\mathcal{D}_L$ into its range. □

Proposition 2.2.2. *If*

$$1 - bme^{-ms^*} > 0, \tag{2.49}$$

then $\mathcal{F}$ is globally injective on $\overline{\mathcal{D}}$.

Proof. Consider $\mathcal{F}$ re-expressed in the following form

$$\mathcal{F}(\boldsymbol{q}) = \boldsymbol{q} - \mathcal{G}(\boldsymbol{q}), \tag{2.50}$$

where $\boldsymbol{q} = (q, r, s)$ and $\mathcal{G}(\boldsymbol{q}) = -e^{-ms}(b\sin kq, d\cos kq, a\cos kq)$. We note that $\mathcal{G}$ itself is a continuous differentiable map and that for any convex domain $\mathcal{G}$ satisfies the following inequality (cf. Appendix A in [96])

$$|\mathcal{G}(\boldsymbol{q}) - \mathcal{G}(\tilde{\boldsymbol{q}})|_2 \leq \max_{\tau\in[0,1]} \|D\mathcal{G}_{\tau\boldsymbol{q}+(1-\tau)\tilde{\boldsymbol{q}}}\|_2 \cdot |\boldsymbol{q} - \tilde{\boldsymbol{q}}|_2, \tag{2.51}$$

where $\tilde{\boldsymbol{q}} = (\tilde{q}, \tilde{r}, \tilde{s})$, $D\mathcal{G}_{\tau\boldsymbol{q}+(1-\tau)\tilde{\boldsymbol{q}}}$ is the Jacobian matrix at any point along the line segment connecting points $\boldsymbol{q}$ and $\tilde{\boldsymbol{q}}$, $|\cdot|_2$ is the Euclidean norm in $\mathbb{R}^3$ and $\|\cdot\|_2$ is the operator norm induced by the Euclidean norm and is equivalent to the spectral matrix norm cf. [58]. The spectral norm of an arbitrary $n \times n$ complex matrix M is given by the square root of the largest eigenvalue of the positive semi-definite matrix M^*M, where M^* is the conjugate transpose of M, that is

$$\|M\|_2 = \sqrt{\lambda_{\max}(M^*M)}.$$

The Jacobian matrix of $\mathcal{G}$ is

$$D\mathcal{G}_{\boldsymbol{q}} = e^{-ms}\begin{pmatrix} -kb\cos kq & 0 & mb\sin kq \\ kd\sin kq & 0 & md\cos kq \\ ka\sin kq & 0 & ma\cos kq \end{pmatrix},$$

and so the product of the above matrix and its complex transpose is given by

$$(D\mathcal{G})^*(D\mathcal{G})$$

$$= e^{-2ms}\begin{pmatrix} k^2b^2\cos^2 kq + (a^2+d^2)k^2\sin^2 kq & 0 & (a^2+d^2-b^2)mb\cos kq\sin kq \\ 0 & 0 & 0 \\ (a^2+d^2-b^2)km\cos kq\sin kq & 0 & m^2b^2\sin^2 kq + (a^2+d^2)m^2\cos^2 kq \end{pmatrix}.$$

Recalling relation (2.2.2), this reduces to

$$(D\mathcal{G})^*(D\mathcal{G}) = b^2e^{-2ms}\begin{pmatrix} k^2 & 0 & 0 \\ 0 & 0 & 0 \\ 0 & 0 & m^2 \end{pmatrix}.$$

Relation (2.25) ensures that $m \geq k$, with equality only along the equator, and therefore we find that

$$\lambda_{\max} = b^2m^2e^{-2ms},$$

which leads directly to

$$\|D\mathcal{G}_{\boldsymbol{q}}\|_2 = bme^{-ms}.$$

Consequently,

$$\|D\mathcal{G}_{\tau\boldsymbol{q}+(1-\tau)\tilde{\boldsymbol{q}}}\|_2 = bme^{-m\bar{s}},$$

where $\bar{s}$ is the s-component of the point on the line segment joining $\boldsymbol{q}$ and $\tilde{\boldsymbol{q}}$ that maximises bme^{-ms}. In particular, it follows that $bme^{-m\bar{s}} \leq bme^{-ms*}$. Returning to the inequality (2.51), we have that

$$\begin{aligned} |\mathcal{G}(\boldsymbol{q}) - \mathcal{G}(\tilde{\boldsymbol{q}})|_2 &\leq bme^{-m\bar{s}}|\boldsymbol{q}-\tilde{\boldsymbol{q}}|_2 \\ &\leq bme^{-ms^*}|\boldsymbol{q}-\tilde{\boldsymbol{q}}|_2. \end{aligned}$$

Recalling that the mapping $\mathcal{F}$ was rewritten in the form (2.50), it follows that

$$\begin{aligned}
|\mathcal{F}(\boldsymbol{q}) - \mathcal{F}(\tilde{\boldsymbol{q}})|_2 &= |\boldsymbol{q} - \tilde{\boldsymbol{q}} - \mathcal{G}(\boldsymbol{q}) + \mathcal{G}(\tilde{\boldsymbol{q}})|_2 \\
&= |(\boldsymbol{q} - \tilde{\boldsymbol{q}}) - (\mathcal{G}(\boldsymbol{q}) + \mathcal{G}(\tilde{\boldsymbol{q}}))|_2 \\
&\geq |\boldsymbol{q} - \tilde{\boldsymbol{q}}|_2 - |\mathcal{G}(\boldsymbol{q}) + \mathcal{G}(\tilde{\boldsymbol{q}})|_2 \\
&\geq |\boldsymbol{q} - \tilde{\boldsymbol{q}}|_2 - bme^{-ms^*}|\boldsymbol{q} - \tilde{\boldsymbol{q}}|_2 \\
&= (1 - bme^{-ms^*})|\boldsymbol{q} - \tilde{\boldsymbol{q}}|_2.
\end{aligned}$$

Therefore, assuming that the proposition (2.49) holds, we have deduced the following bound

$$|\boldsymbol{q} - \tilde{\boldsymbol{q}}|_2 \leq \frac{1}{1 - bme^{-ms^*}}|\mathcal{F}(\boldsymbol{q}) - \mathcal{F}(\tilde{\boldsymbol{q}})|_2,$$

and the map is globally injective. □

We now progress to show that $\mathcal{F}$ is a homeomorphism through the use of the Invariance of Domain Theorem, a proof of which can be found in [99].

Theorem 2.2.3 (Invariance of Domain)**.** *If U is an open subset of $\mathbb{R}^n$ and $f : U \to \mathbb{R}^n$ is a continuous one-to-one mapping, then $V \coloneqq f(U)$ is open in $\mathbb{R}^n$ and f is a homeomorphism between U and V.*

This theorem holds for any open set and so the set $\mathcal{F}(\mathcal{D})$ is open.

Theorem 2.2.4. *If $1 - bme^{-ms^*} > 0$ then $\mathcal{F}$ is a global diffeomorphism from $\mathcal{D}$ into the interior fluid region $\mathcal{M}(t)$ and $\mathcal{F}$ maps $\partial\mathcal{D}$ onto the boundary of $\mathcal{M}(t)$.*

Proof. By the proposition (2.49), $\mathcal{F}$ is injective on $\overline{\mathcal{D}}$ provided that $1 - bme^{-ms^*} > 0$. Since $\mathcal{F}$ is continuous and $\overline{\mathcal{D}}$ is compact, the map $\mathcal{F} : \overline{\mathcal{D}} \to \mathcal{F}(\overline{\mathcal{D}})$ is a homeomorphism. Invariance of Domain applied to the open set $\mathcal{D}$ further ensures that $\mathcal{F}(\mathcal{D})$ is open in $\mathbb{R}^3$, so that $\mathcal{F}(\partial\mathcal{D}) = \partial\mathcal{F}(\mathcal{D})$ and $\overline{\mathcal{F}(\mathcal{D})} = \mathcal{F}(\overline{\mathcal{D}})$, and thus the mapping $\mathcal{F}$ onto $\mathcal{M}(t)$ is surjective.

Furthermore, relations (2.14) and (2.25) lead us to the fact that $b \geq a$, and thus if $1 - bme^{-ms^*} > 0$, it immediately follows that $1 - ame^{-ms^*} > 0$ and we have from proposition (2.48) that $\mathcal{F}$ is a bijective local diffeomorphism from the open set $\mathcal{D}$ into the open set $\mathcal{F}(\mathcal{D})$. Therefore, we conclude that $\mathcal{F}$ is a global diffeomorphism. □

As a final point, we note that along with a sufficient condition for $\mathcal{F}$ to be globally injective, we can obtain also the following necessary condition.

Proposition 2.2.5. *If $\mathcal{F}$ is injective, then*

$$bke^{-ms^*} \leq 1. \tag{2.52}$$

Proof. Note that bke^{-ms} is maximised over the domain at $s = s^*$, since $s \geq s^* > 0$ and e^{-ms} is decreasing in s. It therefore suffices to consider the necessary condition at $s = s^*$, which gives the most restrictive constraint on the parameters. Consider the first component of $\mathcal{F}$ and define the following function

$$\mathcal{H}(q) \coloneqq q - be^{-ms} \sin kq,$$

where it is clear that $\mathcal{H}(q)$ is an odd function that satisfies $H(0) = 0$ and

$$\mathcal{H}(q) \to \infty \quad \text{as} \quad q \to \infty.$$

We will prove by contradiction that if the above inequality does not hold, then the nonlinear equation

$$\mathcal{H}(q) = 0 \tag{2.53}$$

has more than one solution. Therefore, we begin by assuming that (2.52) does not hold, that is

$$bke^{-ms} > 1. \tag{2.54}$$

The function $\mathcal{H}(q)$ has a critical point at

$$q = \frac{1}{k} \arccos\left(\frac{1}{bke^{-ms}}\right),$$

which by our assumption (2.54) is well defined. Thus there exists a unique

$$q_0 \in \left(0, \frac{\pi}{2k}\right),$$

such that $\mathcal{H}'(q) = 0$. Furthermore, we can directly calculate

$$\mathcal{H}''(q_0) = k\sqrt{b^2k^2e^{-2ms} - 1}$$

and by our assumption this is strictly positive so we can conclude that q_0 is a local minimum for $\mathcal{H}$. It also follows from our assumption that

$$\mathcal{H}'(0) = 1 - bke^{-ms} < 0,$$

and so $\mathcal{H}(q)$ takes negative values in a neighbourhood to the right of 0, and since $q_0 \in (0, \pi/2k)$ is a minimum of $\mathcal{H}$ we can conclude that

$$\mathcal{H}(q_0) < 0.$$

By Bolzano's theorem, there exists a strictly positive solution of (2.53) to the

right of q_0, which we will denote as ξ. It follows from the fact that $\mathcal{H}$ is odd that $\mathcal{H}(-\xi) = 0$. Returning to the map $\mathcal{F}$ and considering the points

$$\boldsymbol{q}_1 = (\xi, r, s)$$
$$\boldsymbol{q}_2 = (-\xi, r, s),$$

it is clear that

$$\mathcal{F}(\boldsymbol{q}_1) = \mathcal{F}(\boldsymbol{q}_2),$$

and so $\mathcal{F}$ is not injective. We conclude that if $\mathcal{F}$ is injective, then it must be the case that $bke^{-ms} \leq 1$. □

2.3 The nonhydrostatic model

As in the previous section, the model that is to be investigated is that of a stably stratified ocean on a rotating Earth. In this stably stratified configuration, there are two layers of constant but differing densities $\rho_+ > \rho_0$, separated by a thermocline. The thermocline oscillates in the shape of a trochoid, and the internal wave solution presented here represents this oscillation and propagates above the thermocline. This section presents a nonhydrostatic model, which incorporates a transition in particle velocities from the uniform horizontal speed experienced on the thermocline to being motionless as we extend downwards towards the deep-water region. The motion in the layer $\mathcal{M}(t)$ is dictated by zonally propagating waves induced by the oscillation of the thermocline, see Figure 2.4. Since the amplitude of the wave motion decays rapidly above the thermocline, we separate this layer from the near-surface layer $\mathcal{L}(t)$, to which wind-driven motion is confined. The novelty in this nonhydrostatic model compared with the model presented in the previous section and published in [85] is the addition of transitional layers below the layer $\mathcal{M}(t)$. Immediately below the thermocline we introduce a uniform current layer, $\mathcal{U}(t)$, where particles move with a uniform horizontal velocity in the direction of the internal wave propagation. Beneath $\mathcal{U}(t)$ exists the transitional layer $\mathcal{T}(t)$, where the horizontal velocity of particles decreases linearly with depth until the motionless layer $\mathcal{S}(t)$ is reached, where particles are still.

2.3.1 Boundary conditions

The governing equations of motion remain the Euler equations in the rotating frame derived in Section 2.1, namely (2.6), (2.8) and (2.9), supplemented by the f-plane approximation with Coriolis parameters f and $\hat{f}$ as before, and we define

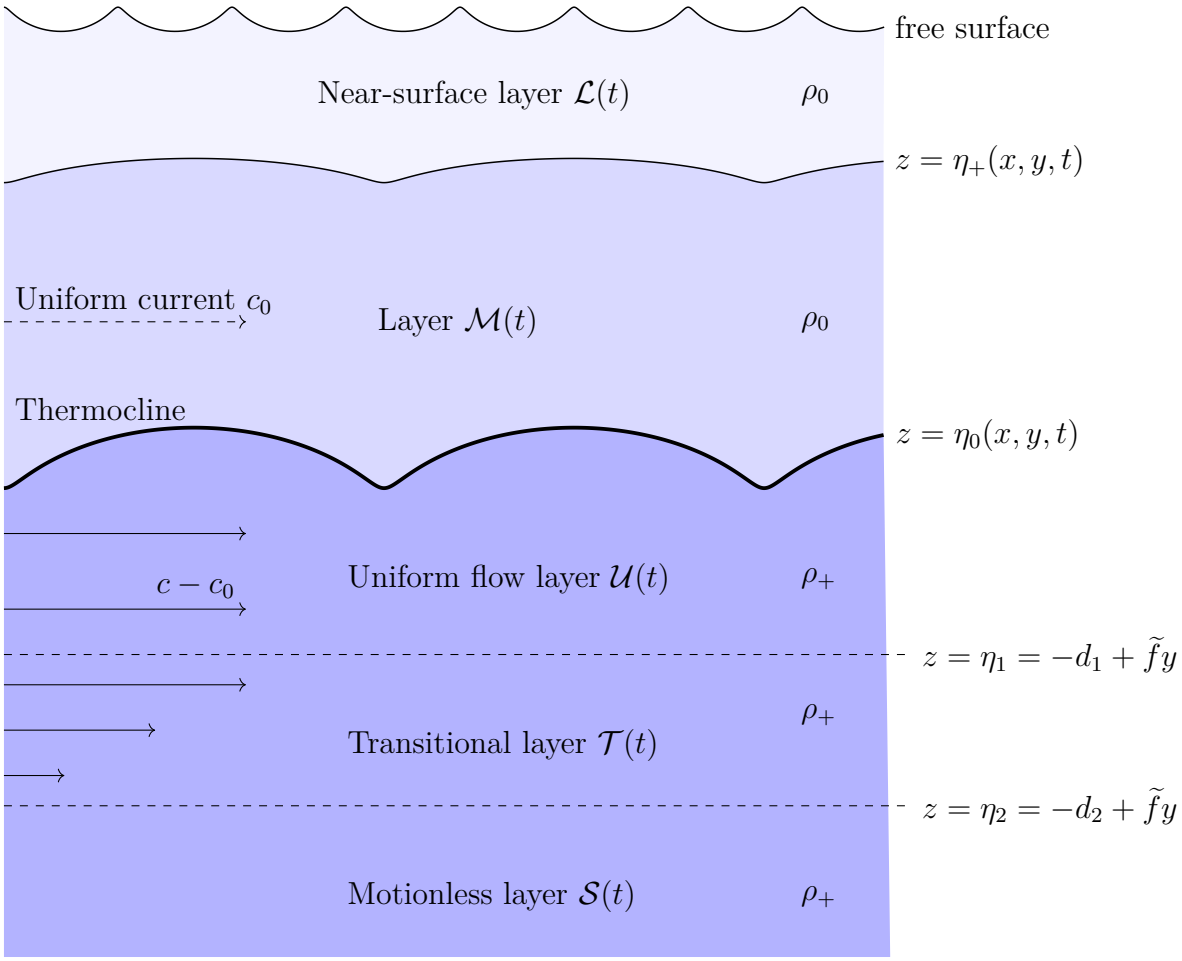

Figure 2.4: Schematic of the nonhydrostatic model at a given latitude. The interface $z = \eta_0(x, y, t)$ represents the thermocline, whose oscillation induces wave motion of wavespeed c in the layer $\mathcal{M}(t)$, which also carries a uniform zonal current c_0. Beneath the thermocline, the layer $\mathcal{U}(t)$ carries a uniform horizontal current, while in the transitional layer $\mathcal{T}(t)$ particle velocities decay linearly with depth to a still deep-water region.

a new quantity

$$\tilde{f} = \frac{f}{\hat{f}} = \tan\phi.$$

For convenience, we rewrite the momentum equations here

$$\begin{aligned} P_x &= -\rho\left[\frac{Du}{Dt} + \hat{f}w - fv\right], \\ P_y &= -\rho\left[\frac{Dv}{Dt} + fu\right], \\ P_z &= -\rho\left[\frac{Dw}{Dt} - \hat{f}u + g\right]. \end{aligned} \tag{2.55}$$

The fluid domain now consists of four distinct layers and at each interface $z = \eta_i(x, y, t)$ for $i = 0, 1, 2$ separating adjacent layers, the solution must satisfy the

following conditions. Continuity of pressure across each interface,

$$[P]_{z=\eta_i} = 0, \quad i = 0, 1, 2,$$

ensures that no impulsive forces act at the layer boundaries. Continuity of the normal component of velocity across each interface,

$$[\boldsymbol{u} \cdot \boldsymbol{n}]_{z=\eta_i} = 0, \quad i = 0, 1, 2,$$

where $\boldsymbol{n}$ denotes the unit normal to the interface, ensures that no fluid crosses the layer boundaries. Finally, to prevent the mixing of particles between layers, we impose the kinematic condition

$$w = \frac{\partial \eta_i}{\partial t} + u\frac{\partial \eta_i}{\partial x} + v\frac{\partial \eta_i}{\partial y} \quad \text{on } z = \eta_i(x, y, t) \quad \text{for } i = 0, 1, 2,$$

and so, particles on the boundary remain on the boundary for all time. The kinematic condition at the thermocline $z = \eta_0$ is satisfied automatically by the Lagrangian structure of (2.56), derived below in Section 2.3.2. Since the thermocline corresponds to the material surface $s = s_0(r)$, which is a fixed label in the Lagrangian framework, every particle initially on the thermocline remains on it for all time. This is equivalent to the statement that

$$\frac{D}{Dt}(z - \eta_0) = 0 \quad \text{on } s = s_0,$$

which is precisely the kinematic boundary condition $w = \eta_{0t} + u\eta_{0x} + v\eta_{0y}$ on $z = \eta_0$.

2.3.2 The exact solution

In this section, we will derive an exact solution describing the motion of particles in the layer $\mathcal{M}(t)$, directly above the thermocline, cf. Figure 2.4. This section is complicated in comparison to Section 2.2, since we now need to ensure that both the normal component of the velocity, as well as the pressure are continuous across the boundaries separating each distinct layer.

The motionless layer $\mathcal{S}(t)$

The upper boundary of the motionless layer, $\mathcal{S}(t)$, is defined as $z = \eta_2 = -d_2 + \widetilde{f}y$, where $d_2 > 0$. The fluid is motionless, thus substitution into the Euler equations

and integrating yields

$$P(x,y,z,t) = P_0 - \rho_+ g z, \qquad z \leq -d_2 + \widetilde{f} y,$$

where P_0 is a constant.

The transitional layer $\mathcal{T}(t)$

The transitional layer $\mathcal{T}(t)$ is bounded below by $z = \eta_2 = -d_2 + \widetilde{f} y$ and above by the boundary

$$z = \eta_1 = -d_1 + \widetilde{f} y,$$

where $d_2 > d_1 > 0$. The dependence of $z = \eta_1$ and $z = \eta_2$ on $\widetilde{f} y$ will become apparent later on, but is necessary for the continuity of pressure across the thermocline, and allows for the thermocline to vary in depth with latitude. This dependence presents itself physically as the boundaries of the transitional layer $\mathcal{T}(t)$ being inclined at an angle of ϕ with respect to the local meridional axis. In this layer, the horizontal component of the particles' velocities increase linearly with height, with the following conditions on the boundaries to ensure continuity across each interface,

$$\begin{aligned} u &= 0 \quad \text{on } z = -d_2 + \widetilde{f} y, \\ u &= c - c_0 \quad \text{on } z = -d_1 + \widetilde{f} y, \end{aligned}$$

leading to the following velocity field

$$(u,v,w) = \left(\frac{c - c_0}{d_2 - d_1} \left(z + d_2 - \widetilde{f} y \right), 0, 0 \right).$$

To find the pressure in the transitional layer, the above velocities are substituted into the governing equations (2.55),

$$P = \frac{1}{2} \rho_+ \hat{f} \frac{c - c_0}{d_2 - d_1} \left(z + d_2 - \widetilde{f} y \right)^2 - \rho_+ g z + P_0.$$

We verify that the pressure is continuous across the interface $z = \eta_2 = -d_2 + \tilde{f} y$. Evaluating the pressure in $\mathcal{T}(t)$ at $z = \eta_2$, we find that $z + d_2 - \tilde{f} y = 0$, and so

$$P\Big|_{z=\eta_2^+} = P_0 - \rho_+ g \eta_2,$$

which coincides with the pressure $P_0 - \rho_+ g z$ in $\mathcal{S}(t)$ evaluated at $z = \eta_2$. Hence $[P]_{z=\eta_2} = 0$. Similarly, the normal velocity condition $[\boldsymbol{u} \cdot \boldsymbol{n}]_{z=\eta_2} = 0$ is verified by

noting that the fluid in $\mathcal{S}(t)$ is motionless, so that $\boldsymbol{u}\Big|_{z=\eta_2^-} = \mathbf{0}$, while the velocity field in $\mathcal{T}(t)$ evaluated at $z = \eta_2$ gives $z + d_2 - \tilde{f}y = 0$, and so $(u, v, w)\Big|_{z=\eta_2^+} = (0, 0, 0)$. Hence $[\boldsymbol{u} \cdot \boldsymbol{n}]_{z=\eta_2} = 0$.

The uniform flow layer $\mathcal{U}(t)$

Existing between the transitional layer and the thermocline is a layer in which all particles experience a uniform horizontal motion. This purely zonal current has the following velocity field

$$(u, v, w) = (c - c_0, 0, 0)\,,$$

which by way of the Euler equations for geophysical ocean flows gives rise to the pressure distribution

$$P = \rho_+ \hat{f}(c - c_0)\left[z - \tilde{f}y\right] - \rho_+ g z + \rho_+ \hat{f}\frac{1}{2}(c - c_0)(d_1 + d_2) + P_0,$$

in the layer $\mathcal{U}(t)$. Evaluating the pressure in $\mathcal{T}(t)$ at $z = \eta_1 = -d_1 + \tilde{f}y$, we have $z + d_2 - \tilde{f}y = d_2 - d_1$, and so

$$P\Big|_{z=\eta_1^-} = \frac{1}{2}\rho_+ \hat{f}(c - c_0)(d_2 - d_1) - \rho_+ g\eta_1 + P_0.$$

Evaluating the pressure in $\mathcal{U}(t)$ at $z = \eta_1$, noting that $z - \tilde{f}y = -d_1$ there, gives

$$\begin{aligned} P\Big|_{z=\eta_1^+} &= \rho_+ \hat{f}(c - c_0)(-d_1) - \rho_+ g\eta_1 + \frac{1}{2}\rho_+ \hat{f}(c - c_0)(d_1 + d_2) + P_0 \\ &= \frac{1}{2}\rho_+ \hat{f}(c - c_0)(d_2 - d_1) - \rho_+ g\eta_1 + P_0. \end{aligned}$$

Hence $[P]_{z=\eta_1} = 0$. Furthermore, at $z = \eta_1$, the velocity in $\mathcal{T}(t)$ evaluates to $(c - c_0, 0, 0)$ since $z + d_2 - \tilde{f}y = d_2 - d_1$ there, giving $u = \frac{c - c_0}{d_2 - d_1}(d_2 - d_1) = c - c_0$. The velocity in $\mathcal{U}(t)$ is $(c - c_0, 0, 0)$ throughout, and so $[\boldsymbol{u} \cdot \boldsymbol{n}]_{z=\eta_1} = 0$.

The layer $\mathcal{M}(t)$, above the thermocline

The layer $\mathcal{M}(t)$ is bounded below by the thermocline, and above by $z = \eta_+(x, y, t)$. The internal wave motion in this layer is driven by the oscillation of the thermocline, and propagates above the thermocline. The solution that is constructed includes a uniform zonal current and is a Pollard-like internal wave in that it represents a periodic zonally travelling wave with a vertical amplitude that decays with height above the thermocline. Furthermore, the positions of fluid particles

(x, y, z) are described in the Lagrangian labelling variables (q, r, s), where

$$\begin{aligned} x &= q - be^{-ms}\sin[k(q-ct)] - c_0 t, \\ y &= r - de^{-ms}\cos[k(q-ct)], \\ z &= -d_0 + s - ae^{-ms}\cos[k(q-ct)], \end{aligned} \tag{2.56}$$

where $d_0 > d_1 > 0$, with the mean depth of the thermocline below the surface given by $d_0 - s_0 > 0$, and the Lagrangian variables are given by

$$(q, r, s) \in \mathbb{R} \times [-r_0, r_0] \times [s_0(r), s_+(r)],$$

with r_0 subject to the constraint to the constraint discussed below, and where $s = s_0(r) \geq s^* > 0$ represents the thermocline and $s = s_+(r) > s_0(r)$ represents the interface between the layers $\mathcal{M}(t)$ and $\mathcal{L}(t)$. We note that since $\widetilde{f} = \tan\phi$, the layer boundaries $\eta_i = -d_i + \widetilde{f}y$ are inclined with respect to the horizontal, with the inclination increasing with latitude. For the layer structure to remain physically consistent, the thermocline must remain above η_1 throughout the domain, which imposes a restriction on the meridional extent r_0 of the domain. This constraint becomes increasingly restrictive at higher latitudes, and the model is therefore most naturally applicable at low to mid latitudes away from the Equator, where the f-plane approximation is simultaneously valid and the layer inclination remains moderate. In particular, while the Antarctic Circumpolar Current (ACC) is used as a motivating example and its parameters are used in Figure 2.5, at the latitude of the ACC ($\phi \approx -60°$) this constraint is more restrictive than at lower latitudes, and the solution should be interpreted as a local description within a meridionally narrow band rather than a global model of the ACC.

As in the hydrostatic setting of Section 2.2, the explicit Lagrangian formulation (2.56) affords direct access to particle trajectory information in the fully nonlinear regime, a feature that is non-trivial to obtain even in the linear setting [54, 55]. The additional complexity of the nonhydrostatic model, incorporating transitional layers beneath the thermocline, does not obstruct this: the particle paths remain explicitly readable from the parametrisation (2.56). The solution is Pollard-like and thus describes particle paths as trochoidal orbits, tilted in the meridional direction at an angle $\arctan(-d/a)$ to the local vertical due to the Earth's rotation. We will later show that d is proportional to f, implying that the magnitude of the tilt increases with distance from the Equator. In what follows we uncover relations that determine the values of b, d, c in terms of $a > 0, m > 0, k > 0$. For convenience, let

$$\theta = k(q - ct).$$

The velocities and accelerations of a particle are given respectively through direct differentiation [5] by

$$\begin{aligned} u &= \frac{Dx}{Dt} = kcbe^{-ms}\cos\theta - c_0, \\ v &= \frac{Dy}{Dt} = -kcde^{-ms}\sin\theta, \\ w &= \frac{Dz}{Dt} = -kcae^{-ms}\sin\theta, \end{aligned}$$

and

$$\begin{aligned} \frac{Du}{Dt} &= k^2c^2be^{-ms}\sin\theta, \\ \frac{Dv}{Dt} &= k^2c^2de^{-ms}\cos\theta, \\ \frac{Dw}{Dt} &= k^2c^2ae^{-ms}\cos\theta. \end{aligned}$$

Substituting the above into the Euler equation (2.55) yields

$$\begin{aligned} P_x &= -\rho_0\left[kc\left(bkc - a\hat{f} + df\right)e^{-ms}\sin\theta\right], \\ P_y &= -\rho_0\left[kc\left(dkc + bf\right)e^{-ms}\cos\theta - fc_0\right], \\ P_z &= -\rho_0\left[kc\left(akc - \hat{f}b\right)e^{-ms}\cos\theta + \hat{f}c_0 + g\right]. \end{aligned}$$

The mapping from the particles position in our rotating Cartesian reference frame to the Lagrangian labelling variables has transposed Jacobian

$$\begin{pmatrix} \frac{\partial x}{\partial q} & \frac{\partial y}{\partial q} & \frac{\partial z}{\partial q} \\ \frac{\partial x}{\partial r} & \frac{\partial y}{\partial r} & \frac{\partial z}{\partial r} \\ \frac{\partial x}{\partial s} & \frac{\partial y}{\partial s} & \frac{\partial z}{\partial s} \end{pmatrix} = \begin{pmatrix} 1 - kbe^{-ms}\cos\theta & kde^{-ms}\sin\theta & kae^{-ms}\sin\theta \\ 0 & 1 & 0 \\ mbe^{-ms}\sin\theta & mde^{-ms}\cos\theta & 1 + mae^{-ms}\cos\theta \end{pmatrix},$$

with determinant

$$J = 1 + (am - bk)e^{-ms}\cos\theta - kmabe^{-2ms}.$$

For the flow to be incompressible $J_t/J = 0$, cf. [12] and so

$$am = bk, \tag{2.57}$$

and

$$ambke^{-2ms} \neq 1.$$

The above constraint that $J \neq 0$ ensures that (2.56) is a valid local diffeomorphic change of coordinates by means of the inverse function theorem. Since $s \geq s^* > 0$, and we have that $am = bk$ from (2.57), then

$$a^2 m^2 e^{-2ms^*} < 1,$$

and thus the maximum amplitude of a particle is given by

$$a_{max} = \frac{1}{m}. \tag{2.58}$$

The pressure gradient in the Lagrangian labelling variables is given by the change of variables

$$\begin{pmatrix} P_q \\ \\ P_r \\ \\ P_s \end{pmatrix} = \begin{pmatrix} \dfrac{\partial x}{\partial q} & \dfrac{\partial y}{\partial q} & \dfrac{\partial z}{\partial q} \\ \dfrac{\partial x}{\partial r} & \dfrac{\partial y}{\partial r} & \dfrac{\partial z}{\partial r} \\ \dfrac{\partial x}{\partial s} & \dfrac{\partial y}{\partial s} & \dfrac{\partial z}{\partial s} \end{pmatrix} \cdot \begin{pmatrix} P_x \\ \\ P_y \\ \\ P_z \end{pmatrix},$$

leading to the following system of equations

$$\begin{aligned} P_q &= -\rho_0 \Big[k^3 c^2 \left(a^2 + d^2 - b^2\right) e^{-2ms} \cos\theta \sin\theta \\ &\qquad + (bk^2c^2 - a\hat{f}kc + a\hat{f}kc_0 - dfkc_0 + dkfc + gak) e^{-ms} \sin\theta \Big], \\ P_r &= -\rho_0 \Big[kc \left(dkc + bf\right) e^{-ms} \cos\theta - fc_0 \Big], \\ P_s &= -\rho_0 \Big[\left(ak^2c^2 + \hat{f}amc_0 - fdmc_0 - \hat{f}bkc + gam\right) e^{-ms} \cos\theta \\ &\qquad + mkc(kcb^2 - \hat{f}ab + fbd) e^{-2ms} \\ &\qquad + mk^2c^2(a^2 + d^2 - b^2) e^{-2ms} \cos^2\theta + g + \hat{f}c_0 \Big]. \end{aligned} \tag{2.59}$$

Assuming that the pressure in $\mathcal{M}(t)$ has continuous second order mixed partial derivatives, the relation $P_{qr} = P_{rq}$ yields

$$dkc + bf = 0. \tag{2.60}$$

while $P_{qs} = P_{sq}$ gives

$$mkc^2 b + mcdf = k^2 c^2 a. \tag{2.61}$$

From the pressure gradient (2.59), the pressure is found as

$$\begin{aligned} P(q,r,s) = \widetilde{P}_0 - \rho_0 \Big[& -fc_0 r + \left(g + \hat{f}c_0\right) s - \frac{1}{2}\left(b^2k^2c^2 - \hat{f}abkc + fbdkc\right) e^{-2ms} \\ & - (bkc^2 - a\hat{f}c + a\hat{f}c_0 - dfc_0 + dfc + ga) e^{-ms}\cos\theta \\ & - \frac{1}{2}k^2c^2\left(a^2 + d^2 - b^2\right) e^{-2ms}\cos^2\theta \Big]. \end{aligned} \tag{2.62}$$

It is required that the pressure be continuous across the thermocline, that is the pressure in $\mathcal{M}(t)$ must equal the pressure in $\mathcal{U}(t)$ when evaluated on the thermocline. Thus for a given latitude r, and the pressure evaluated on the thermocline $s = s_0(r)$, we define that

$$\begin{aligned} P_0 - \widetilde{P_0} = & \frac{1}{2}\rho_0 bkc\left(bkc - a\hat{f} + df\right) e^{-ms_0} - \left(\rho_+\hat{f}c - (\rho_+ - \rho_0)\, g\right) s_0 + (\rho_+ - \rho_0)\,\hat{f}c_0 s_0 \\ & + \rho_+ fcr - (\rho_+ - \rho_0)\, fc_0 r - \frac{1}{2}(c - c_0)\,\rho_+\hat{f}\,(d_2 + d_1) + d_0\rho_+\left(\hat{f}\,(c - c_0) - g\right), \end{aligned}$$

where the thermocline at a given latitude is found by solving the above implicit equation for $s_0(r)$. Furthermore, the pressure distribution (2.62) must hold for all times t, leading to the relations

$$a^2 + d^2 = b^2,$$

$$bkc^2 = \frac{\rho_+ - \rho_0}{\rho_0}\left[-a\hat{f}c + a\hat{f}c_0 - dfc_0 + dfc + ga\right]. \tag{2.63}$$

Relations (2.57), (2.60) and (2.61), can be rearranged to yield the following

$$b = \frac{ma}{k},$$

$$d = -\frac{fma}{k^2c}, \tag{2.64}$$

$$m^2 = \frac{k^4c^2}{k^2c^2 - f^2}. \tag{2.65}$$

It is noteworthy that the third equation above implies that on the equator (where $f = 0$) $m = k$ and hence m can be thought of as a 'modified wavenumber'. The dispersion relation for nonhydrostatic internal water waves in the presence of a uniform zonal current induced by the oscillations of the thermocline is found through substitution of the above parameters into the continuity equation (2.63),

and takes the form:

$$\left[k^2c^3+\frac{\rho_+-\rho_0}{\rho_0}f^2\left(c-c_0\right)\right]^2=\left(\frac{\rho_+-\rho_0}{\rho_0}\right)^2\left(k^2c^2-f^2\right)\left(g-\hat{f}\left(c-c_0\right)\right)^2, \tag{2.66}$$

Note that in the absence of a mean horizontal current this result agrees with the dispersion relation found in [66].

2.3.3 Perturbative analysis of the dispersion relation

To analyse this dispersion relation further we first nondimensionalise it by introducing the nondimensionalised variables

$$X=c\sqrt{\frac{k}{\widetilde{g}}},\quad X_0=c_0\sqrt{\frac{k}{\widetilde{g}}},\quad \varepsilon=\frac{f}{\sqrt{\widetilde{g}k}},\quad F=\frac{\hat{f}}{f}. \tag{2.67}$$

A typical value [38] for $\widetilde{g}$ at the Equator is 6×10^{-3} ms^{-2}. This allows the dispersion relation (2.66) to be rewritten as

$$\left[X^3+\varepsilon^2\left(\frac{\rho_+-\rho_0}{\rho_0}\right)\left(X-X_0\right)\right]^2=\left(X^2-\varepsilon^2\right)\left[1-\varepsilon F\left(\frac{\rho_+-\rho_0}{\rho_0}\right)\left(X-X_0\right)\right]^2,$$

which can be expanded to yield the following polynomial of degree six with $P(X)=0$ and

$$\begin{aligned}
P(X)=&X^6+\varepsilon^2\left(\frac{\rho_+-\rho_0}{\rho_0}\right)\left[2-F^2\left(\frac{\rho_+-\rho_0}{\rho_0}\right)\right]X^4\\
&+2\varepsilon\left(\frac{\rho_+-\rho_0}{\rho_0}\right)\left[F-\varepsilon X_0+\varepsilon F^2\left(\frac{\rho_+-\rho_0}{\rho_0}\right)X_0\right]X^3\\
&+\left[\left(\frac{\rho_+-\rho_0}{\rho_0}\right)^2\varepsilon^4-1-2\varepsilon F\left(\frac{\rho_+-\rho_0}{\rho_0}\right)X_0\right.\\
&\quad\left.-\varepsilon^2F^2\left(\frac{\rho_+-\rho_0}{\rho_0}\right)^2X_0^2+\varepsilon^4F^2\left(\frac{\rho_+-\rho_0}{\rho_0}\right)^2\right]X^2\\
&-2\varepsilon^3\left(\frac{\rho_+-\rho_0}{\rho_0}\right)\left[\varepsilon\left(\frac{\rho_+-\rho_0}{\rho_0}\right)X_0+F+\varepsilon F^2\left(\frac{\rho_+-\rho_0}{\rho_0}\right)X_0\right]X\\
&+\varepsilon^2\left[\left(\frac{\rho_+-\rho_0}{\rho_0}\right)^2\varepsilon^2X_0^2+1+2\varepsilon F\left(\frac{\rho_+-\rho_0}{\rho_0}\right)X_0+\varepsilon^2F^2\left(\frac{\rho_+-\rho_0}{\rho_0}\right)^2X_0^2\right].
\end{aligned}$$

The roots to the dispersion relation at mid-latitudes cannot be found analytically, however Figure 2.5 suggests that roots may be found near to $X=\pm1$ and $X=$

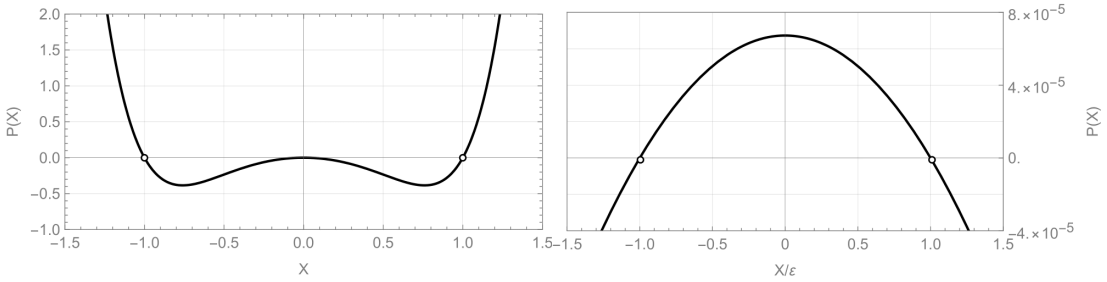

(a) (b)

Figure 2.5: Plots of the dispersion relation $P(X)$: panel (a) shows two $O(1)$ roots, and panel (b) shows two $O(\varepsilon)$ roots. Parameters $f \approx -1.3 \times 10^{-4}\,\mathrm{s}^{-1}$, $c_0 \approx -0.3\,\mathrm{m\,s}^{-1}$ and $k = 6.28 \times 10^{-2}\,\mathrm{m}^{-1}$ are chosen to match the Antarctic Circumpolar Current.

$\pm\varepsilon$. With this in mind we search for accurate approximations to the roots of $P(X)$ through a perturbation expansion in the small parameter ε. Let

$$X = x_0 + \varepsilon x_1 + \varepsilon^2 x_2 + \varepsilon^3 x_3 + ...$$

Substituting into $P(X)$ and collecting different powers of ε, it is found that to $O(\varepsilon^0)$

$$x_0^6 - x_0^2 = 0,$$

and thus

$$x_0 = \{0, \pm 1, \pm i\}.$$

The roots to $P(X)$ near to $X = \pm 1$ correspond to internal Gerstner-like waves slightly modified by the Earth's rotation. Since we are only interested in physical roots, for the following analysis we assume that $x_0 = 0$, which results in the existence of two possible small roots mediated by the presence of a nonhydrostatic zonal current, and are approximately given by

$$X = \pm\varepsilon \left(1 + \varepsilon^2 \left(\frac{\rho_+ - \rho_0}{\rho_0}\right)^2 \frac{X_0^2}{2}\right). \tag{2.68}$$

This gives an approximation of the wavespeed to $O(\varepsilon^2)$ of

$$c \approx \pm\frac{f}{k}, \tag{2.69}$$

and therefore the period of this wave motion is

$$T = \frac{\lambda}{c} \approx \pm\frac{2\pi}{f} = T_i,$$

where $\lambda = {}^{2\pi}/_{k}$ is the wavelength and T_i is the inertial period of the Earth, and so the wave motion described by (2.68) is that of an inertial wave. Calculating further an approximation of the wavespeed to $O(\varepsilon^3)$ we find that

$$c^2 = \frac{f^2}{k^2}\left(1 + \varepsilon^2\left(\frac{\rho_+ - \rho_0}{\rho_0}\right)^2 X_0^2 + O(\varepsilon^4)\right).$$

Substitution of the above wavespeed into (2.65) yields

$$m = \frac{k^2 c}{f\varepsilon\left(\frac{\rho_+ - \rho_0}{\rho_0}\right) X_0}.$$

Reversing the nondimensionalisation (2.67), and substituting (2.26) and (2.69) into the above yields a value for the modified wavenumber

$$m \approx \pm\frac{gk}{fc_0}, \tag{2.70}$$

quantifying the rate of decay of the amplitude of the internal wave with height above the thermocline. The velocity of a particle is calculated as

$$u^2 + v^2 + w^2 = c_0^2 + a^2m^2c^2e^{-2ms} - 2c_0amce^{-ms}\cos\theta,$$

with maximum particle speed at depth s,

$$v_{\max}(s) = c_0 + amce^{-ms},$$

which, upon substitution of (2.69) and (2.70), gives

$$v_{\max}(s) \approx c_0 + \frac{ag}{c_0}e^{-ms}.$$

We can estimate the maximum lateral and longitudinal amplitudes. The lateral amplitude can be expressed through the manipulation of (2.64), (2.69) and (2.70) to yield

$$d \approx \pm a\frac{g}{fc_0}.$$

Similarly, the longitudinal displacement is found to be

$$b \approx \pm a\frac{g}{fc_0}.$$

An upper bound for the vertical displacement of particle motion was established in (2.58) and can be used along with (2.70) to estimate the maximum lateral (and

longitudinal) displacement as follows,

$$d_{max} \approx \frac{g}{mfc_0} \approx \frac{1}{k} (\approx b_{max}).$$

Therefore, the lateral and longitudinal displacement of a particle undergoing this wave motion greatly exceeds its vertical displacement. In comparison with the hydrostatic model presented in [85], an artefact of this more physically realistic model is that the presence of transitional layers beneath the thermocline compels the amplitude of particle motion to decrease more rapidly with height above the thermocline. This can be seen by comparing the decay scales of the two models: in the hydrostatic model $m \approx \pm \widetilde{g}k/fc_0$, whereas in the nonhydrostatic model $m \approx \pm gk/fc_0$. Since $g \gg \widetilde{g}$ (recalling that $\widetilde{g} \sim O(10^{-3})$ ms^{-2} while $g = 9.81$ ms^{-2}), the nonhydrostatic decay scale m^{-1} is significantly smaller, confirming that the wave amplitude decays more rapidly with height above the thermocline in the nonhydrostatic setting. Furthermore, recalling relation (2.58), the maximum vertical amplitude attainable by a particle on the thermocline is diminished in the presence of nonhydrostatic layers beneath the thermocline.

Chapter 3

Temperature dependent precipitation in exact nonlinear mountain waves

In this chapter we examine exact nonlinear mountain waves propagating in a moist atmosphere, and in particular we deduce the temperature profile of saturated laminar flow from the Clausius–Clapeyron equation with temperature-dependent enthalpies of vaporisation. The chapter combines the results of two published works [75, 76], where precipitation in nonlinear mountain waves was first examined using a constant enthalpy of vaporisation. While a constant enthalpy is a reasonable first approximation, the energy released during a phase transition depends on the temperature at which it occurs, and this dependence is non-negligible in the context of atmospheric energy budgets [1, 45]. In [75], this temperature dependence is incorporated through a linear model for the enthalpy of vaporisation, derived from Kirchhoff's equation [1] and given by

$$\Delta H'_{\mathrm{v}}(\mathscr{T}') = h'_0 - h'_1(\mathscr{T}' - \mathscr{T}'_0),$$

where $h'_0 \approx 2.500\,82 \times 10^6\,\mathrm{J\,kg^{-1}}$ is the specific enthalpy of condensation at $\mathscr{T}'_0 = 273.15\,\mathrm{K}$ and $h'_1 \approx 2.358 \times 10^3\,\mathrm{J\,kg^{-1}\,K^{-1}}$ [31]. The work of [76] subsequently addresses the nonlinear temperature dependence of the enthalpy of vaporisation, using the formula derived by Henderson-Sellers [45],

$$\Delta H'_{\mathrm{vap}}(\mathscr{T}') = \eta' \left(\frac{\mathscr{T}'}{\mathscr{T}' - \alpha'} \right)^2,$$

where $\eta' := 1.918\,46 \times 10^6\,\mathrm{J\,kg^{-1}}$ and $\alpha' := 33.91\,\mathrm{K}$. This nonlinear model is accurate to within 0.02% between 273 K and 303 K [45], offering a notable improvement over both the constant and linear approximations. Additionally, [76] examines the phase change of deposition, that is the direct transition of water vapour to ice, and is itself characterised by an enthalpy with nonlinear tempera-

ture dependence.

The exact solution underlying both works was originally developed in [16], where vertically propagating nonlinear waves were constructed as exact solutions of the governing equations for gravity waves in a stratified dry atmosphere; dry here meaning no heat is released by condensation of water vapour, as distinct from an absence of atmospheric moisture [23]. The solution is expressed explicitly in terms of Lagrangian labelling variables and takes the form of a Gerstner-like wave [40] superimposed on constant background wind currents, which incorporate orographic lift through the adiabatic displacement of air parcels. In [50], this solution was extended to three dimensions through the incorporation of a transverse current, and the governing equations were generalised to include Coriolis effects via the f-plane approximation. It is shown therein that retaining the Earth's rotation and incorporating a mean vertical current are mutually exclusive within this framework: the compatibility condition on the pressure field requires either $W_0 = 0$ (yielding trapped lee waves in the equatorial f-plane) or $\Omega = 0$ (yielding vertically propagating mountain waves at arbitrary latitudes, consistent with the solution of [16]). The flows examined in the present chapter fall within the latter setting.

The rich kinematic structure of the Lagrangian description affords direct descriptions of thermodynamic variables within the flow; this connection between the dynamic and thermodynamic descriptions was first exploited in [74] to deduce the temperature profile in a saturated atmosphere, and it is this connection that the articles [75] and [76] on which this chapter is based, extend to the case of temperature-dependent enthalpies of vaporisation. A significant feature of this approach is that it operates entirely within fully nonlinear wave theory, in contrast to the classical analysis of mountain waves, which relies on the Boussinesq approximation and is consequently restricted to small-amplitude linear waves [33, 94, 100, 101]. The exact solution framework employed here belongs to a broader programme of Lagrangian exact solutions that has seen considerable development in recent years, encompassing surface [10, 13, 25, 47] and internal [65, 85, 86] ocean waves, two-layer stratified atmospheric flows [90], and the visible atmospheric dynamics of the celestial bodies [24].

The introduction of moisture into the air requires careful treatment in the governing equations. The mixture of dry air and water vapour means the equation of state must account for both components separately; however, following [29, 107], it is convenient to introduce the virtual temperature, which allows the moist-air equation of state to be written in a form analogous to that of dry air, while the first law of thermodynamics must incorporate a heat source term corresponding to the latent heat of condensation released as vapour condenses and precipitates.

Thermal diffusion, though small relative to pressure gradients and gravitational forces, plays an essential role in redistributing thermal energy within the atmosphere. In particular, diffusion transports heat from high- to low-temperature regions, with the thermodynamic effect of reducing entropy in precipitating zones. Combined with the second law of thermodynamics, this places a lower bound on the rate of entropy decrease within a precipitating region, and consequently an upper bound on the altitude at which precipitation can occur in the troposphere.

The waves under consideration in this thesis are short mountain waves with wavelengths of approximately 2 km, and although mountains exert a pronounced influence on atmospheric flows and the global distribution of precipitation, this is a scale not typically resolved by current global weather and climate prediction models [105]. On the windward side of a mountain range, moist air is forced upward by the terrain, cools adiabatically, and its moisture condenses and falls as precipitation. Having lost a substantial portion of its humidity, the air descends on the leeward side comparatively dry, creating rain shadows — regions of significantly reduced rainfall. A vivid illustration is the contrast between the windward and leeward flanks of the Olympic Mountains of Washington State, where annual precipitation exceeds 500 cm on the windward side while the leeward side typically receives below 50 cm. Beyond their influence on precipitation, mountain waves play a significant role in atmospheric momentum transport [8, 56], sub-grid parameterisations of atmospheric flow patterns [92], and the generation of clear-air turbulence in the upper troposphere [43] that can adversely affect aviation [7]. The turbulence induced by mountain waves is also exploited recreationally by unpowered glider aircraft. A visually striking manifestation of the interaction between mountain waves and atmospheric moisture is the formation of lenticular clouds downwind of mountain ranges, where moist air parcels are lifted into the condensation zone by the wave motion; while such formations appear nearly stationary, they are composed of rapidly moving air undergoing continuous condensation and evaporation. An example of such clouds can be seen in Fig. 3.1.

Extensive analytical and numerical studies on the effects of moisture and heat on mountain-wave flows have been carried out; see [101] for a comprehensive review of mountain meteorology. For instance [34, 35] examine the effects of moisture in linear mountain-wave theory. The effect of nonlinearities in the flow of moist air over mountains was investigated in [3], where moisture is incorporated in the nonlinear flow by modifying the buoyancy frequency of moist atmospheric regions; although the parcel equations themselves are linear, nonlinearity enters through the unknown position of the interface between moist and dry regions. The present work departs from this tradition by working with fully nonlinear exact

Figure 3.1: A lenticular cloud formation above Croagh Patrick, Ireland courtesy of Dr. Emily Gleeson, Meteorologist at Met Éireann. While such a cloud formation may appear static, it is in fact composed of moving air parcels in which moisture continually condenses as it cools during the wave's ascent and evaporates as it warms on descent.

solutions throughout. Of the three principal sources of atmospheric precipitation (convective clouds, frontal systems, and tropical cyclones), it is convective clouds, which draw energy from temperature and moisture-density stratification, that are most directly relevant to the laminar flow structures analysed here.

3.1 Governing equations

The typical physical scale of mountain waves mean that the effects of the Earth's rotation and sphericity can be reasonably neglected [106], and therefore the equations of motion are presented in a Cartesian coordinate system, with the x'-axis in the horizontal direction of wave propagation, the y'-axis parallel to the wavefront, and the z'-axis vertically upwards. In the context of the mountain waves considered here, the x'-axis is transverse to the mountain range, while the y'-axis is parallel to it. The z'-axis is parallel to the gravitational acceleration.

We assume that the flow is homogeneous parallel to the mountain range, and therefore the flow considered here is effectively two-dimensional with velocity components (u', w') along the x' and z'-axes respectively. Homogeneity along the y-axis now means $\partial_y \mathfrak{f} \equiv 0$ for any variable of state $\mathfrak{f}$ while $v = 0$. The Euler equation which governs this two-dimensional atmospheric flow is given in dimensional variables - denoted by primes here, which will be removed upon nondimensionalisation - by

$$\begin{aligned} u'_{t'} + u'u'_{x'} + w'u'_{z'} &= -\frac{1}{\rho'}P'_{x'}, \\ w'_{t'} + u'w'_{x'} + w'w'_{z'} &= -\frac{1}{\rho'}P'_{z'} - g', \end{aligned} \tag{3.1}$$

cf. [57], where ρ' is the air density, P' is the atmospheric pressure, $g' \approx 9.8\,\mathrm{m\,s^{-2}}$ is the Earth's gravitational acceleration and t' is time. Conservation of mass in the flow ensures that

$$\frac{\partial \rho'}{\partial t'} + \boldsymbol{\nabla} \cdot (\rho' \mathbf{u}') = 0,$$

throughout the flow. In fact, it will be determined that the nature of the exact solution (3.6) will ensure incompressibility,

$$\boldsymbol{\nabla} \cdot \mathbf{u}' = 0,$$

during an air parcels adiabatic ascent to saturation. Introducing the dimensionless variables, $t, x, z, u, w, \rho, P, T$ allows the equations of motion to be nondimensionalised using suitable physical length scales for short mountain waves by way of the following transformation,

$$\begin{gathered}(x', z') = L'(x, z), \quad t' = \frac{L'}{U'}t, \quad (u', w') = U'(u, w), \\ \rho' = \bar{\rho}'\rho, \quad P' = \bar{\rho}' U'^2 P, \quad T' = \frac{U'^2}{\mathfrak{R}_\mathrm{d}} T,\end{gathered} \tag{3.2}$$

where we assume that appropriate physical length and velocity scales for short mountain waves are approximated by $L' \approx 2000\,\mathrm{m}$ and $U' \approx 20\,\mathrm{m\,s^{-1}}$ respectively. The mean atmospheric density of the lower troposphere is approximately given by $\bar{\rho}' \approx 1\,\mathrm{kg\,m^{-3}}$, $\mathfrak{R}_d \approx 287\,\mathrm{J\,kg^{-1}\,K^{-1}}$ is the dry-air gas constant and T' is the absolute temperature measured in kelvin.

3.2 Thermodynamics of moist air

The cooling of an air mass forced to ascend over rising terrain can be considered a dry adiabatic process outside of regions of active precipitation, cf. [57]. However, if over the course of this ascent the air parcel cools sufficiently to reach saturation (meaning that water vapour is condensing at the same rate at which liquid water is evaporating), any further cooling leads to an excess of condensation and the formation of precipitation. In contrast to the flows examined in [16, 50] which considered dry adiabatic orographic lifting of air particles, the current work incorporates the effect of moisture precipitating in the atmosphere and the latent heat released during condensation cf. [74, 75]. A saturated air parcel can be considered an ideal gas composed of dry air and water vapour, and since the dynamic equilibrium between liquid water and water vapour means that any heat released during condensation is absorbed by evaporation, there is no net change in the temperature of the parcel. In general, the equation of state for a moist air

parcel is given by

$$P = \mathfrak{R}_d \rho_d T + \mathfrak{R}_v \rho_v T, \tag{3.3}$$

where $\mathfrak{R}_v \approx 461\,\mathrm{J\,kg^{-1}\,K^{-1}}$ is the water vapour gas constant, ρ_d and ρ_v are the densities for dry-air and water vapour respectively, and T is the absolute temperature of both gas-species which are in thermal equilibrium. For convenience, let us now introduce a modified temperature measure $\mathscr{T}$, known as the virtual temperature, and which is given by

$$\mathscr{T} = \left(1 - q + \frac{q}{\varepsilon}\right) T, \tag{3.4}$$

with

$$\varepsilon = \frac{\mathfrak{R}_\mathrm{d}}{\mathfrak{R}_\mathrm{v}} \approx 0.622, \qquad q = \frac{\rho_\mathrm{v}}{\rho_d + \rho_v},$$

cf. [41]. The virtual temperature $\mathscr{T}$ is the temperature at which a theoretical dry air parcel would attain equal pressure and density to a moist air parcel at absolute temperature T. The virtual temperature of a moist air parcel is always greater than the absolute temperature, although under typical atmospheric conditions the difference is typically less than 2%, cf. [29], and so in what follows it is a reasonable approximation to consider the virtual temperature $\mathscr{T}$, in lieu of the absolute temperature T. Physically, a parcel of warm air is less dense that a corresponding cool air parcel, while moist air is less dense than a corresponding parcel of dry air. By introducing the virtual temperature $\mathscr{T}$, we can approximate the effect of moisture in the atmosphere by considering instead a parcel of dry air at a slightly higher temperature, and allows us to rewrite the equation of state (3.3) in terms of the total density of the air parcel as follows

$$P = \rho \mathscr{T}.$$

Since the formation and subsequent fallout of precipitation is an irreversible process, by the second law of thermodynamics this necessitates a change in the entropy of the precipitating material elements, as well as its surrounding environment. For such non-isentropic flows, conservation of energy must account for the latent heat released by condensing water vapour as well as for the diffusion of heat into the surrounding dry air which acts as a heat sink, cf. [4, 41]. Therefore, the first law of thermodynamics can be rewritten in the form

$$\frac{\mathrm{D}\mathscr{T}}{\mathrm{D}t} - \frac{\mu}{\rho}\frac{\mathrm{D}P}{\mathrm{D}t} = \dot{Q}. \tag{3.5}$$

The constant parameter μ is given by $\mu = \frac{\mathfrak{R}_\mathrm{d}}{C_P} \approx 0.287$, where the heat capacity of dry-air at constant pressure and at $20\,^\circ\mathrm{C}$ is approximated as $C_P \approx$

$1000\,\mathrm{J\,kg^{-1}\,K^{-1}}$. The heat source $\dot{Q}$ is related to the thermal diffusivity of the surrounding dry-air, and the enthalpy of condensing water vapour in the following way

$$\dot{Q} = \kappa\nabla^2\mathscr{T} - \frac{\Delta H_{\mathrm{v}}}{1-q_{\mathrm{s}}}\frac{\mathrm{D}q_{\mathrm{s}}}{\mathrm{D}t}, \quad \kappa = \frac{K}{\bar{\rho}'U'L'C_p},$$

where the non-dimensionalised thermal diffusivity of dry-air is approximately $\kappa \approx 6.26 \times 10^{-10}$, q_s is the specific humidity of a moist air-parcel at saturation. Saturated specific humidity corresponds to the maximum ratio between the mass of water vapour to total moist air mass at a given temperature and pressure, and a relative humidity of 100%.

3.3 Explicit flow dynamics

3.3.1 The laminar flow layer

The exact solution to the nonlinear governing equations (3.1) is explicit in the Lagrangian labelling variables (a, b), and is given by specifying at time t, the positions

$$x(a,b,t) = U_0 t + a - \frac{1}{k}e^{kb}\sin(k(a-ct)), \tag{3.6a}$$

$$z(a,b,t) = d + W_0 t + b + \frac{1}{k}e^{kb}\cos(k(a-ct)), \tag{3.6b}$$

of an air particle propagating in the laminar flow region, in terms of the wavenumber $k > 0$, wavespeed $c > 0$, and the constant wind-currents $U_0, W_0 > 0$, see Figure 3.2.

Mathematically, the above solution permits appropriate real-valued labelling variables a, b and currents U_0, W_0, however, physical considerations will restrict these values. Furthermore, we impose the restriction that $b < 0$, ensuring that particle paths are curtate trochoids, and therefore do not self-intersect. For mountain waves propagating vertically in the leewards direction, we require that $U_0, W_0 > 0$. Similarly, we take $a \in [0, \infty)$, which paramterizes the leeside of the mountain, and $b \in (b_1, b_0)$ with $b_1 < b_0 < 0$ demarcating the laminar flow region. Beneath b_1, frictional effects near to the surface may induce turbulence and lead to low-level atmospheric rotors, see [32]. Meanwhile, as the density of the atmosphere decreases with altitude (and therefore with increasing b, pre-empting relation (3.8) which yields that $z_b > 0$), the amplitude of oscillation e^{kb}/k increases monotonically with increasing b. The exact solution (3.6) presented here is composed of a Gerstner-like solution in which particle paths are prescribed as circles with depth-dependent radii, superimposed on linear wind currents. Therefore, as

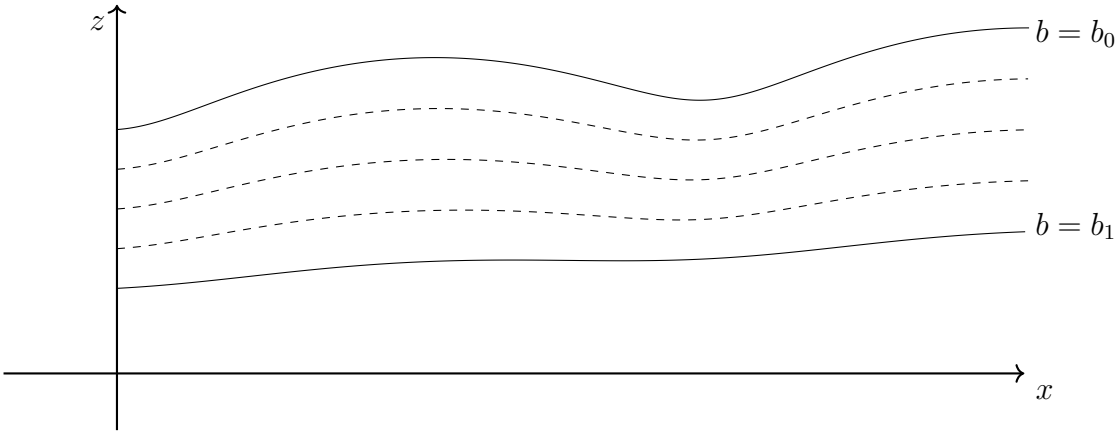

Figure 3.2: Particle paths in the (x, z)-plane for the flow (3.6), including the horizontal and vertical background winds U_0 and W_0. Air parcels follow trochoidal trajectories, whose shallow crests and sharp troughs reflect the highly nonlinear nature of the waves, in contrast to the sinusoidal waves of linear theory. The upper and lower boundaries of the laminar flow region correspond to the labelling variables $b = b_0$ and $b = b_1$ respectively, with $b_1 < b_0 < 0$.

depicted in Figure 3.2 the trajectories are trochoidal curves in the (x, z) plane which exhibit wide crests and narrow troughs, a feature of highly nonlinear waves.

For convenience, let us now introduce the notation $\xi = a - ct$. The horizontal and vertical velocities experienced by particles within the flow can be readily calculated by taking the derivative with respect to the time t of the particle positions 3.6,

$$u(a, b, t) = \frac{\partial x}{\partial t} = U_0 + ce^{kb}\cos(k\xi),$$
$$w(a, b, t) = \frac{\partial z}{\partial t} = W_0 + ce^{kb}\sin(k\xi).$$

The Jacobian matrix for the transformation to Lagrangian labelling variables 3.6 is given by

$$\mathbf{J} = \frac{\partial(x, z)}{\partial(a, b)} = \begin{bmatrix} 1 - e^{kb}\cos(k\xi) & -e^{kb}\sin(k\xi) \\ -e^{kb}\sin(k\xi) & 1 + e^{kb}\cos(k\xi) \end{bmatrix}, \tag{3.8}$$

with a non-zero Jacobian determinant for $b < 0$ given by

$$J = 1 - e^{2kb}. \tag{3.9}$$

For all $b \in (b_1, b_0)$ the inverse Jacobian matrix is

$$\mathbf{J}^{-1} = \begin{bmatrix} a_x & b_x \\ a_z & b_z \end{bmatrix} = \frac{1}{1 - e^{2kb}} \begin{bmatrix} 1 + e^{kb}\cos(k\xi) & e^{kb}\sin(k\xi) \\ e^{kb}\sin(k\xi) & 1 - e^{kb}\cos(k\xi) \end{bmatrix}. \tag{3.10}$$

From this it can be readily shown that the flows velocity is divergence free, that is

$$\nabla \cdot \mathbf{u} = (a_x \partial_a + b_x \partial_b)u + (a_z \partial_a + b_z \partial_z)w = 0,$$

and thus the solution (3.6) represents an incompressible atmospheric flow. Furthermore, the continuity equation (3.1) can now be expressed as

$$\frac{\mathrm{D}\rho}{\mathrm{D}t} = \frac{\partial \rho}{\partial t} + u\frac{\partial \rho}{\partial x} + w\frac{\partial \rho}{\partial z} = 0, \tag{3.11}$$

and thus the volume of a material fluid element is conserved throughout its trajectory.

3.3.2 The dispersion relation and pressure distribution

Given a density distribution of the form $\rho = \rho(\xi, b)$ it may be shown that

$$\frac{\partial \rho}{\partial \xi} = -\frac{1}{c}\frac{\mathrm{D}\rho}{\mathrm{D}t},$$

see [16] for a detailed proof. Moreover, given the incompressibility condition (3.11) it now follows that a density distribution $\rho(\xi, b)$ satisfies $\frac{\mathrm{D}}{\mathrm{D}t}\rho(\xi, b) \equiv 0$, meaning that the density distribution is in fact a univariate function $\rho(b)$. This implies that exact nonlinear mountain waves given by the diffeomorphism (3.6) are propagating in a stratified domain.

The pressure gradient defined by the governing equation (3.1) may be re–formulated in terms of the Lagrangian variables according to

$$\begin{bmatrix} P_a \\ P_b \end{bmatrix} = \mathbf{J}\begin{bmatrix} P_x \\ P_z \end{bmatrix} = \begin{bmatrix} (g - kc^2)\rho(b)e^{kb}\sin(k\xi) \\ kc^2 e^{2kb}\rho(b) - g\rho(b) + (kc^2 - g)\rho(b)e^{kb}\cos(k\xi) \end{bmatrix}, \tag{3.12}$$

so that the gradient $\boldsymbol{\nabla}_{(a,b)}P$ is well defined throughout the laminar flow layer, since $\mathbf{J}$ is non–singular everywhere in this domain (cf. equation (3.9)). The compatibility condition $\frac{\partial^2 P}{\partial a \partial b} = \frac{\partial^2 P}{\partial b \partial a}$ applied to the components P_a and P_b given in equation (3.12) now ensures

$$(g - kc^2)\frac{\partial \rho}{\partial b}e^{kb}\sin(k\xi) + k(g - kc^2)\rho e^{kb}\sin(k\xi) = -k(kc^2 - g)\rho e^{kb}\sin(k\xi), \tag{3.13}$$

for a general univariate density distribution $\rho(b)$. In atmospheric domains the density distribution is variable so that in general it is required that $\frac{\partial \rho}{\partial b} \neq 0$. This implies that the compatibility condition as given by equation (3.13) may be realised only when

$$kc^2 - g = 0 \implies c = \sqrt{\frac{g}{k}}, \tag{3.14}$$

which yields the dispersion relation for the atmospheric waves described by (3.6). The wave–speed c is chosen to be the positive root of this dispersion relation since the mountain waves under consideration here are propagating in the leeward direction only.

Given the gradient (3.12) and the dispersion relation (3.14), it now follows that $P_a = 0$ so that $P = P(b)$. Furthermore, using the equation of state $P = \rho\mathscr{T}$, the remaining component P_b may be integrated to yield

$$P(b) = P_* \exp\left(-g\int_{b_*}^{b} \frac{J(s)}{\mathscr{T}(s)}\,\mathrm{d}s\right), \qquad b \in [b_1, b_0]. \tag{3.15}$$

Moreover, the inverse Jacobian matrix (3.10) may be used to calculate the pressure gradient

$$\frac{\partial P}{\partial z} = \frac{\partial b}{\partial z}\frac{\partial P}{\partial b} < 0,$$

since it follows that $P_b < 0$ from (3.15) and the facts that $J > 0$ and $\mathscr{T} > 0$, since $\mathscr{T}$ is measured in Kelvin. Furthermore, since $b_z > 0$ as is clear from equation (3.10), it now follows that pressure decreases monotonically with altitude.

Dalton's law of partial pressures also now means that atmospheric pressure may be written according to $P(b) = e(b) + p(b)$, where $e(b)$ is the partial pressure of water vapor along any streamline b, while $p(b)$ is the partial pressure of dry–air along that same streamline. This now means the atmospheric pressure as given by equation (3.15) may also be written according to

$$e(b) + p(b) = e_* \exp\left(-g\int_{b_*}^{b} \frac{J(s)}{\mathscr{T}(s)}\,\mathrm{d}s\right) + p_* \exp\left(-g\int_{b_*}^{b} \frac{J(s)}{\mathscr{T}(s)}\,\mathrm{d}s\right), \tag{3.16}$$

where e_* and p_* are the partial pressures of vapor and dry-air along a given streamline b_*.

3.4 Saturated air flows

When the liquid and gaseous phases of water within an air-parcel are in equilibrium, the saturated vapour pressure and temperature are related by the Clausius-Clapeyron equation, given in physical variables by

$$\frac{1}{e'_s}\frac{\mathrm{d}e'_s}{\mathrm{d}T'} = \frac{\Delta H'_{\mathrm{v}}}{\mathfrak{R}_{\mathrm{v}} T'^2}.$$

Given the relationship between physical and non-dimensionalised variables in (3.2), the non-dimensionalised Clausius-Clapeyron equation is given by

$$\frac{1}{e_s}\frac{\mathrm{d}e_s}{\mathrm{d}\mathscr{T}} = \frac{\Delta H_\mathrm{v}}{\mathscr{T}^2}, \tag{3.17a}$$

$$\Delta H_\mathrm{v}\left(\mathscr{T}\right) = \frac{\mathfrak{R}_\mathrm{d}}{\mathfrak{R}_\mathrm{v}U'^2}\Delta H'_\mathrm{v}\left(U'^2\mathscr{T}/\mathfrak{R}_d\right), \tag{3.17b}$$

where T has been approximated by $\mathscr{T}$ again, in line with equation (3.5).

For many applications the enthalpy of vapourisation of water is taken as constant, commonly with a value of $\Delta H_{vap} = 2.5 \times 10^6\,\mathrm{J\,kg^{-1}}$, cf. [87]. In general though, enthalpy H is defined as the sum of a system's internal energy U and the product of it's pressure P and volume V,

$$H = U + PV.$$

By considering a saturated air parcel as an ideal gas with a fixed number of air particles n, the internal energy is thus purely kinetic and depends only on the temperature. Furthermore, by the ideal gas law $PV = nRT$, and the fact that both n and the universal gas constant R are constants, in what follows we will assume that $H = H(T) \approx H(\mathscr{T})$.

3.5 Linear temperature-dependent enthalpy

The simplest temperature-dependent model for enthalpy of vapourisation is the linear model, given by

$$\Delta H'_\mathrm{v}(\mathscr{T}') = h'_0 - h'_1(\mathscr{T}' - \mathscr{T}'_0) \tag{3.18}$$

where the parameter $h'_0 \approx 2.500\,82 \times 10^6\,\mathrm{J\,kg^{-1}}$ is the specific enthalpy of condensation at $\mathscr{T}'_0 = 273.15\,\mathrm{K}$ and $h'_1 \approx 2.358 \times 10^3\,\mathrm{J\,kg^{-1}\,K^{-1}}$ (see [31]). There are several other, closely related, approximations for these parameters (see [41, 45] for instance). The non-dimensionalised Clausius-Clapeyron equation (3.17a) means the non-dimensionalised analogue of this enthalpy function may be written in the form

$$\Delta H_\mathrm{v}(\mathscr{T}) = \eta_0 - \eta_1\mathscr{T}, \tag{3.19a}$$

$$\eta_0 = \frac{\mathfrak{R}_\mathrm{d}}{\mathfrak{R}_\mathrm{v}U'^2}(h'_0 + h'_1\mathscr{T}'_0) \approx 4893, \qquad \eta_1 = \frac{h'_1}{\mathfrak{R}_\mathrm{v}} \approx 5.112, \tag{3.19b}$$

where the parameters η_0 and η_1 follow from equation (3.17b).

3.5.1 Saturation temperature and pressure distributions

When the temperature dependence of enthalpy of vapourisation is accounted for as in equation (3.19a), the Clausius-Clapeyron equation (3.17a) may be integrated to give the saturation pressure as

$$e_{\mathrm{s}}(\mathscr{T}) = e_{\mathrm{s},*}\left(\frac{\mathscr{T}_*}{\mathscr{T}}\right)^{\eta_1}\exp\!\left\{\eta_0\left(\frac{1}{\mathscr{T}_*}-\frac{1}{\mathscr{T}}\right)\right\}, \tag{3.20}$$

a function of temperature only. The boundary conditions $\mathscr{T} = \mathscr{T}_*$ and $e = e_{\mathrm{s},*}$ are the temperature and vapour pressure along a given saturated streamline $b = b_*$. At saturation the liquid-to-gas and gas-to-liquid phase changes are in equilibrium so that there is no net loss or gain of vapour at saturation, meaning the vapour phase is effectively an ideal gas (see [29] for a detailed discussion), so that the equation of state $e_{\mathrm{s}} = \varepsilon\rho_{\mathrm{v}}T$ holds approximately. Moreover, Dalton's law of partial pressures ensures $P(b) = p(b) + e(b)$, while the virtual temperature (3.4) is defined so as to ensure the equation of state $p+e = \rho\mathscr{T}$ in general. In particular, along a saturated streamline b, equation (3.15) is equivalently given by

$$\frac{\mathrm{d}}{\mathrm{d}b}\left(p+e_{\mathrm{s}}\right) = -g\frac{J}{\mathscr{T}}\left(p+e_{\mathrm{s}}\right) \implies p(b)+e_{\mathrm{s}}(b) = (p_*+e_{\mathrm{s},*})\exp\!\left\{-g\int_{b_*}^{b}\frac{J(s)}{\mathscr{T}(s)}\,\mathrm{d}s\right\},$$

having used the boundary conditions $p(b_*) + e_{\mathrm{s}}(b_*) = p_* + e_{\mathrm{s},*} = P_*$ on the saturated streamline b_*. As such, the saturation pressures along the streamlines b_* and b are also related by

$$e_{\mathrm{s}}(b) = e_{\mathrm{s},*}\exp\!\left\{-g\int_{b_*}^{b}\frac{J(s)}{\mathscr{T}(s)}\,\mathrm{d}s\right\}. \tag{3.21}$$

Equations (3.20)–(3.21) now provide two distinct expressions for saturation pressure $e_{\mathrm{s}}(b)$, which we equate to find

$$\left(\frac{\mathscr{T}_*}{\mathscr{T}(b)}\right)^{\eta_1}\exp\!\left\{\eta_0\left(\frac{1}{\mathscr{T}_*}-\frac{1}{\mathscr{T}(b)}\right)\right\} = \exp\!\left\{-g\int_{b_*}^{b}\frac{J(s)}{\mathscr{T}(s)}\,\mathrm{d}s\right\}, \tag{3.22}$$

having set $\mathscr{T} = \mathscr{T}(b)$ in equation (3.20). It is also noted that $\mathscr{T}$ and T may be related according to

$$\mathscr{T} = \frac{T}{1-({}^{e}\!/_{P})\,(1-\varepsilon)},$$

so within a saturated domain $b \in [b_*, b^\dagger]$ at equilibrium , we find

$$\frac{e_{\mathrm{s}}(b)}{P(b)} = \frac{e_{\mathrm{s},*}}{P_*} \implies \mathscr{T}(b) = \beta_* T(b)$$
$$\beta_* = \frac{1}{1 - (e_{\mathrm{s},*}/P_*)(1-\varepsilon)}$$

along any saturated streamline. However it should be noted that this relationship only applies for adiabatic parcel transfer, since $\frac{\mathrm{D}}{\mathrm{D}t}\left(\frac{e_{\mathrm{s}}}{P}\right) \neq 0$ during an irreversible process such as precipitation. Applying the natural logarithm to equation (3.22) and differentiating with respect to b, it now follows that

$$\frac{\eta_0 - \eta_1 \mathscr{T}}{\mathscr{T}} \mathscr{T}_b = -gJ. \tag{3.23}$$

Integrating (3.23) we find

$$-\frac{\eta_1 \mathscr{T}}{\eta_0} \exp\left\{-\frac{\eta_1 \mathscr{T}}{\eta_0}\right\} = -\frac{\eta_1 \mathscr{T}_*}{\eta_0} \exp\left\{-\frac{1}{\eta_0}\left(\eta_1 \mathscr{T}_* + g\int_{b_*}^{b} J(s)\,\mathrm{d}s\right)\right\} =: \varphi(b), \tag{3.24}$$

having imposed the boundary condition $\mathscr{T}(b_*) = \mathscr{T}_*$. This can be solved explicitly in terms of the Lambert W function (cf. [28]) to give

$$\mathscr{T}(b) = -\frac{\eta_0}{\eta_1} W\left(\varphi(b)\right), \tag{3.25}$$

with $W(\phi)$ defined according to $W(\phi \exp\{\phi\}) = \phi$. It follows from equations (3.19a) and (3.25) that the enthalpy function may be explicitly written as

$$\Delta H_{\mathrm{v}}(b) = \eta_0 \left(1 + W\left(\varphi(b)\right)\right).$$

It is clear from (3.19b) that ${}^{\eta_1 \mathscr{T}_*}/_{\eta_0} > 0$ while equation (3.25) ensures $\varphi(b) \in (-e^{-1}, 0]$ so that $W\left(\varphi(b)\right) \in \mathbb{R}$ on the principal value branches W_0 and W_{-1}, while physically realistic temperatures are realised when $\mathscr{T}(b)$ is calculated using the W_0 branch only. The rich kinematical information provided by the Lagrangian description of the flow dynamics (3.6) gives rise to expression (3.15), specifying the temperature dependence of the vapour pressure in the flow throughout the entire domain, while the Clausius-Clapeyron equation leads to another, distinct expression, (3.20), for the temperature dependence of the vapour pressure at saturation. Compatibility between these two distinct expressions for the vapour pressure at saturation leads to an explicit description for the temperature throughout the saturated domain in terms of the Lambert W function, (3.25). If a streamline in the flow at a given temperature $\mathscr{T}(b_*) = \mathscr{T}_*$ is saturated, then it has been shown in this section that the dynamics of the flow are sufficient to determine

the temperature distribution throughout the entire saturated domain.

3.5.2 Adiabatic cooling to saturation

During orographic lift moist air is elevated adiabatically to higher altitude where its temperature decreases, while its relative humidity increases until it reaches 100% and further cooling eventually leads to condensation and cloud formation. Below this altitude at which saturation occurs, the moist air in the atmosphere is unsaturated and the relative humidity satisfies $e/e_s = \mathfrak{h} < 1$. At saturation, the relative humidity is $\mathfrak{h} = 1$, while adiabatic cooling of the water-vapour content means the first law of thermodynamics becomes

$$\frac{\mathrm{D}\mathscr{T}}{\mathrm{D}t} - \frac{\mu}{\rho_{\mathrm{v}}}\frac{\mathrm{D}e}{\mathrm{D}t} = 0,$$

(see [29] for instance), while the equation of state for vapour $e = \varepsilon\rho_{\mathrm{v}}T$ now ensures the first-law of thermodynamics may be written as

$$\frac{\mathrm{D}}{\mathrm{D}t}\ln(e) = \frac{1}{\mu\varepsilon}\frac{\mathrm{D}}{\mathrm{D}t}\ln(\mathscr{T}). \tag{3.26}$$

The logarithmic change in saturation vapour pressure e_s, is determined using the Clausius-Clapeyron equation and is given by

$$\frac{\mathrm{D}}{\mathrm{D}t}\ln(e_s) = \frac{\Delta H}{\mathscr{T}}\frac{\mathrm{D}}{\mathrm{D}t}\ln(\mathscr{T}). \tag{3.27}$$

We can use the above relations to determine the logarithmic change in relative humidity $\mathfrak{h}$ as

$$\frac{\mathrm{D}}{\mathrm{D}t}\ln(\mathfrak{h}) = \frac{\mathrm{D}}{\mathrm{D}t}\left(\ln(e) - \ln(e_{\mathrm{s}})\right) = \left(\frac{1}{\mu\varepsilon} - \frac{\Delta H\left(\mathscr{T}\right)}{\mathscr{T}}\right)\frac{\mathrm{D}}{\mathrm{D}t}\left(\ln(\mathscr{T})\right), \tag{3.28}$$

cf. [29]. Integrating from the initial conditions (temperature $\mathscr{T}$ and relative humidity $\mathfrak{h}$), to the conditions at which the air has become saturated with water vapour (temperature $\mathscr{T}_*$ and a relative humidity equal to 1),

$$\int_{\mathfrak{h}}^{1}\frac{1}{h}\,\mathrm{d}h = \int_{\mathscr{T}}^{\mathscr{T}_*}\left(\frac{1}{\mu\varepsilon\theta} - \frac{\Delta H}{\theta^2}\right)\mathrm{d}\theta\,. \tag{3.29}$$

The saturation temperature T_* may be defined implicitly in terms of the non-saturated relative humidity $\mathfrak{h}$ according to

$$\ln(\mathfrak{h}) = \eta_2\ln\left(\frac{\mathscr{T}}{\mathscr{T}_*}\right) + \eta_0\left(\frac{1}{\mathscr{T}} - \frac{1}{\mathscr{T}_*}\right); \qquad \eta_2 := \frac{1}{\mu\epsilon} + \eta_1$$

which may now be solved in terms of the Lambert W function according to

$$\mathscr{T}_* = -\frac{\eta_0}{\eta_2 W\left(-\frac{\eta_0}{\eta_2 \mathscr{T}} \exp\left\{-\frac{\eta_0}{\eta_2 \mathscr{T}}\right\} \mathfrak{h}^{\frac{1}{\eta_2}}\right)} \tag{3.30}$$

allowing us to specify $\mathscr{T}_*$ and b_* for the saturation temperature distribution in equation (3.25). It should be noted that for the values of temperature and relative humidity that are physically relevant to the meteorological processes examined here, the argument of the Lambert W function in (3.30) lies between $(-e^{-1}, 0)$, and so there exists two possible real solutions. For $x \in (-e^{-1}, 0)$ the principal branch $W_0(x) \in (-1, 0)$, and so for physically reasonable saturation temperatures only the lower branch $W_{-1}(x)$ is considered. This saturation temperature profile is in good agreement with the saturation Bolton temperature profile [6], which follows from (3.27) using a constant enthalpy ΔH_{v} with associated saturation temperature T_{s} given by the approximation

$$T_s \approx \frac{1}{\frac{1}{T-55} - \frac{\ln(\mathfrak{h})}{2840}} + 55, \tag{3.31}$$

see [29] for further discussion. A comparison of the two saturation temperature profiles is illustrated in Fig. 3.3 By introducing the concept of relative humid-

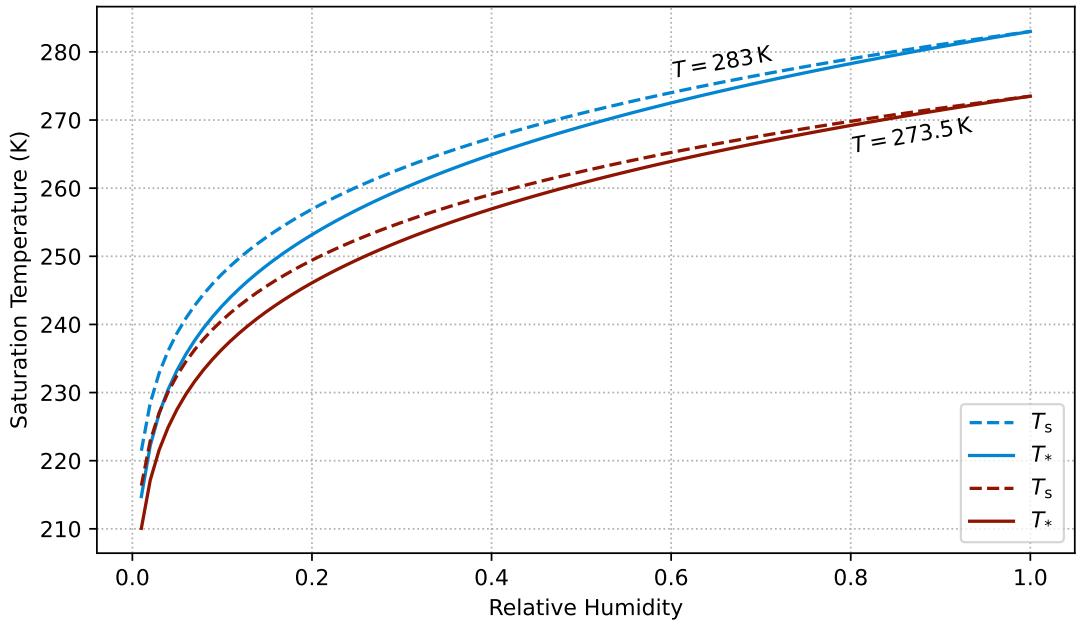

Figure 3.3: The saturation temperature T_* from (3.30) (solid curves) and Bolton's approximation T_{s} from (3.31) (dashed curves), plotted against relative humidity $\mathfrak{h} \in [0.01, 1]$ at temperatures $T = 273.5\,\mathrm{K}$ (red) and $T = 283\,\mathrm{K}$ (blue).

ity $\mathfrak{h}$, as the ratio of vapour pressure e, to vapour pressure at saturation e_s, and through application of the 1st law of thermodynamics and the Clausius-Clapeyron

equation, we have specified the relationship between temperature and relative humidity variations along a fluid parcel trajectory (3.28). The resulting differential equation can be solved subject to the boundary condition that an initially unsaturated fluid parcel at temperature $\mathscr{T}$ with relative humidity $\mathfrak{h} = \mathfrak{h}(\mathscr{T}) < 1$, will become saturated at a temperature $\mathscr{T}_*$ such that $\mathfrak{h} = \mathfrak{h}(\mathscr{T}_*) = 1$. This leads to a novel approximation (3.30) for the saturation temperature $\mathscr{T}_* = \mathscr{T}_*(\mathscr{T}, \mathfrak{h})$ in terms of the Lambert W function, derived from a linear temperature-dependent enthalpy of vapourisation (3.18).

3.5.3 Precipitation as a heat change within the flow

The ansatz (3.6a)–(3.6b) may also be understood to define the variables a and b implicitly in terms of the physical coordinates x and z. This in turn means we can now write the components of the temperature gradient according to

$$\begin{aligned}\mathscr{T}_x &= a_x \mathscr{T}_a + b_x \mathscr{T}_b = b_x \mathscr{T}_b,\\ \mathscr{T}_z &= a_z \mathscr{T}_a + b_z \mathscr{T}_b = b_z \mathscr{T}_b,\end{aligned}$$

where the last term in each expression follows from the fact that T is a function of b only and so $T_a \equiv 0$. Extending this process, it is also found that the Laplacian of the temperature is given by

$$\mathscr{T}_{xx} + \mathscr{T}_{zz} = \left[(b_x)_a \, a_x + (b_z)_a \, a_z + (b_x)_b \, b_x + (b_z)_b \, b_z \right] \mathscr{T}_b + \left[b_x^2 + b_z^2 \right] \mathscr{T}_{bb}, \quad (3.32)$$

where the x and z partial derivatives of a and b may be found explicitly in term of a and b from the inverse Jacobian matrix (3.10). Given the Jacobian matrix (3.8) and its inverse (3.10) the heating due to diffusion $\dot{Q}_{\mathrm{D}} = \kappa \nabla^2 \mathscr{T}$ follows from equation (3.32) and is given by

$$\dot{Q}_{\mathrm{D}} = \frac{2\kappa}{J} \left(1 - e^{kb} \cos(k\xi) \right) \frac{\mathrm{d}}{\mathrm{d}b} \left(\frac{\mathscr{T}}{J} \right) - \frac{\mathscr{T}_{bb}}{J},$$

while the specific form of the saturated temperature distribution is given by (3.25). As such the total heat change in the flow due to diffusion is

$$\begin{aligned}\Delta Q_{\mathrm{D}} &= \int_{b_*}^{b^\dagger} \int_0^1 \int_{t_1}^{t_2} \dot{Q}_{\mathrm{D}} J \, \mathrm{d}t \, \mathrm{d}a \, \mathrm{d}b\\ &= \kappa \int_{b_*}^{b^\dagger} \int_0^1 \int_{t_1}^{t_2} \left(\mathscr{T}_{bb} - 2 \left(1 - e^{kb} \cos(k\xi) \right) \frac{\mathrm{d}}{\mathrm{d}b} \left(\frac{\mathscr{T}}{J} \right) \right) \mathrm{d}t \, \mathrm{d}a \, \mathrm{d}b\\ &= -\kappa (t_2 - t_1) \left[\frac{gJ\mathscr{T}}{\eta_0 + \eta_1 \mathscr{T}} + 2 \frac{\mathscr{T}}{J} \right]_{b_*}^{b^\dagger} < 0\end{aligned}$$

having used equation (3.23) to re-write $\mathscr{T}_b$ in terms of $\mathscr{T}$, J and $\Delta H_{\mathrm{v}}(\mathscr{T})$. Heating due to condensation within the flow is given by

$$\dot{Q}_{\mathrm{C}} = -\frac{\Delta H}{1-q_{\mathrm{s}}}\frac{\mathrm{D}q_{\mathrm{s}}}{\mathrm{D}t} = (\eta_0 - \eta_1\mathscr{T})\frac{\mathrm{D}}{\mathrm{D}t}\ln(1-q_{\mathrm{s}}).$$

To integrate this heat source over the fluid domain, we note equation (3.23) means that $\mathscr{T}$ may be re-written according to

$$\mathscr{T} = -\frac{\Delta H}{gJ}\mathscr{T}_b,$$

so that

$$\dot{Q}_{\mathrm{C}} = \left(\eta_0 - \frac{\eta_1}{gJ}\left(\eta_0 - \eta_1\mathscr{T}\right)\mathscr{T}_b\right)\frac{\mathrm{D}}{\mathrm{D}t}\ln(1-q_{\mathrm{s}}).$$

As such the contribution to the heat change over a time interval $t \in [t_1, t_2]$ and the labelling domain $(a, b) \in [0,1] \times \left[b_*, b^\dagger\right]$, with boundary data

$$q_s(t_1) = q_{\mathrm{s},*} \qquad q_s(t_2) = \lambda q_{\mathrm{s},*} \qquad \lambda \in [0,1],$$

is given by

$$\int_{b_*}^{b^\dagger}\int_0^1\int_{t_1}^{t_2}\dot{Q}_{\mathrm{C}}J\,\mathrm{d}t\,\mathrm{d}a\,\mathrm{d}b = \ln\left(\frac{1-\lambda q_{\mathrm{s},*}}{1-q_{\mathrm{s},*}}\right)\int_{b_*}^{b^\dagger}\left(\eta_0 - \frac{\eta_1}{gJ}\left(\eta_0-\eta_1\mathscr{T}\right)\mathscr{T}_b\right)J\,\mathrm{d}b\,.$$

This integral may be evaluated explicitly to give the heat change due to condensation throughout the saturated fluid domain as

$$\Delta Q_{\mathrm{C}} = \ln\left(\frac{1-\lambda q_{\mathrm{s},*}}{1-q_{\mathrm{s},*}}\right)\left[\eta_0\left(b - \frac{e^{2kb}}{2k}\right) - \frac{\eta_1}{g}\left(\eta_0\mathscr{T} - \frac{\eta_1}{2}\mathscr{T}^2\right)\right]_{b_*}^{b^\dagger}.$$

The total heat change within the flow is $\Delta Q = \Delta Q_{\mathrm{C}} + \Delta Q_{\mathrm{D}}$, that is to say

$$\begin{aligned}\Delta Q = -\kappa(t_2-t_1)&\left[\frac{gJ\mathscr{T}}{\eta_0+\eta_1\mathscr{T}} - 2\frac{\mathscr{T}}{J}\right]_{b_*}^{b^\dagger}\\ &+\ln\left(\frac{1-\lambda q_{\mathrm{s},*}}{1-q_{\mathrm{s},*}}\right)\left[\eta_0\left(b-\frac{e^{2kb}}{2k}\right) - \frac{\eta_1}{g}\left(\eta_0\mathscr{T} - \frac{\eta_1}{2}\mathscr{T}^2\right)\right]_{b_*}^{b^\dagger}. \quad (3.33)\end{aligned}$$

The heat flux over an area covering one wavelength of the saturated domain, $A = ([0,1]\times(b_*, b^\dagger))$, over a time interval $[t_1, t_2]$ is given by the triple integral

$$\Delta Q = \iint_A\int_{t_1}^{t_2}\left(\dot{Q}_D + \dot{Q}_C\right)J dt dA.$$

Assuming that the mapping $(a, b) \mapsto (x(a, b), z(a, b))$ represents a diffeomorphism, then equation (3.32) represents the transformed Laplacian in terms of the variables (a, b) of a general univariate function $\mathscr{T}(b)$. Therefore, $\dot{Q}_D$ can be calculated explicitly using the temperature distribution derived in section §3.5.1. Meanwhile, to obtain an explicit expression for the heat change due to condensation over the saturated spatial domain and time interval $t \in [t_1, t_2]$, we impose that a precipitating fluid parcel can not have gained any additional moisture along its trajectory. Mathematically, this results in conditions at the temporal bounds $q_s(t_1) = q_{s,*}$ and $q_s(t_2) = \lambda q_{s,*}$, where $\lambda \in [0, 1]$.

3.5.4 Real world example - *Feldberg, Germany*

The change in heat, (3.33), within the saturated fluid domain is due to the fallout of precipitation from the flow, and so we can estimate the mass of precipitation which falls over a given area during a given time interval. To illustrate this, we use (3.33) to estimate the mass of rainfall over a region using meteorological field data gathered from measurements taken near to the summit of Feldberg, a mountain in the Black Forest of Germany between 1991 and 2020 (see NOAA for the data used in this example), and compare with average rainfall estimates for the region.

These records indicate that a mass $\overline{M}_{prec} = 6.216 \times 10^8\,\mathrm{kg}$ of precipitation falls over a region of area $L \times L = 4\,\mathrm{km}^2$ on average for the month of July. Furthermore, the data shows that on average the summit of Feldberg has no snowfall in July, and so for this example we will only consider the average data values from July for the thermodynamic variables. Therefore, we can assume that all of the heat change in the flow is due to condensation.

The station is located at a height $z'_M = 1.4896\,\mathrm{km}$, which when nondimensionalised yields $z_M = 0.7448$. Assuming that the measurements are taken at $t = 0$ from the mountain peak, that is at $x = 0$, then the b-parameter for the measurements is given by $b_M \approx -5.2552$. The mean daily temperature is $T'_M = 285.35\,\mathrm{K}$, and so the virtual temperature is $\mathscr{T}'_M = 286.8\,\mathrm{K}$ by (3.4). The mean vapour pressure is $e'_M = 11.4\,\mathrm{mbar}$, while the mean station-level pressure is $P'_M = 853\,\mathrm{mbar}$. The mean relative humidity is recorded as $\mathfrak{h} = 0.81$, and the specific humidity is given by 8.533×10^{-3}. The nondimensional analogues of the above thermodynamic variables are given as

$$T_M = 204.81, \quad \mathscr{T}_M = 205.85, \quad e_M = 2.85, \quad P_M = 213.25.$$

As described in section §3.5.2, air-parcels are assumed to rise adiabatically from the mountain peak until they reach saturation, and so during this ascent their

motion is governed by (3.26). Thus the saturation temperature can be calculated using (3.30) as $\mathscr{T}_* = 202.6$, which in physical variables is $\mathscr{T}'_* = 282.27\,\mathrm{K}$. Since the amplitude of oscillations for the flow (3.6) near to the summit are of the order $\exp\{kb_m\}/k \approx 7.3 \times 10^{-16}$, we can assume that the air parcel does not experience any large vertical accelerations during its dry adiabatic ascent from the mountain peak to the point where it becomes saturated. The dry adiabatic lapse rate can be derived (see [29]) in this hydrostatic approximation as $\Gamma_d = g/C_p \approx 9.8\,^\circ\mathrm{C\,km^{-1}}$, meaning that the air parcel becomes saturated at a height

$$\frac{\mathscr{T}'_M - \mathscr{T}'_*}{\Gamma_d} = 0.462\,\mathrm{km}$$

above the Feldberg summit. The corresponding value for the b-parameter at saturation is given by $b_* = -5.024$. The saturated streamline corresponding to b_* is sufficient to describe the saturation temperature distribution above this streamline using (3.25), however the temperature distribution below this streamline has been approximated here through the use of the dry adiabatic lapse rate Γ_d. During an air parcel's adiabatic rise to saturation, it is assumed that the specific humidity remains constant, that is $q_{s,*} = q_M = 8.355 \times 10^{-3}$. However, the energy released during condensation causes a change in internal and mechanical energy of that component of the parcel which does not fallout as liquid water. Thus, the parcel which is no longer in equilibrium with its surroundings will rise until it cools sufficiently to reach saturation and precipitate again. Through this process, an air-parcel may repeatedly lose moisture and thus we make the approximation that the specific humidity decays by 61.5% over the time interval (t'_1, t'_2), that is $\lambda = 0.385$. The nondimensionalised time interval for the month of July is given by $(t_2 - t_1) = 26784$.

Equation (3.33) now allows the total heat change over the labelling domain $(a, b) \in [0, 1] \times [b_*, b^\dagger]$ for $t \in [t_1, t_2]$ in physical variables to be calculated as

$$\Delta Q' = \frac{U'^2 L'^2}{R_d} \Delta Q \approx 7.76 \times 10^8\,\mathrm{m}^2,$$

and since the flow (3.6) is assumed to be homogeneous parallel to the mountain range, the total heat change over the field site is given by

$$\bar{\rho} C_p L' \Delta Q' \approx 1.55 \times 10^{15}\,\mathrm{J}. \tag{3.34}$$

To estimate the corresponding mass of water vapour required to precipitate from the flow, an indicative value of the saturated temperature distribution (3.25) is

calculated as the average of $\mathscr{T}(b)$ over the domain $b \in (b_*, b^\dagger)$,

$$\overline{\mathscr{T}'} = \frac{1}{b^\dagger - b_*} \int_{b_*}^{b^\dagger} \mathscr{T}(s) ds \approx 196.41.$$

Thus, the mass of precipitation corresponding to the change in energy found in (3.34) is found using the temperature-dependent enthalpy (3.18) as

$$\frac{1}{\Delta H'_{\mathrm{v}}\left(\overline{\mathscr{T}'}\right)} 1.55 \times 10^{15} \approx 6.219 \times 10^{8}\,\mathrm{kg},$$

compared with $\overline{M}_{prec} = 6.216 \times 10^8\,\mathrm{kg}$ estimated from the field data. In comparison with [74], which found an approximate value of $\lambda = 0.1$, here consideration of a temperature-dependent enthalpy of vapourisation suggests that the specific humidity decreases less rapidly over the time interval $t \in (t_1, t_2)$ than when considering a constant enthalpy of vapourisation.

3.5.5 Entropy in a saturated atmosphere

At the molecular scale, the energy of an arrangement of vapour molecules is unaffected by the interchange or rotation of molecules within the vapour, since these molecules are essentially freely moving. Contrarily the dipole-dipole interaction of molecules in liquid water introduces numerous inter-molecular forces, so that interchanging or rotating molecules will significantly affect the energy of this aggregate, thereby reducing the number of microstates available within a given energy range. During condensation vapour with a large number of available microstates undergoes a phase transition to liquid with relatively few available microstates thereby decreasing the entropy during the gas-to-liquid phase transition. A detailed treatment of entropy calculations in liquid water based on molecular dynamics and incorporating various inter-molecular forces may be found in [108].

Hydrometeor fallout is an irreversible process since it requires an external energy source such as solar radiation to return moisture to the atmosphere, and as such the second-law of thermodynamics means the entropy of a precipitating air parcel should increase during this process. However, since the latent heat of condensation is $\Delta H_{\mathrm{c}} = -\Delta H_{\mathrm{v}} < 0$, entropy of water vapour decreases during condensation $\Delta S_{\mathrm{v}} < 0$, while the second law of thermodynamics tells us that the entropy of the system should increase in the course of any spontaneous change [2]. However condensation is an exothermic process [69], meaning energy is released by the water vapour upon condensing and this released energy is absorbed by the surrounding dry-air increasing it's entropy $\Delta S_{\mathrm{d}} > 0$. This process alone suggests a balance in the entropy change for the moist-air system, however in physical

scenarios such as water condensation in the atmosphere there are non-ideal effects which contribute to a further increase in the entropy of the surroundings. In this case, the increased kinetic energy of the dry-air particles means that more heat will be dissipated through friction and collisions, and thus the entropy of the surroundings will further increase. Therefore, although the water vapour undergoes a decrease in entropy, the entropy of the overall system increases

$$\Delta S := \Delta S_{\mathrm{d}} + \Delta S_{\mathrm{v}} > 0,$$

so the the second law of thermodynamics is still observed. Consequently the rate of change of entropy during condensation is required to be positive, namely

$$\frac{\mathrm{D}S}{\mathrm{D}t} = \frac{\dot{Q}}{\mathscr{T}} > 0,$$

and since $\mathscr{T} > 0$, the irreversible process of precipitation may occur only when $\dot{Q} > 0$. This means only regions of the domain $(a, b) \in [0, 1] \times [b_*, b^\dagger]$ where

$$\frac{\mathrm{D}S}{\mathrm{D}t} = \kappa \frac{\nabla^2 \mathscr{T}}{\mathscr{T}} + \frac{\Delta H}{\mathscr{T}} \frac{\mathrm{D}}{\mathrm{D}t} \ln(1 - q_{\mathrm{s}}) > 0 \tag{3.35}$$

may precipitate. Precipitation occurs within a saturated air parcel only when $\frac{\mathrm{D}q_{\mathrm{s}}}{\mathrm{D}t} < 0$, indicating a loss of moisture due to hydrometeor fallout, so that

$$\frac{\mathrm{D}}{\mathrm{D}t} \ln(1 - q_{\mathrm{s}}) = -\frac{1}{1 - q_{\mathrm{s}}} \frac{\mathrm{D}q_{\mathrm{s}}}{\mathrm{D}t} > 0,$$

since $q_{\mathrm{s}} \ll 1$ typically (see [41, §4.4]). The net entropy change of a saturated parcel due to diffusion and condensation is required to satisfy

$$\frac{\mathrm{D}S}{\mathrm{D}t} = \frac{\Delta H}{\mathscr{T}} \frac{\mathrm{D}}{\mathrm{D}t} \ln(1 - q_{\mathrm{s}}) + \frac{g\kappa\eta_0 e^{kb}}{{\Delta H_{\mathrm{v}}}^3} \left(\cos(k\xi) - \cosh(kb) - \frac{1}{2c^2\eta_0} \frac{{\Delta H_{\mathrm{v}}}^2}{\sinh(kb)} \right) \geq 0, \tag{3.36}$$

so that the entropy increase due to condensation equals or exceeds the entropy decrease due to diffusion.

3.5.6 Dry air flows

When these entropy changes are balanced, $\frac{\mathrm{D}S}{\mathrm{D}t} = 0$, and an parcel is in equilibrium because heat loss by diffusion matches heat gain by condensation. This means the minimum rate at which latent heat increases along a saturated streamline is

$$\frac{\Delta H}{\mathscr{T}} \frac{\mathrm{D}}{\mathrm{D}t} \ln(1 - q_{\mathrm{s}}) = -\frac{g\kappa\eta_0 e^{kb}}{{\Delta H_{\mathrm{v}}}^3} \left(\cos(k\xi) - \cosh(kb) - \frac{1}{2c^2\eta_0} \frac{{\Delta H_{\mathrm{v}}}^2}{\sinh(kb)} \right) \geq 0. \tag{3.37}$$

This does not exclude the possibility that $\frac{\mathrm{D}}{\mathrm{D}t}\ln(1-q_{\mathrm{s}})$ grows at a faster rate, it only imposes a lower bound on this rate so that the second law of thermodynamics is ensured along a saturated streamline. However, there is also a subregion defined implicitly by the condition

$$\cos(k\xi) - \cosh(kb) - \frac{1}{2c^2\eta_0}\frac{{\Delta H_{\mathrm{v}}}^2}{\sinh(kb)} \geq 0,$$

in which case $\frac{\mathrm{D}}{\mathrm{D}t}\ln(1-q_{\mathrm{s}}) \leq 0$, which is not possible during precipitation. Since $H_{\mathrm{v}}(\mathscr{T}(b))$ is positive on the interval $b \in [b_*, b^\dagger]$, precipitation is only possible for

$$\mathfrak{S}(\xi, b) = \mathfrak{S}_1(\xi, b) - \mathfrak{S}_2(\xi, b) < 0, \tag{3.38a}$$

$$\mathfrak{S}_1(\xi, b) := \frac{g\kappa\eta_0 e^{kb}}{{\Delta H_{\mathrm{v}}}^3}\cos(k\xi), \tag{3.38b}$$

$$\mathfrak{S}_2(\xi, b) := \frac{g\kappa\eta_0 e^{kb}}{{\Delta H_{\mathrm{v}}}^3}\left(\cosh(kb) + \frac{1}{2c^2\eta_0}\frac{\Delta H_{\mathrm{v}}^2}{\sinh(kb)}\right) := \frac{g\kappa\eta_0 e^{kb}}{{\Delta H_{\mathrm{v}}}^3}\mathfrak{B}(\xi, b). \tag{3.38c}$$

Therefore, precipitation is possible whenever the inequality (3.38a) holds, or equivalently whenever

$$\cos(k\xi) < \cosh(kb) + \frac{1}{2c^2\eta_0}\frac{\Delta H_{\mathrm{v}}^2}{\sinh(kb)}. \tag{3.39}$$

As in the example in §3.5.4, in what follows we specify the boundary conditions for $\varphi(b)$ in (3.24) by assuming that the streamline initially at an altitude of 1.9496 km, ($b_* \approx -5.024$), is saturated with a nondimensionalised virtual temperature $\mathscr{T}_* \approx 202.6$. The surfaces $\mathfrak{S}_1$ and $\mathfrak{S}_2$ are illustrated in Fig. 3.4, where it can be seen that precipitation is possible in the region in which the orange surface $\mathfrak{S}_2$ lies above the black surface $\mathfrak{S}_1$. Furthermore, precipitation is thermodynamically permissible for all $\xi \in \mathrm{R}$ such that $\mathfrak{S}_2(b) > 1$, which occurs for all $\xi = n \in \mathbb{Z}$, while it can never occur for $\mathfrak{S}_2(b) < -1$, where $\xi = {}^n\!/_2$ for $n \in \mathbb{Z}$. The values of b demarcating these distinct regions can be found numerically by solving

$$\mathfrak{B}(b) - 1 = 0, \quad \mathfrak{B}(b) + 1 = 0,$$

yielding $b_- \approx -0.5378$ ($\approx 10.935\,\mathrm{km}$) and $b_+ \approx -0.5266$ ($\approx 10.959\,\mathrm{km}$), respectively at $x = 0$, and $t = 0$.

Consequently we have shown that precipitation is thermodynamically possible for all $\xi \in \mathbb{R}$ as long as $b \in [b_*, b_-)$, while it is never possible for $b \in (b_+, b_0]$. However, within the interval $b \in [b_-, b_+]$ we find $-1 \leq \mathfrak{B}(b) \leq 1$, while the

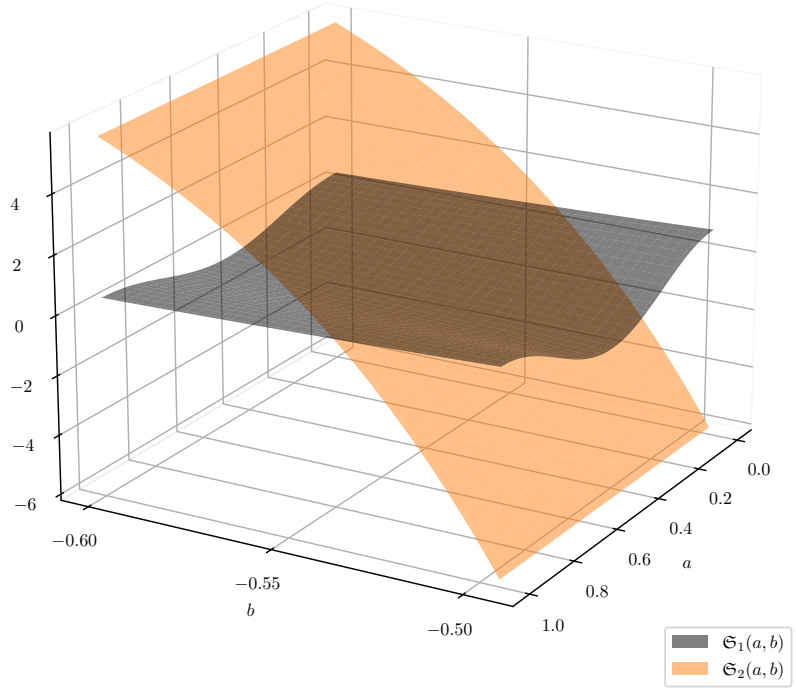

Figure 3.4: Surfaces $\mathfrak{S}_1(a,b)$ from (3.38b) (black) and $\mathfrak{S}_2(a,b)$ from (3.38c) (orange). Precipitation is consistent with the second law of thermodynamics in regions where $\mathfrak{S}_1 < \mathfrak{S}_2$.

inequality (3.39) is satisfied within intervals of the form

$$nk - \arccos(\mathfrak{B}(b)) < k\xi < nk + \arccos(\mathfrak{B}(b)), \quad n \in \mathbb{N}.$$

A contour plot of the function $\mathfrak{B}(b) - \cos(k\xi)$ at an initial time $t = 0$ is shown in Fig. 3.5, where the level set $\mathfrak{B}(b) - \cos(ka) = 0$ is shown in black. The grey region beneath this level-set corresponds to the region where precipitation is thermodynamically possible.

In this section it has been found that the inequality (3.35) following from the second law of thermodynamics may be explicitly formulated according to equation (3.36). Dry–air in the sense used in references [23] means an absence of condensation, in which case the term $\frac{\mathrm{D}}{\mathrm{D}t}\ln(1-q_1)$ vanishes, so that the second law of thermodynamics places a lower bound on the quantity appearing in the inequality (3.37) and so defines an implicit curve in the labelling domain. Along this implicit curve, it is found that $\frac{\mathrm{D}S}{\mathrm{D}t} = 0$, so that this curve represents the upper–boundary of the labelling domain where precipitation may take place.

A significant advantage of the explicit formulation of (3.6) in Lagrangian labelling variables, is that it allows us to plot particle trajectories governed by this

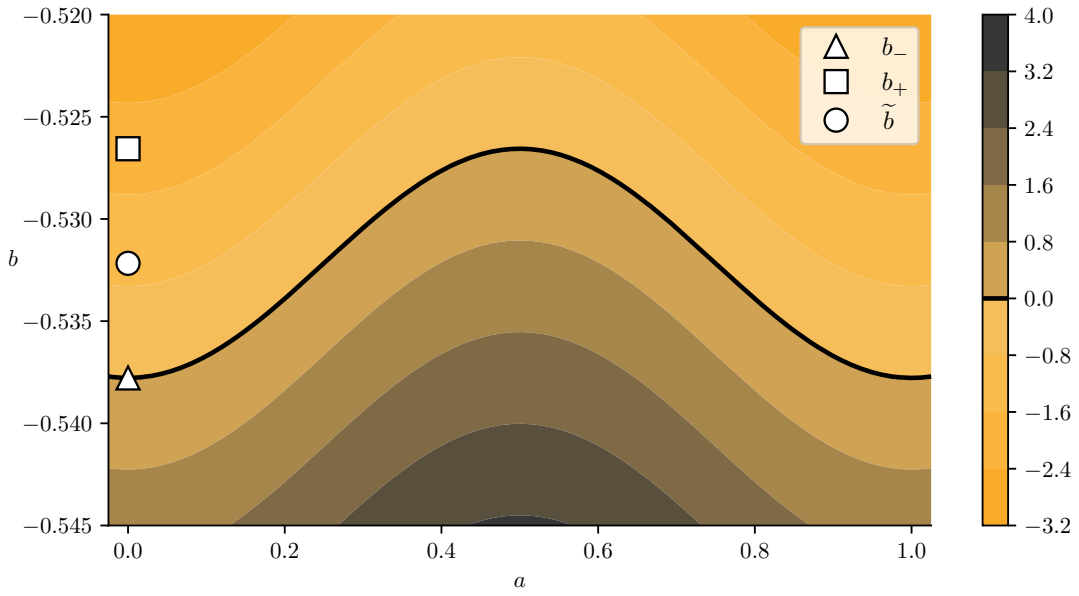

Figure 3.5: Contour plot of $\mathfrak{B}(b) - \cos(k\xi)$ at time $t = 0$ on the labelling domain $(a, b) \in (0, 1) \times [-0.545, -0.52]$, with the level set $\mathfrak{B}(b) - \cos(k\xi) = 0$ shown in black. As time evolves, this level set translates to the right through the fixed labelling domain, so that for any particle with $b \in (b_-, b_+)$ precipitation is thermodynamically admissible intermittently.

nonlinear flow, as illustrated in Fig. 3.6.

3.6 Nonlinear temperature-dependent enthalpy

In [75], the enthalpy of vaporisation was approximated by enforcing a linear dependence on temperature, however when compared with experimental data from [9, 71] for temperatures relevant to meteorological calculations, both the constant ΔH_{vap} and the linear $\Delta H_{vap}(\mathscr{T})$ have errors of approximately 2.9% and 0.03% respectively. For evaporation (or condensation) on small scales such errors are unlikely to be significant, however for phenomena on a global scale any error in the value for enthalpy can lead to a significant error in the calculation of energy lost (or gained) by the surrounding environment. It is for this reason that Henderson-Sellers [45], derived the following nonlinear temperature-dependent function for the enthalpy of vapourisation of water

$$\Delta H'_{\text{vap}}(\mathscr{T}') = \eta' \left(\frac{\mathscr{T}'}{\mathscr{T}' - \alpha'} \right)^2, \tag{3.40}$$

where $\eta' := 1.918\,46 \times 10^6\,\text{J}\,\text{kg}^{-1}$ and $\alpha' := 33.91\,\text{K}$. Equation (3.40) is accurate to within 0.02% between 273 K to 303 K, justifying its use as an approximation for the enthalpy of vaporisation of water over the simpler linear approximation.

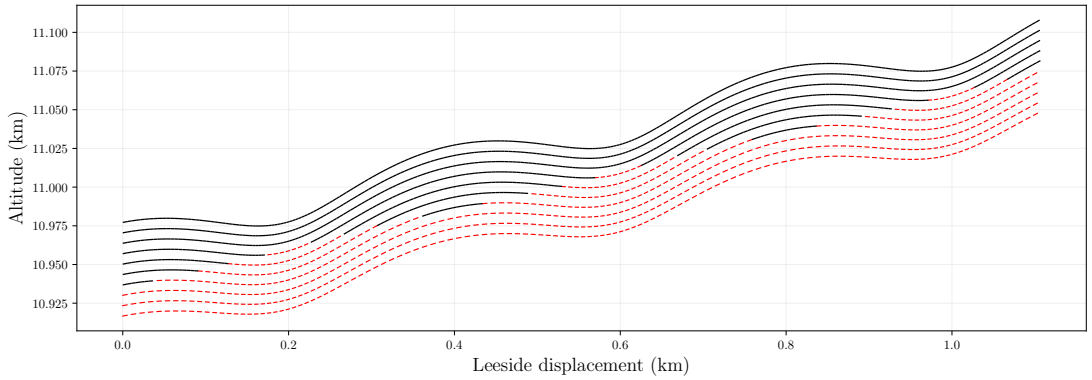

Figure 3.6: Particle trajectories in the physical domain. The dashed red lines denote the region where precipitation is thermodynamically admissible, determined by (3.39). For $b \in (b_-, b_+)$ precipitation occurs intermittently.

Nondimensionalising the constants α' and η' we find that

$$\alpha = \alpha' \frac{\mathfrak{R}_\mathrm{d}}{U^2} \approx 24.34, \quad \eta = \eta' \frac{\mathfrak{R}_\mathrm{d}}{\mathfrak{R}_\mathrm{v} U^2} \approx 2983.69.$$

Substituting these constants into (3.40), we find that the nondimensionalised enthalpy function for the vapourisation of water due to Henderson-Sellers is given by

$$\Delta H_\mathrm{vap}(\mathscr{T}) = \eta \left(\frac{\mathscr{T}}{\mathscr{T} - \alpha} \right)^2 .$$

Since we are interested in the range of temperatures for which the condensation of water vapour occurs in the atmosphere, it is assumed that $\mathscr{T} > \alpha$. Incorporating this nonlinear temperature-dependent form for the enthalpy of vapourisation into the Clausius-Clapeyron equation (3.17a), and integrating over the saturated domain, leads to the following expression for saturation pressure,

$$e_s(\mathscr{T}) = e_{s,*} \exp\left\{ \frac{\eta\,(\mathscr{T} - \mathscr{T}_*)}{(\mathscr{T} - \alpha)(\mathscr{T}_* - \alpha)} \right\}. \tag{3.41}$$

The dynamics of the flow lead to the pressure distribution (3.16) which must hold throughout the flow, and thus by Dalton's law of partial pressures, the saturation pressure for the water vapour component of the flow must be of the form

$$e_s(b) = e_{s,*} \exp\left\{ -g \int_{b_*}^{b} \frac{J(s)}{\mathscr{T}(s)} \,\mathrm{d}s \right\}.$$

Equating these two distinct expressions for the saturated vapour pressure e_s, and taking the natural logarithm leads to

$$\frac{\eta\,(\mathscr{T} - \mathscr{T}_*)}{\beta(\mathscr{T} - \alpha)} = -g \int_{b_*}^{b} \frac{J(s)}{\mathscr{T}(s)} \,\mathrm{d}s\,,$$

where $\beta \coloneqq \mathscr{T}_* - \alpha$. Differentiating with respect to the labelling variable b,

$$\frac{\mathscr{T}(b)}{\left(\mathscr{T}(b)-\alpha\right)^2}\frac{\mathrm{d}\mathscr{T}}{\mathrm{d}b} = -\frac{g}{\eta}J(b)$$

and integrating leads to

$$\left(\frac{\mathscr{T}(b)-\alpha}{\beta}\right)\exp\left\{\frac{\alpha}{\beta} - \frac{\alpha}{\mathscr{T}(b)-\alpha}\right\} = \exp\left\{-\frac{g}{\eta}\int_{b_*}^{b} J(s)\,\mathrm{d}s\right\},$$

which can be rewritten in the form

$$\left(\frac{\alpha}{\mathscr{T}(b)-\alpha}\right)\exp\left\{\frac{\alpha}{\mathscr{T}(b)-\alpha}\right\} = \frac{\alpha}{\beta}\exp\left\{\frac{\alpha}{\beta} + \frac{g}{\eta}\int_{b_*}^{b} J(s)\,\mathrm{d}s\right\}.$$

This can be solved explicitly for the virtual temperature $\mathscr{T}(b)$ in terms of the Lambert W function

$$\mathscr{T}(b) = \alpha\left(1 + \frac{1}{W(f(b))}\right), \tag{3.42}$$

where

$$f(b) \coloneqq \frac{\alpha}{\beta}\exp\left\{\frac{\alpha}{\beta} + \frac{g}{\eta}\int_{b_*}^{b} J(s)\,\mathrm{d}s\right\} > 0. \tag{3.43}$$

The enthalpy of vapourisation can then also be written in terms of the Lambert W function as

$$\Delta H_v(b) = \eta\left(W(f(b)) + 1\right)^2.$$

3.6.1 Precipitation in nonlinear mountain waves

Prior to saturation, it is assumed that moist air being forced upwards by mountainous terrain is elevated adiabatically, as in [16, 50]. The decrease in temperature of the air parcel associated with this forced ascent leads to a rise in its relative humidity $\mathfrak{h} = {}^{e}/_{e_s}$. If the air is cooled sufficiently such that $\mathfrak{h} = 1$, the air is said to be saturated and depending on the prevailing conditions, any further cooling may lead to the condensation of water vapour into liquid water or the deposition of water vapour directly into ice. To determine the temperature $\mathscr{T}_*$, at which saturation is attained, we proceed as in §3.5.2, and use the integral equation (3.29) which relates the saturation temperature and relative humidity, yielding

$$\mathfrak{h} = \left(\frac{\mathscr{T}}{\mathscr{T}_*}\right)^{\frac{1}{\mu\varepsilon}}\exp\left\{\frac{\mathscr{T}_* - \mathscr{T}}{\left(\mathscr{T}_*-\alpha\right)\left(\mathscr{T}-\alpha\right)}\right\}. \tag{3.44}$$

In contrast to the saturation temperature profile found in [75] which considered a linear function for ΔH, here it cannot be defined explicitly in terms of the initial temperature and relative humidity. Another approximate, but simpler,

approximation was given in [6] as

$$T_* \approx \frac{1}{\frac{1}{T-55} - \frac{\ln(\mathfrak{h})}{2840}} + 55. \tag{3.45}$$

A numerical comparison between the saturation temperature profile derived here (3.44), with those developed in [75], and by Bolton (3.45) is given in Fig.3.7.

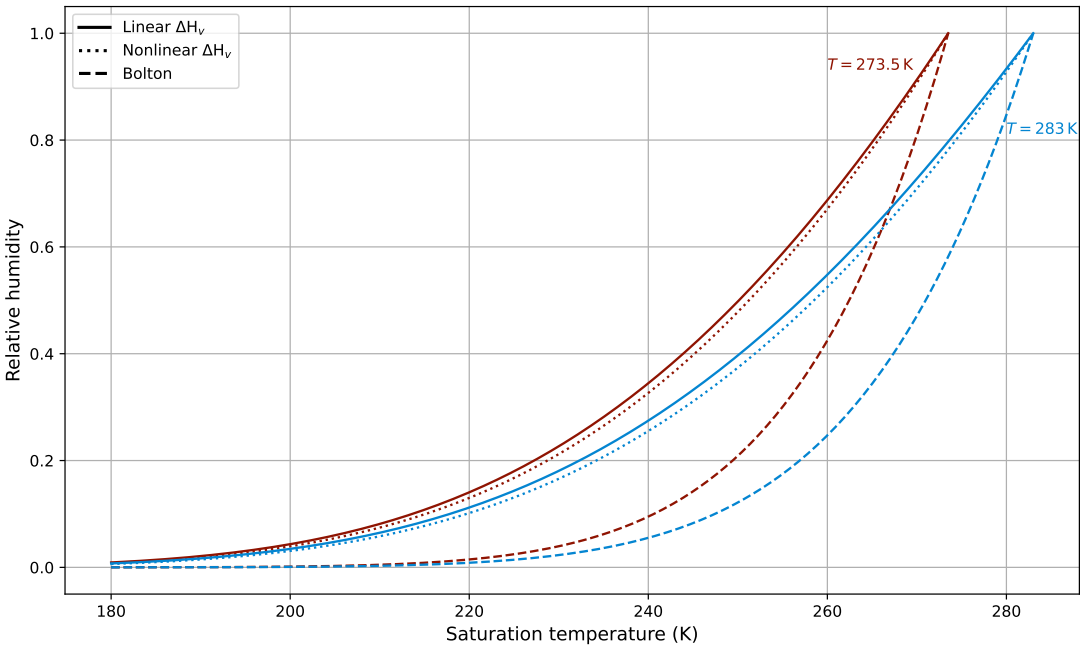

Figure 3.7: Comparison of three approximations for the saturation temperature $\mathscr{T}_*$, evaluated at temperatures $\mathscr{T} = 273.5\,\mathrm{K}$ (red) and $\mathscr{T} = 283\,\mathrm{K}$ (blue). The profile (3.44) derived here from a nonlinear enthalpy of vaporisation is shown as dotted curves (···), the profile from [75] using a linear enthalpy as solid curves (—), and Bolton's approximation (3.45) as dashed curves (- -). At relative humidity $\mathfrak{h} = 1$ the saturation temperature coincides with the physical temperature.

3.6.2 Entropy

Precipitation is thermodynamically admissible only in regions in which the second law of thermodynamics is adhered to. This reduces to the condition that

$$\frac{\mathrm{D}S}{\mathrm{D}t} = \frac{\dot{Q}}{\mathscr{T}} > 0,$$

(see the discussion in [75]) and since the temperature $\mathscr{T}$ is measured in Kelvin and thus positive, it must be the case that $\dot{Q} > 0$ during active precipitation. The additional contributions to the change in heat energy considered here are due to latent heat released during condensation $\dot{Q}_C$, and the heat diffused throughout

the surrounding dry-air $\dot{Q}_D$, where

$$\dot{Q} = \dot{Q}_D + \dot{Q}_C = \kappa \frac{\nabla^2 \mathscr{T}}{\mathscr{T}} + \frac{\Delta H}{\mathscr{T}} \frac{\mathrm{D}}{\mathrm{D}t} \ln(1 - q_\mathrm{s}) > 0,$$

cf. [41, 4].

As described in [75], when the heat loss to diffusion is precisely matched by the heat gain to condensation then

$$\frac{\Delta H}{\mathscr{T}} \frac{\mathrm{D}}{\mathrm{D}t} \ln(1 - q_\mathrm{s}) = -\kappa \frac{\nabla^2 \mathscr{T}}{\mathscr{T}} \geq 0, \tag{3.46}$$

since physically, $\frac{\mathrm{D}}{\mathrm{D}t} \ln(1 - q_s)$ must be positive during active precipitation. This leads to a subregion implicitly defined by $\nabla^2 \mathscr{T}(b) < 0$ in which precipitation is admissible by the second law of thermodynamics. It should be noted that this inequality does not restrict vapour in the atmosphere from condensing at a faster rate, instead the inequality defines an implicit curve in the labelling domain (a, b) on which $\frac{\mathrm{D}S}{\mathrm{D}t} = 0$, and thus demarcates the troposphere into two regions, one in which precipitation is admissible according to entropy considerations, and one where it is not.

In section §3.6.1, an explicit expression (3.42) was found for the temperature distribution within the saturated fluid domain. The laplacian for this temperature distribution, which is univariate in the labelling variable b is given by

$$\mathscr{T}_{xx} + \mathscr{T}_{zz} = \left[(b_x)_a \, a_x + (b_z)_a \, a_z + (b_x)_b \, b_x + (b_z)_b \, b_z \right] \mathscr{T}_b + \left[b_x^2 + b_z^2 \right] \mathscr{T}_{bb},$$

and can be calculated using (3.10), yielding

$$\nabla^2 \mathscr{T} = \frac{4ke^{2kb} \left(1 - e^{kb} \cos(k\xi)\right)}{(1 - e^{2kb})^3} \mathscr{T}_b + \frac{1 + e^{2kb} - 2e^{bk} \cos(k\xi)}{(1 - e^{2kb})^2} \mathscr{T}_{bb},$$

and rewritten as

$$\nabla^2 \mathscr{T} = \frac{1}{J} \left(2 \left(1 - e^{kb} \cos(k\xi)\right) \frac{\mathrm{d}}{\mathrm{d}b} \left(\frac{\mathscr{T}_b}{J} \right) - \mathscr{T}_{bb} \right). \tag{3.47}$$

Using the relations

$$\frac{f'(s)}{f(s)} = \frac{g}{\eta} J(s), \qquad \frac{\mathrm{d}}{\mathrm{d}s} W(f(s)) = \frac{f'(s)}{f(s)} \frac{W(f(s))}{(1 + W\left(f(s)\right))},$$

where $f(s)$ is as defined in (3.43), leads to the following relations for first and second order derivatives of the temperature distribution within the saturated

domain

$$\mathscr{T}_b = -\frac{gJ}{\eta} \cdot \frac{(\mathscr{T} - \alpha)^2}{\mathscr{T}}, \tag{3.48}$$

$$\mathscr{T}_{bb} = \mathscr{T}_b \left(\frac{J_b}{J} - \frac{gJ\left(\mathscr{T}^2 - \alpha^2\right)}{\eta \mathscr{T}^2} \right). \tag{3.49}$$

Substituting equations (3.48) and (3.49) into (3.47), the inequality $\nabla^2 \mathscr{T} < 0$ implicitly defines a region in the labelling domain in which precipitation can occur, and is given by

$$\cos(k\xi) > \cosh(kb) + \frac{k\eta \mathscr{T}^2}{2g\left(\mathscr{T}^2 - \alpha^2\right)\sinh(kb)}.$$

3.6.3 Dew-point temperature in the flow

Relative humidity and dew point temperatures are regularly used as more accessible data values in mountain meteorology. Using the Henderson-Sellers model of enthalpy of vapourisation, we may deduce the dew point along any other streamline in the flow, given its temperature $\mathscr{T}$ and relative humidity. The dew point temperature of a fluid parcel at temperature and pressure $\mathscr{T}$ and $e(\mathscr{T})$ respectively, is the temperature $\mathscr{T}_{\mathrm{D}}$ defined according to

$$e_s(\mathscr{T}_{\mathrm{D}}) = e(\mathscr{T}),$$

which a parcel at virtual temperature $\mathscr{T}$ must cool down to in order to become saturated. At the same time the relative humidity is defined by $\mathfrak{h} = {}^{e(\mathscr{T})}/_{e_s(\mathscr{T})}$, so that

$$\mathfrak{h} = \frac{e_s(\mathscr{T}_{\mathrm{D}})}{e_s(\mathscr{T})} \implies \mathscr{T}_{\mathrm{D}} = e_s^{-1}\left(\mathfrak{h} e_s(\mathscr{T})\right).$$

Given the saturation pressure $e_s(\mathscr{T}(b))$ deduced from the Henderson-Sellers enthalpy of vapourisation, the inverse of this saturation pressure may be applied along a streamline with vapour pressure $e(\mathscr{T})$ and relative humidity , to deduce the corresponding dew point temperature

$$\mathscr{T}_{\mathrm{D}} = \frac{\alpha\beta \ln\left(\frac{\mathfrak{h} e_s(\mathscr{T})}{e_{s,*}}\right) - \eta \mathscr{T}_*}{\beta \ln\left(\frac{\mathfrak{h} e_s(\mathscr{T})}{e_{s,*}}\right) - \eta}.$$

Moreover, in principle this estimate for dew-point temperature also allows us to estimate the actual vapour pressure in the flow since $e_s(\mathscr{T}_{\mathrm{D}}) = e_s(\mathscr{T})$, by definition. However, it is also the case that we require a specific distribution for the relative humidity, in which case we can also calculate the vapour pressure according to $e(\mathscr{T}) = \mathfrak{h} e_s(\mathscr{T})$.

At sea-level, a typical relative humidity is $\mathfrak{h}_1 = 0.77$, while the mean temperature is 288.15 K, whose associated saturation pressure is 17.04 mbar, while the atmospheric pressure is 1.013 bar. In non-dimensionalised variables these values are $T_1 = 206.8$, $P_1 = 253.3$, $e_{s,1} = 4.264$. The relative humidity and saturation pressure mean the vapour pressure is $e_1 = \mathfrak{h}_1 e_{s,1} = 3.285$ which in turn yields a virtual temperature $\mathscr{T}_1 = 207.8$. This now means

$$\mathscr{T}_{\mathrm{D},1} = e_s^{-1}\left(\mathfrak{h}_1 e_{s,1}\right) \approx 9.6\,^{\circ}\mathrm{C},$$

while the vertical profile of the dew point temperature may be deduced upon choosing an appropriate distribution for the relative humidity $\mathfrak{h}$. In this regard, the work of Manabe and Wetherald [77] proposes a relative humidity distribution which is linear in atmospheric pressure P', given by

$$\mathfrak{h} = \mathfrak{h}_1 \frac{\frac{P'}{P'_1} - 0.02}{1 - 0.02}.$$

Using the standard atmospheric distribution of temperature and pressure, combined with the saturated temperature distribution (3.41) deduced from the Henderson-Sellers nonlinear enthalpy of vapourisation, we are now able to provide the estimated dew temperature at other altitudes within the troposphere. The estimated dew point distribution and the standard atmosphere temperature distributions are compared in Figure 3.8a. It is clear from Figs. 3.8a–3.8b that dew point tem-

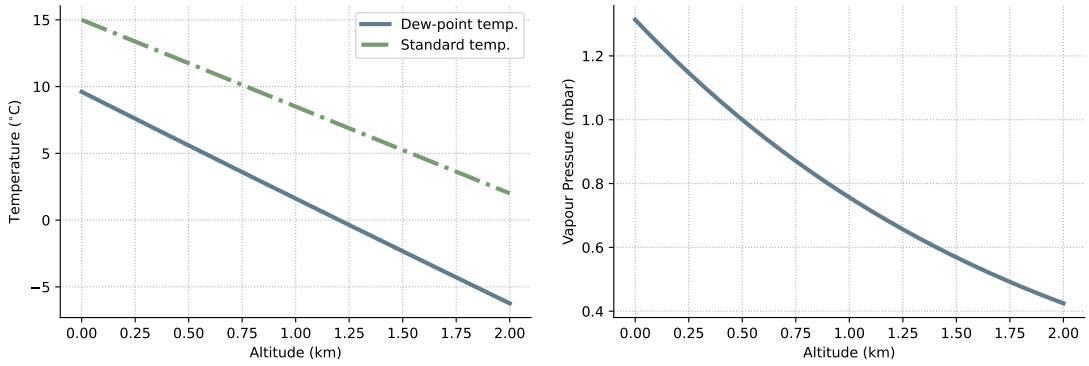

(a) The dew point temperature profile

(b) The vapour pressure profile

Figure 3.8: Estimated distributions of (a) the dew-point temperature $\mathscr{T}_{\mathrm{D}} = e_s^{-1}\left(\mathfrak{h}\, e_s(\mathscr{T})\right)$ and (b) the vapour pressure $e(\mathscr{T}) = e_s(\mathscr{T}_{\mathrm{D}})$, shown in physical units.

perature and the standard atmospheric temperature diverge with altitude while the vapour pressure also decreases with altitude, meaning the moisture decreases with altitude, as expected.

3.6.4 Deposition

The atmospheric process of snow formation involves the deposition of water vapour to ice and the freezing of liquid water into ice. Only the first of these processes will be examined here, since the liquid water can no longer be realistically considered an ideal gas and so it outside the scope of the equation of state (3.3) used here. In dimensional variables, the enthalpy associated with this phase change is given by

$$\Delta\mathcal{H}' = 46782.5 + 35.8925T' - 0.07414T'^2 + 541.5\exp\Big\{-(T'/123.75)^2\Big\}, \quad T' > 30\,\mathrm{K},$$

with $\Delta\mathcal{H}'$ having units of $\mathrm{J\,mol^{-1}}$ (see [91] for further detail). With $\Delta\mathcal{H}$ scaling according to $\Delta\mathcal{H} = \frac{\mathfrak{R}_\mathrm{d}}{U'^2\mathfrak{R}_\mathrm{v}}\Delta\mathcal{H}'$ under non-dimensionalisation, it now follows that the non-dimensionalised enthalpy of sublimation may be written as

$$\Delta\mathcal{H} = h_0 + h_1\mathscr{T} - h_2\mathscr{T}^2 + he^{-(\mathscr{T}/\mathscr{T}_0)^2}, \quad \mathscr{T} \gtrsim 41.8,$$

where $h_0 \approx 8.64 \times 10^{-3}$, $h_1 \approx 4.33$, $h_2 \approx 1.25 \times 10^{-2}$, $h \approx 46.8$ and $\mathscr{T}_0 \approx 88.8$. The non–dimensionalised Clausius–Clapeyron equation now becomes

$$\frac{\mathrm{d}}{\mathrm{d}\mathscr{T}}\ln(e_\mathrm{s}) = \frac{\Delta\mathcal{H}}{\mathscr{T}^2},$$

so the the saturation pressure is

$$e_\mathrm{s}(\mathscr{T}) = e_{\mathrm{s},*}\exp\left\{\int_{\mathscr{T}_*}^{\mathscr{T}} \frac{\Delta\mathcal{H}}{\mathscr{T}^2}\,\mathrm{d}\mathscr{T}\right\},$$

$$\begin{aligned}\int_{\mathscr{T}_*}^{\mathscr{T}} \frac{\Delta\mathcal{H}}{\mathscr{T}^2}\,\mathrm{d}\mathscr{T} = h_0\left(\frac{1}{\mathscr{T}_*} - \frac{1}{\mathscr{T}}\right) + h_1\ln\left(\frac{\mathscr{T}}{\mathscr{T}_*}\right) + h_2\left(\mathscr{T} - \mathscr{T}_*\right) \\ + \frac{h}{\mathscr{T}_0}\left(\frac{1}{\theta_*}e^{-\theta_*^2} - \frac{1}{\theta}e^{-\theta^2} + \sqrt{\pi}\left(\mathrm{erf}(\theta_*) - \mathrm{erf}(\theta)\right)\right),\end{aligned} \tag{3.50}$$

where $\mathrm{erf}(\cdot)$ is the error function (see [42] for instance) with $\theta = \mathscr{T}/\mathscr{T}_0$ and the boundary conditions are $e_{\mathrm{s},*} = e_s(\mathscr{T}_*)$ and $\theta_* = \mathscr{T}_*/\mathscr{T}_0$. Given Dalton's Law (cf. equation (3.16)) and the saturation pressure $e_s(\mathscr{T})$ (cf. equation (3.50)), there are now two expressions for the saturation pressure of water vapour when in equilibrium with the ice phase of water, requiring

$$e_{\mathrm{s},*}\exp\left\{-g\int_{b_*}^{b}\frac{J(s)}{\mathscr{T}(s)}\,\mathrm{d}s\right\} = e_{\mathrm{s},*}\exp\left\{\int_{\mathscr{T}_*}^{\mathscr{T}(b)}\frac{\Delta\mathcal{H}}{\mathscr{T}^2}\,\mathrm{d}\mathscr{T}\right\}.$$

Differentiation with respect to b now yields

$$-gJ(b) = \frac{\Delta\mathcal{H}(\mathscr{T}(b))}{\mathscr{T}(b)}\frac{\mathrm{d}\mathscr{T}}{\mathrm{d}b}, \tag{3.51}$$

so that upon integrating we attain an implicit relation for $\mathscr{T}(b)$ given by

$$\begin{aligned}-g\left[b - b_* - \frac{e^{2kb} - e^{2kb_*}}{2k}\right] = h_0 \ln\left(\frac{\mathscr{T}(b)}{\mathscr{T}_*}\right) + h_1\left(\mathscr{T}(b) - \mathscr{T}_*\right) \\ - \frac{h_2}{2}\left(\mathscr{T}(b)^2 - \mathscr{T}_*^2\right) + \frac{h}{2}\left(\mathrm{E}_1\left(\theta(b)^2\right) - \mathrm{E}_1\left(\theta_*^2\right)\right),\end{aligned} \tag{3.52}$$

where $\theta(b) = \mathscr{T}(b)/\mathscr{T}_0$, $\mathscr{T}(b_*) = \mathscr{T}_*$ and $\mathrm{E}_1(x) = \int_x^\infty u^{-1}e^{-u}\,\mathrm{d}u$ is the exponential integral (see [42] for example).

In this instance it is no longer possible to find an explicit expression for the temperature distribution in a saturated atmosphere, however it is still possible to obtain an implicit expression for $\mathscr{T}(b)$. Given the general expression (3.47) for $\nabla^2\mathscr{T}$ when $\mathscr{T}(b)$ is a univariate temperature distribution, thermal diffusion in a saturated atmosphere in equilibrium between the vapour and ice phases is given by

$$\nabla^2\mathscr{T} = \frac{1}{J}\left(\frac{\mathrm{d}}{\mathrm{d}b}\left(\frac{gJ}{\Delta\mathcal{H}}\right) - 2\left(1 - e^{kb}\cos(k\xi)\right)\frac{\mathrm{d}}{\mathrm{d}b}\left(\frac{g}{\Delta\mathcal{H}}\right)\right),$$

where equation (3.51) was used to re–write T_b. While entropy change is required to satisfy equation (3.46), we may re-write this equation according to

$$\Delta\mathcal{H}\frac{\mathrm{D}}{\mathrm{D}t}\ln(1 - q_s) = -\kappa\nabla^2\mathscr{T} \geq 0,$$

so that $\nabla^2\mathscr{T} = 0$ imposes an additional implicit relation defining the boundary above which deposition is no longer possible. Given equations (3.52) and $\nabla^2\mathscr{T} = 0$ we now find

$$2ke^{2kb} + g(1 - e^{2kb})\left(\frac{h^0 + h_2\mathscr{T}^2 + h(1+\theta^2)e^{-\theta^2}}{\Delta\mathcal{H}^2}\right)\left(2e^{kb}\cos(k\xi) - (1 + e^{2kb})\right) = 0 \tag{3.53}$$

which serves to define $\mathscr{T}$ implicitly in terms of the Lagrangian variables (a, b). Equations (3.52) and (3.53) may be used to implicitly define the curve in the (a, b)–domain along which $\frac{\mathrm{D}S}{\mathrm{D}t} = 0$, with this curve being the upper boundary of the fluid domain where deposition and snow fall may occur.

Chapter 4

Flow underlying coupled surface and internal waves with lower layer vorticity

The material presented in this chapter is based on an article[1] that is currently in an advanced stage of preparation. In this chapter we study the flow induced by coupled surface and internal small-amplitude water waves in a two-layer fluid model, in which the upper layer is assumed to be irrotational, while the lower layer carries constant vorticity γ. Both adverse ($\gamma < 0$) and favourable ($\gamma > 0$) vorticities are considered. The underlying flow generated by waves and wave-current interactions in a single fluid layer, in both the linear and nonlinear settings, has been the subject of extensive study in recent years [11, 36, 72], see also [12] and the references therein. The two-layer setting has also received considerable attention, and the investigations carried out to date have treated either the case in which both fluid layers are separately irrotational [54, 55], or the case in which the upper layer carries nonzero vorticity while the lower layer remains irrotational [51]. The relative absence of results concerning fluid flow in the presence of wave-current interactions with a rotational lower fluid layer provides the principal motivation for the work presented here.

Two-layer fluid configurations arise whenever a significant vertical density difference leads to stratification of the fluid, typically as a result of variations in salinity, temperature, or other physical factors [104]. In the ocean, water columns are frequently observed to have nearly constant density outside of thin transition layers, giving rise to an internal interface between the two layers, known as a pycnocline, or a thermocline when the density variation is driven by temperature differences, together with the internal waves that propagate along it. Internal waves play a fundamental role in the description of large-scale ocean dynamics, but are inherently difficult to observe and measure directly [19, 70], underlining

[1] Devine, D., McCarney, J., Flow underlying coupled surface and internal water waves with a rotational lower layer.

the relevance and importance of rigorous theoretical studies in this setting.

The chapter is structured as follows. After formulating the governing equations in Section 4.1, in Section 4.2 we employ a classical linearisation procedure [63] together with variational techniques developed in [19] to recast the problem within a Hamiltonian framework. Although the equations of motion are linearised in the fluid-dynamical sense, the resulting dynamical system describing the fluid flow is nonlinear, and its analysis forms the central mathematical content of the chapter. In Section 4.4 we derive the dispersion relation for the wave speeds of the coupled surface and internal waves, which takes the form of a quartic polynomial in the phase speed c. The presence of vorticity in the lower layer complicates matters considerably from a mathematical perspective: in the irrotational setting, the analogous dispersion relation is quadratic in c^2 [54, 104], and is therefore far more tractable. A detailed analysis of the roots of the quartic dispersion relation turns out to be essential to understanding the flow in both fluid layers, and is carried out in detail. In Section 4.5 we then conduct a phase-plane analysis of the underlying flow from an Eulerian perspective, and finally in Section 4.6 we study the particle trajectories themselves from the Lagrangian viewpoint, establishing qualitative results on drift behaviour and the existence of closed particle paths.

4.1 Equations of motion

We consider here a two-dimensional water flow, moving under the influence of gravity, and use a reference frame with horizontal x axis, and y axis that points vertically upwards. The water flow occupies the domain bounded below by the rigid at bed $y = -h$, (with $h > 0$), and above by the free surface $y = \eta_1(x,t) + h_1$, the latter being a perturbation of the flat free surface $y = h_1$. Here, $h_1 > 0$ is a constant, while $\eta_1(x,t)$ is a periodic function in x of period $L > 0$ which has mean zero, that is, for all t

$$\int_0^L \eta_1(x,t)dx = 0.$$

The fluid is assumed to be stratified into two layers of differing piecewise constant densities, and so $\boldsymbol{\rho} = \rho_1$ on the upper fluid layer $\Omega_1(\eta,\eta_1)$, where

$$\Omega_1(\eta,\eta_1) = \{(x,y) : x \in [0,L],\ \eta(x,t) < y < h_1 + \eta_1(x,t)\}$$

while $\boldsymbol{\rho} = \rho$ on the lower fluid layer $\Omega(\eta)$, where

$$\Omega(\eta) = \{(x,y) : x \in [0,L],\ -h < y < \eta(x,t)\}.$$

Here, $y = \eta(x,t)$ denotes the internal interface separating the two fluid layers, which we also take to be L-periodic in the x-variable with zero mean, so

$$\int_0^L \eta(x,t)dx = 0$$

for all t. We assume the fluid is stably stratified, so that $\rho_1 < \rho \equiv (1+r)\rho_1$ for some $r > 0$. In an oceanographical context, a reasonable value of r would be $r = \mathcal{O}(10^{-3})$ [19]. The velocity field of the fluid can therefore be split into

$$\boldsymbol{u}(x,y,t) = \begin{cases} u(x,y,t) & \text{in } \Omega(\eta), \\ u_1(x,y,t) & \text{in } \Omega_1(\eta,\eta_1), \end{cases}$$

and

$$\boldsymbol{v}(x,y,t) = \begin{cases} v(x,y,t) & \text{in } \Omega(\eta), \\ v_1(x,y,t) & \text{in } \Omega_1(\eta,\eta_1). \end{cases}$$

The equations of motion for an inviscid and incompressible fluid are the Euler equation, which can be expressed as

$$\begin{cases} \boldsymbol{u}_t + \boldsymbol{u}\boldsymbol{u}_x + \boldsymbol{v}\boldsymbol{u}_y = -\dfrac{1}{\boldsymbol{\rho}}P_x, \\ \boldsymbol{v}_t + \boldsymbol{u}\boldsymbol{v}_x + \boldsymbol{v}\boldsymbol{v}_y = -\dfrac{1}{\boldsymbol{\rho}}P_y - g, \end{cases}$$

where $P = P(x,y,t)$ denotes the pressure and g is the acceleration due to gravity. The incompressibility condition can be expressed as

$$\boldsymbol{u}_x + \boldsymbol{v}_y = 0 \quad \text{in} \quad \Omega \cup \Omega_1. \tag{4.1}$$

We denote the vorticity of the fluid by $\boldsymbol{\gamma} = \nabla \times \boldsymbol{U}$, where $\boldsymbol{U}$ is the velocity field of the fluid in each layer, which in our case becomes

$$\gamma = u_y - v_x \quad \text{in } \Omega \quad \text{and} \quad \gamma_1 = u_{1,y} - v_{1,x} \quad \text{in } \Omega_1.$$

We are interested here in the case where the fluid is irrotational in the upper layer, i.e $\gamma_1 = 0$, and the lower layer has constant non-zero vorticity $\gamma \neq 0$. When it comes to the boundary conditions, at the free surface $y = \eta_1(x,t) + h_1$ the dynamic boundary condition

$$P = P_{atm} \quad \text{on } y = \eta_1(x,t) + h_1,$$

decouples the water from the air. We take P_{atm}, the atmospheric pressure, to be constant. We have the following kinematic boundary conditions

$$v_1 = \eta_{1,t} + u_1\eta_{1,x} \quad \text{on } y = \eta_1(x,t) + h_1,$$

as well as

$$\begin{aligned} v_1 &= \eta_t + u_1\eta_x \quad \text{on } y = \eta(x,t), \\ v &= \eta_t + u\eta_x \quad \text{on } y = \eta(x,t), \end{aligned}$$

and

$$v = 0 \quad \text{on } y = -h.$$

The incompressibility condition (4.1) enables us to define the generalised velocity potential

$$\boldsymbol{\varphi}(x,y,t) = \begin{cases} \varphi(x,y,t) & \text{in } \Omega, \\ \varphi_1(x,y,t) & \text{in } \Omega_1, \end{cases}$$

by

$$\begin{cases} u = \varphi_x + \gamma y + \vartheta, & v = \varphi_y & \text{in } \Omega, \\ u_1 = \varphi_{1,x} + \vartheta, & v_1 = \varphi_{1,y} & \text{in } \Omega_1, \end{cases} \tag{4.2}$$

where both φ and φ_1 are L-periodic in x. When it comes to the additive constant ϑ in definition (4.2), by assuming the Stokes condition

$$\int_0^L u(x,-h,t)\, dx = 0,$$

we see that $\vartheta = \gamma h$ is the most natural choice. The kinematic boundary conditions can now be reexpressed in terms of the potential as

$$\eta_{1,t} = (\varphi_{1,y})_{s_1} - \eta_{1,x}((\varphi_{1,x})_{s_1} + \gamma h),$$

and

$$\eta_t = (\varphi_{1,y})_s - \eta_x((\varphi_{1,x})_s + \gamma h), \quad \eta_t = (\varphi_y)_s - \eta_x((\varphi_x)_s + \gamma(\eta + h)),$$

with s_1 denoting the trace at the free surface $y = \eta_1(x,t) + h_1$, and s denoting the trace on the interface $y = \eta(x,t)$. Finally, we shall denote

$$\begin{aligned} &\Phi(x,t) = \varphi(x,\eta(x,t),t), \quad \Phi_1(x,t) = \varphi_1(x,\eta(x,t),t), \\ &\Phi_2(x,t) = \varphi_1(x,\eta_1(x,t) + h_1, t). \end{aligned}$$

4.2 Linearisation of the equations

We now perform a nondimensionalisation and scaling of our variables. To this end, we assume the depths h and h_1 are roughly the same order of magnitude, allowing us to introduce a depth scale $\mathfrak{h}$ such that $h, h_1 = \mathcal{O}(\mathfrak{h})$. Similarly for the amplitudes of the surface and internal wave, a_1 and a, we introduce the amplitude length scale $\mathfrak{a}$, so that $a, a_1 = \mathcal{O}(\mathfrak{a})$. We define the dimensionless parameters

$$\epsilon = \frac{\mathfrak{a}}{\mathfrak{h}}, \quad \delta = k\mathfrak{h}, \quad \mathfrak{e} = k\mathfrak{a},$$

where $k = 2\pi/L$ is the wave number, and thus it follows that ϵ denotes the wave amplitude relative to the layer depth, δ measures the depth relative to the wavelength, and $\mathfrak{e}$ denotes the wave steepness parameter. The equations are linearised using the classical procedure of assuming $\epsilon, \mathfrak{e} \ll 1$ [63]. We assume $\delta = \mathcal{O}(1)$, and make the following changes of variables

$$\overline{h} = \mathfrak{h}h, \quad \overline{h}_1 = \mathfrak{h}h_1, \quad \overline{\varphi} = \frac{\epsilon}{\delta}\mathfrak{h}\sqrt{\overline{g}\mathfrak{h}}\varphi, \quad \overline{\varphi}_1 = \frac{\epsilon}{\delta}\mathfrak{h}\sqrt{\overline{g}\mathfrak{h}}\varphi_1, \quad \overline{\eta} = \epsilon\frac{\mathfrak{h}}{\delta}\eta, \quad \overline{\eta}_1 = \epsilon\frac{\mathfrak{h}}{\delta}\eta_1$$
$$(\overline{x}, \overline{y}, \overline{t}) = \frac{\mathfrak{h}}{\delta}\left(x, y, \frac{1}{\sqrt{\overline{g}\mathfrak{h}}}t\right), \quad \overline{\gamma} = \frac{\sqrt{\overline{g}\mathfrak{h}}}{\mathfrak{h}}\gamma, \quad (\overline{u}, \overline{v}) = \sqrt{\overline{g}\mathfrak{h}}(u, v).$$

Above, the dimensional variables have a bar over them. In the new non-dimensional variables, our boundary conditions then become

$$\begin{aligned}
\eta_{1,t} &= (\varphi_{1,y})_{s_1} - \eta_{1,x}(\epsilon(\varphi_{1,x})_{s_1} + \gamma h), \\
\eta_t &= (\varphi_{1,y})_s - \eta_x(\epsilon(\varphi_{1,x})_s + \gamma h), \\
\eta_t &= (\varphi_y)_s - \eta_x\left[\epsilon(\varphi_x)_s + \frac{\epsilon}{\delta}\gamma\eta + \gamma h\right].
\end{aligned}$$

Letting $\epsilon \to 0$, these equations are approximated by

$$\begin{aligned}
\eta_{1,t} &= (\varphi_{1,y})_{s_1} - \gamma h\eta_{1,x}, \\
\eta_t &= (\varphi_{1,y})_s - \gamma h\eta_x, \\
\eta_t &= (\varphi_y)_s - \gamma h\eta_x.
\end{aligned}$$

Furthermore, we have

$$\begin{aligned}
&\Phi(x,t) = \varphi(x, \epsilon\eta(x,t), t), \quad \Phi_1(x,t) = \varphi_1(x, \epsilon\eta(x,t), t), \\
&\Phi_2(x,t) = \varphi_1(x, \epsilon\eta_1(x,t) + h_1, t).
\end{aligned}$$

which, letting $\epsilon \to 0$, are approximated by

$$\begin{aligned} &\Phi(x,t) = \varphi(x,0,t), \quad \Phi_1(x,t) = \varphi_1(x,0,t), \\ &\Phi_2(x,t) = \varphi_1(x,h_1,t). \end{aligned} \tag{4.3}$$

The Hamiltonian for our physical set up is given by the total energy

$$H = \iint_{\Omega \cup \Omega_1} \boldsymbol{\rho} \left\{ \frac{\boldsymbol{u}^2 + \boldsymbol{v}^2}{2} + gy \right\} dydx.$$

This is the energy of the system over one period. The Hamiltonian variables we will use are η, η_1 and

$$\begin{aligned} \xi &= \frac{\rho\varphi(x,0,t) - \rho_1\varphi_1(x,0,t)}{\rho_1} \equiv (r+1)\Phi(x,t) - \Phi_1(x,t) \\ \xi_1 &= \varphi_1(x,h_1,t) \equiv \Phi_2(x,t). \end{aligned} \tag{4.4}$$

These are not strictly Hamiltonian variables in the usual sense, but we will use this language going forward since they are “nearly Hamiltonian". From [19], the Hamiltonian for our system admits an expansion of the form

$$H(\xi, \xi_1, \eta, \eta_1) = \epsilon^2 H^{(2)}(\xi, \xi_1, \eta, \eta_1) + \epsilon^3 H^{(3)}(\xi, \xi_1, \eta, \eta_1) + \cdots$$

The leading order term is (cf equation 4.15 in [19] with $\gamma_1 = 0$)

$$\begin{aligned} H^{(2)}(\xi, \xi_1, \eta, \eta_1) = \frac{1}{2}\int_0^L \Bigg[&\xi \frac{D\tanh(hD)}{(1+r) + \tanh(hD)\tanh(h_1 D)} \xi \\ &+ 2\xi \frac{D\tanh(hD)\operatorname{sech}(h_1 D)}{(1+r) + \tanh(hD)\tanh(h_1 D)} \xi_1 \\ &+ \xi_1 \frac{D\tanh(hD) + (1+r)D\tanh(h_1 D)}{(1+r) + \tanh(hD)\tanh(h_1 D)} \xi_1 \\ &+ (rg + \gamma^2 h(1+r))\eta^2 + g\eta_1^2 - 2\gamma h(\eta_x \xi + \eta_{1,x}\xi_1) \Big] dx, \end{aligned}$$

where $D = -i\partial_x$. The Hamiltonian equations have the form

$$\begin{aligned} &\epsilon^2 \eta_t = \frac{\delta H}{\delta \xi}, \qquad \epsilon^2 \xi_t = -\frac{\delta H}{\delta \eta} - (1+r)\gamma \int_0^x \frac{\delta H}{\delta \xi(x')} dx', \\ &\epsilon^2 \eta_{1,t} = \frac{\delta H}{\delta \xi_1}, \quad \epsilon^2 \xi_{1,t} = -\frac{\delta H}{\delta \eta_1}. \end{aligned}$$

At leading order, $H = \epsilon^2 H^{(2)}$, which yields the following

$$\begin{aligned}
\xi_t &= -(rg + \gamma^2 h(1+r))\eta - \gamma h \xi_x - (1+r)\gamma \partial_x^{-1}\eta_t, \\
\eta_t &= \frac{D\tanh(hD)\coth(h_1 D)}{(1+r)\coth(h_1 D) + \tanh(hD)}\xi \\
&\quad + \frac{D\tanh(hD)\mathrm{csch}(h_1 D)}{(1+r)\coth(h_1 D) + \tanh(hD)}\xi_1 - \gamma h \eta_x, \\
\xi_{1,t} &= -g\eta_1 - \gamma h \xi_{1,x}, \\
\eta_{1,t} &= \frac{D\tanh(hD)\mathrm{csch}(h_1 D)}{(1+r)\coth(h_1 D) + \tanh(hD)}\xi \\
&\quad + \frac{D[\tanh(hD)\coth(h_1 D) + (1+r)]}{(1+r)\coth(h_1 D) + \tanh(hD)}\xi_1 - \gamma h \eta_{1,x}.
\end{aligned} \tag{4.5}$$

4.3 Travelling wave solutions

We now determine the velocity potentials from their values on the surface and the interface, using the boundary values obtained in the previous section. We shall make use of the following standard Ansatz

$$\eta(x,t) = a\cos(kx - \omega t), \quad \eta_1(x,t) = a_1\cos(kx - \omega t). \tag{4.6}$$

To determine the velocity potential in the lower layer, we are led to the following boundary value problem:

$$\begin{aligned}
&\Delta\varphi = 0, \\
&\frac{\partial\varphi}{\partial \boldsymbol{n}} = 0 \text{ on } y = -h, \\
&\varphi_y(x,0,t) = \eta_t(x,t) + \gamma h \eta_x(x,t).
\end{aligned}$$

This has solution

$$\varphi(x,y,t) = \frac{a(c(k) - \gamma h)\cosh(k(y+h))}{\sinh(kh)}\sin(kx - \omega t), \tag{4.7}$$

where

$$c(k) = \frac{\omega(k)}{k},$$

is the phasespeed of the wave. The relevant boundary value problem in the upper layer is then

$$\begin{aligned}
&\Delta\varphi_1 = 0,\\
&\varphi_{1,y}(x,h_1,t) = \eta_{1,t}(x,t) + \gamma h \eta_{1,x}(x,t),\\
&\varphi_{1,y}(x,0,t) = \eta_t(x,t) + \gamma h \eta_x(x,t),
\end{aligned}$$

which has solution

$$\varphi_1(x,y,t) = a_1(c-\gamma h)[\sinh(k(y-h_1)) + A\cosh(k(y-h_1))]\sin(kx-\omega t), \quad (4.8)$$

where

$$A = \frac{1}{\sinh(kh_1)}\left(\cosh(kh_1) - \frac{a}{a_1}\right). \quad (4.9)$$

We now seek an expression for A which is independent of the quantity a/a_1. To this end, using (4.3) and (4.8) we have

$$\xi_1(x,t) = \Phi_2(x,t) = \varphi_1(x,h_1,t) = a_1(c-\gamma h)A\sin(kx-\omega t).$$

Using the third equation in (4.5) and matching coefficients leads to

$$A = \frac{g}{k(c-\gamma h)^2}. \quad (4.10)$$

From (4.10), we clearly have $A > 0$. The exact value of A, in particular whether $A < 1$, $A = 1$ or $A > 1$, is crucial to studying the flow in the upper fluid layer Ω_1. It has recently been shown that in the irrotational case $\gamma = 0$, only values $A > 1$ can arise [52] . Theorem 4.4.1 below gives a new, more straight forward proof of this result. The situation is different when nonzero values of γ are permitted, however, as is shown in Theorem 4.4.2 below. Theorem 4.4.2 is therefore the first rigorous justification that values $A \leq 1$ are possible, and this can only occur for nonzero vorticity. We conclude this section with the following observation. From (4.9), since

$$\frac{a}{a_1} = \cosh(kh_1) - A\sinh(kh_1),$$

it is clear that

$$\frac{a}{a_1} > 0 \iff \coth(kh_1) > A,$$

which corresponds to the surface and internal wave being in-phase (see Figure 4.1). Likewise, the surface and internal waves are out of phase if and only if $A > \coth(kh_1)$, which cannot happen when $A \leq 1$. The equality $A = \coth(kh_1)$ corresponds to $a = 0$ and therefore $\eta \equiv 0$, i.e the case of no internal wave.

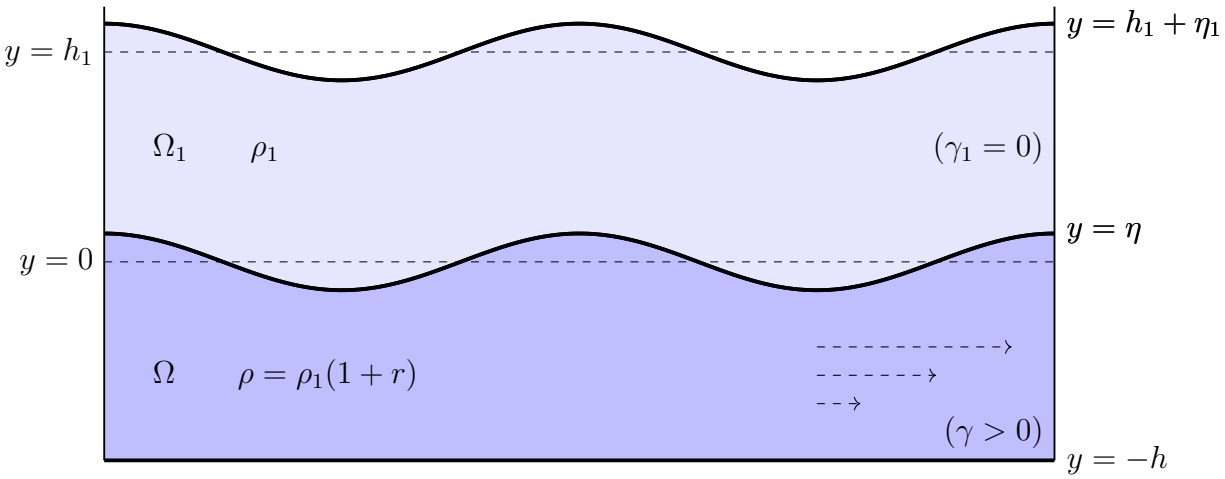

(a) In-phase surface and internal waves.

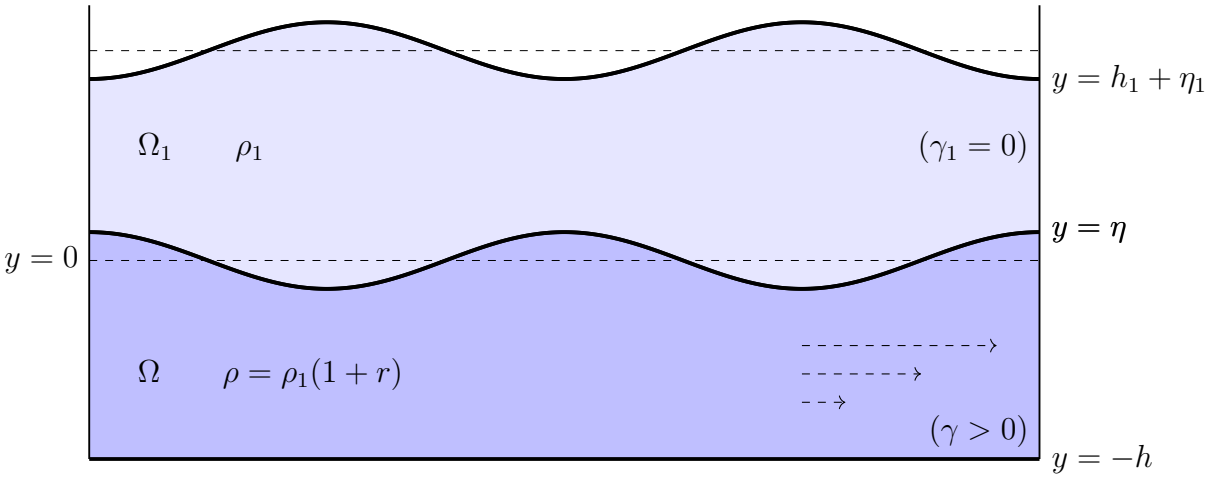

(b) Out-of-phase surface and internal waves.

Figure 4.1: Schematic of a stably stratified two-layer fluid model. The upper layer Ω_1 is irrotational, while the lower layer Ω carries constant vorticity γ. When the crests (troughs) of the surface wave lie directly above the crests (troughs) of the internal wave, the configuration is said to be *in-phase*, corresponding to $a/a_1 > 0$. When the crests (troughs) of the surface wave lie above the troughs (crests) of the internal wave, the configuration is *out-of-phase*, corresponding to $a/a_1 < 0$. The case $a/a_1 = 0$ implies that no internal wave is present.

4.4 Dispersion relation

In this section we derive the dispersion relation for the wavespeed c. Using our near Hamiltonian equations (4.5), together with our Ansatz (4.6), we conclude

$$\begin{aligned} \xi(x,t) &= a\frac{rg + \gamma(1+r)(\gamma h - c)}{k(c - \gamma h)}\sin(kx - \omega t), \\ \xi_1(x,t) &= \frac{ga_1}{k(c-\gamma h)}\sin(kx - \omega t). \end{aligned} \tag{4.11}$$

Turning to the definition of the variables ξ, ξ_1 (4.4), we also have from (4.7) and (4.8)

$$\begin{aligned}\xi(x,t) =& [(1+r)a(c-\gamma h)\coth(kh) + a_1(c-\gamma h)\sinh(kh_1) \\ & -Aa_1(c-\gamma h)\cosh(kh_1)]\sin(kx-\omega t), \\ \xi_1(x,t) =& a_1(c-\gamma h)A\sin(kx-\omega t).\end{aligned} \tag{4.12}$$

Equating (4.11) and (4.12), using our definition (4.9) and denoting $\mathfrak{c} = c - \gamma h$, after some algebra we have the following dispersion relation

$$\begin{aligned}&\left[1 + \frac{1+r}{\tanh(kh)\tanh(kh_1)}\right]\mathfrak{c}^4 + \frac{\gamma(1+r)}{k\tanh(kh_1)}\mathfrak{c}^3 \\ &- \frac{g(1+r)}{k}\left(\frac{1}{\tanh(kh)} + \frac{1}{\tanh(kh_1)}\right)\mathfrak{c}^2 - \frac{\gamma(1+r)g}{k^2}\mathfrak{c} + \frac{rg^2}{k^2} = 0,\end{aligned} \tag{4.13}$$

which we will denote by $P(\mathfrak{c}) = 0$. We make a few observations about the dispersion relation (4.13). Firstly, it is invariant under the change of variables $(c, \gamma) \mapsto (-c, -\gamma)$. Secondly, if we set $\gamma = 0$, then (4.13) reduces to

$$\left[1 + \frac{1+r}{\tanh(kh)\tanh(kh_1)}\right]c^4 - \left[\frac{g(1+r)}{k}\left(\frac{1}{\tanh(kh)} + \frac{1}{\tanh(kh_1)}\right)\right]c^2 + \frac{rg^2}{k^2} = 0, \tag{4.14}$$

which is the well known dispersion relation of a coupled surface and internal wave above a flat bed [54, 104]. It is now known that in the case $\gamma = 0$, for any root of the dispersion relation (4.14), the corresponding value A satisfies $A > 1$ [52]. Let us first give a new, shorter proof of this result.

Theorem 4.4.1. *Let $h, h_1, k, r > 0$ be fixed, and suppose $\gamma = 0$. The dispersion relation* (4.14) *has four real roots $c_1, ..., c_4$ satisfying $c_3 < c_4 < 0 < c_2 < c_1$. For each $i = 1, ..., 4$ we have $c_i^2 < g/k$, and therefore the corresponding values of A satisfy $A > 1$.*

Proof. Let $h, h_1, k, r > 0$ be fixed and suppose $\gamma = 0$. In physical variables, this corresponds to fixed depths in both fluid layers, a fixed wavelength, and a fixed difference in the density of the fluids in the two layers. Since (4.14) is quadratic in c^2, it can be solved explicitly giving $c_3 < c_4 < 0 < c_2 < c_1$, where $c_3 = -c_1$ and $c_4 = -c_2$. In [54] Section 3.3.1, it is shown that the positive roots c_1, c_2 satisfy

$$c_2 < \sqrt{\frac{g}{k}\frac{\tanh(kh)\tanh(kh_1)}{\tanh(kh)+\tanh(kh_1)}} \quad \text{and} \quad c_1 > \max\left\{\sqrt{\frac{g}{k}\tanh(kh)}, \sqrt{\frac{g}{k}\tanh(kh_1)}\right\}.$$

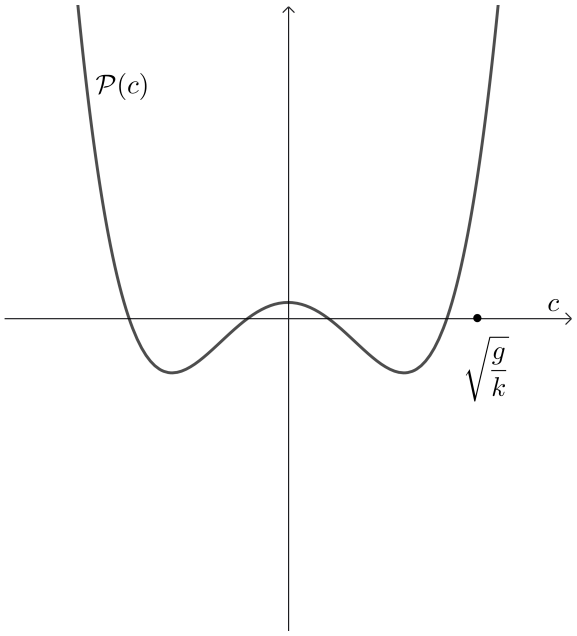

Figure 4.2: Plot of the dispersion relation $\mathcal{P}(c)$ given by (4.14) in the case $\gamma = 0$. The polynomial is quadratic in c^2 and satisfies $\mathcal{P}(\sqrt{g/k}) > 0$.

We note that since $k, h, h_1 > 0$, we have that $\tanh(kh)$, $\tanh(kh_1) \in (0, 1)$ and

$$\frac{1}{\tanh(kh)} + \frac{1}{\tanh(kh_1)} > 1.$$

It follows that

$$\frac{\tanh(kh)\tanh(kh_1)}{\tanh(kh) + \tanh(kh_1)} = \frac{1}{\frac{1}{\tanh(kh)} + \frac{1}{\tanh(kh_1)}} < 1,$$

and thus $c_2 < \sqrt{\frac{g}{k}}$. Denoting (4.14) by $\mathcal{P}(c) = 0$, it is easy to verify that

$$\mathcal{P}\left(\sqrt{\frac{g}{k}}\right) = (1 + r)\left(1 - \frac{1}{\tanh(kh)}\right)\left(1 - \frac{1}{\tanh(kh_1)}\right)\frac{g^2}{k^2} > 0.$$

So Bolzano's Theorem says that $c_1 < \sqrt{\frac{g}{k}}$, and both positive roots satisfy $c^2 < \frac{g}{k}$. But because $c_3 = -c_1$ and $c_4 = -c_2$, we see that all roots actually satisfy $c^2 < \frac{g}{k}$. Since for $\gamma = 0$ we have

$$A = \frac{g}{kc^2},$$

the fact that $A > 1$ follows immediately. □

Our next result shows that allowing nonzero vorticity in the lower layer changes this picture, thus complicating the analysis of Sections 4.5 and 4.6.

Theorem 4.4.2. *Let $h, h_1, k, r > 0$ be fixed. There exist values of $\gamma \neq 0$ such that the dispersion relation* (4.13) *has real roots, and the corresponding values of*

A can satisfy $0 < A < 1$, $A = 1$ *or* $A > 1$.

Proof. The fact that $A > 0$ for any real root of (4.13) is clear from equation (4.10). Consider the value $\mathfrak{c} = \sqrt{\frac{g}{k}}$ (recall that we have defined $\mathfrak{c} = c - \gamma h$). It is easy to check that

$$P\left(\sqrt{\frac{g}{k}}\right) = \frac{(1+r)g^2}{k^2}\left(1 - \frac{1}{\tanh(kh_1)}\right)\left(1 - \frac{1}{\tanh(kh)} - \frac{\gamma}{\sqrt{gk}}\right),$$

so we clearly have that $P\left(\sqrt{\frac{g}{k}}\right) = 0$ for $\gamma = \gamma^*$ where

$$\gamma^* = \sqrt{gk}\left(1 - \frac{1}{\tanh(kh)}\right) < 0,$$

and $P\left(\sqrt{\frac{g}{k}}\right) < 0$ for $\gamma < \gamma^*$. By equation (4.10), $A = 1$ whenever $\mathfrak{c} = \sqrt{\frac{g}{k}}$ is a root of (4.13), which by above is possible when $\gamma = \gamma^*$. When $\gamma < \gamma^*$, and thus $P\left(\sqrt{\frac{g}{k}}\right) < 0$, since $P(\mathfrak{c}) \to \infty$ as $\mathfrak{c} \to \infty$ there exists a root of (4.13) satisfying $\mathfrak{c} > \sqrt{\frac{g}{k}}$, with the corresponding value of A satisfying $A < 1$. Due to the fact $P(0) > 0$, there is also a second root satisfying $\mathfrak{c} < \sqrt{\frac{g}{k}}$, for which $A > 1$. □

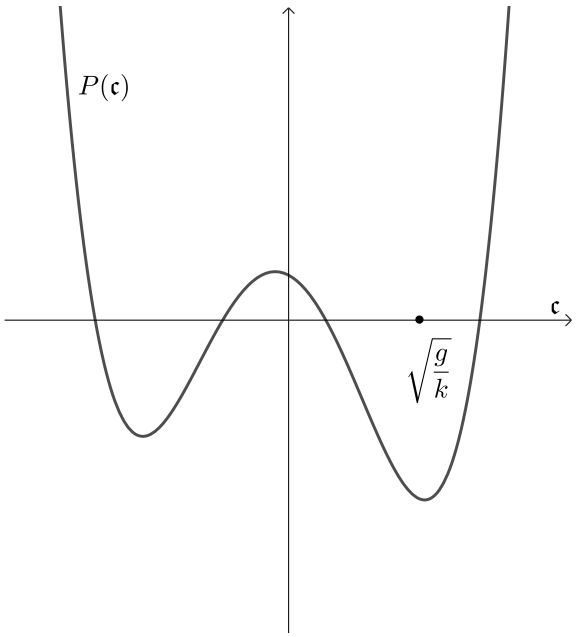

Figure 4.3: Plot of the dispersion relation $\mathcal{P}(\mathfrak{c})$ given by (4.13) with $\gamma \neq 0$ in the lower layer. In contrast to the irrotational case, $\mathcal{P}(\sqrt{g/k}) < 0$ is now possible.

4.5 Phase plane analysis

Using (4.2), (4.7), (4.8) and the linear wave Ansatz (4.6), explicit expressions for the velocity fields can be obtained. Letting $(x(t), y(t))$ denote the path of a

particle in the lower fluid layer Ω, we have that the particle's motion is described by the nonlinear nonautonomous dynamical system

$$\begin{cases} \dfrac{dx}{dt} = u(t) = ak\mathfrak{c}\dfrac{\cosh(k(y+h))}{\sinh(kh)}\cos(kx-\omega t) + \gamma(y+h), \\ \dfrac{dy}{dt} = v(t) = ak\mathfrak{c}\dfrac{\sinh(k(y+h))}{\sinh(kh)}\sin(kx-\omega t), \end{cases} \tag{4.15}$$

for $-h < y < 0$, with initial data (x_0, y_0). In the upper fluid layer Ω_1, the particle's trajectory is described by the nonlinear nonautonomous dynamical system

$$\begin{cases} \dfrac{dx}{dt} = u_1(t) = a_1k\mathfrak{c}[\sinh(k(y-h_1)) + A\cosh(k(y-h_1))]\cos(kx-\omega t) + \gamma h, \\ \dfrac{dy}{dt} = v_1(t) = a_1k\mathfrak{c}[\cosh(k(y-h_1)) + A\sinh(k(y-h_1))]\sin(kx-\omega t), \end{cases} \tag{4.16}$$

for $0 < y < h_1$, with initial data (x_0, y_0). The right hand sides of systems (4.15) and (4.16) are smooth and bounded (since y is bounded), so the existence of unique local smooth solutions is ensured by the Picard-Lindelöf theorem, and these solutions are in fact defined globally [88]. Moving forward, we shall only consider the case of right moving waves (i.e $c > 0$). From the dispersion relation (4.13), if c is a wavespeed for a fixed vorticity γ, then $-c$ will be a solution of (4.13) with vorticity $-\gamma$. So we may restrict to $c > 0$ without loss of generality. For the analysis in this section, we will further assume that $\mathfrak{c} = c - \gamma h > 0$. We can do this without losing generality since, after switching to a moving frame of reference, $\mathfrak{c} < 0$ simply corresponds to a shift of the phase portraits in the horizontal direction in the lower layer. In the upper layer, it corresponds to a reversal of the flow direction of the phase portraits, but does not substantively affect the qualitative analysis.

4.5.1 Lower layer

We make the change of variables

$$X(t) = kx(t) - \omega t, \quad Y(t) = k(y(t) + h),$$

which transforms the dynamical system (4.15) into the following nonlinear autonomous system

$$\begin{cases} \dot{X} = M\cos(X)\cosh(Y) + \gamma Y - \omega, \\ \dot{Y} = M\sin(X)\sinh(Y), \end{cases} \tag{4.17}$$

where

$$M = \frac{ak^2\mathfrak{c}}{\sinh(kh)} = \frac{a}{k}\cdot\frac{kh}{\sinh(kh)}\cdot(\omega - \gamma kh) \ll \omega,$$

except in the case of very large negative vortcity, since $\sigma < \sinh(\sigma)$ for $\sigma > 0$, and recalling that $a/h = \mathcal{O}(\epsilon) \ll 1$ by assumption. We note that system (4.17) has a Hamiltonian structure. Indeed, setting

$$F(X,Y) = M\cos(X)\sinh(Y) + \frac{\gamma}{2}Y^2 - \omega Y,$$

we see that

$$\dot{X} = \frac{\partial F}{\partial Y}, \quad \dot{Y} = -\frac{\partial F}{\partial X},$$

while the Hessian of F is given by

$$D^2F = \begin{pmatrix} -M\cos(X)\sinh(Y) & -M\sin(X)\cosh(Y) \\ -M\sin(X)\cosh(Y) & M\cos(X)\sinh(Y) + \gamma \end{pmatrix}.$$

We define the 0-isocline to be the set $\{(X,Y)|\ \dot{Y} = 0\}$, and we similarly define the ∞-isocline to be the set $\{(X,Y)|\ \dot{X} = 0\}$. Since the system (4.17) is periodic with respect to X, it is sufficient to only consider the set $\{(X,Y)|\ -\pi \leq X \leq \pi,\ 0 \leq Y \leq kh + \mathfrak{e}\cos(X)\}$, where $\mathfrak{e} = ak$ is the wave steepness parameter for the internal wave.

The Irrotational case

It will be useful to first examine our dynamical system (4.17) in the irrotational setting, that is the case $\gamma = 0$. In this case, system (4.17) reduces to

$$\begin{cases} \dot{X} = M\cos(X)\cosh(Y) - \omega, \\ \dot{Y} = M\sin(X)\sinh(Y), \end{cases} \tag{4.18}$$

a system which appears in [36] and [54]. We recall here the salient features of system (4.18), which are displayed schematically in Figure 4.4 below. The 0-isocline clearly consists of the lines $X = 0, \pm\pi$, and the line segment $Y = 0$. Since $\omega > 0$, there are no points (X,Y) in the ∞-isocline satisfying $X \in [-\pi, -\pi/2] \cup [\pi/2, \pi]$. In the region $X \in (-\frac{\pi}{2}, \frac{\pi}{2})$, the ∞-isocline is given by the curve $(X, \alpha(X))$, where $\alpha(X) \in [Y^*, \infty)$ for $\cosh(Y^*) = \omega/M$, with α defined as follows: on $[0, \frac{\pi}{2})$ set

$$\alpha(X) = \cosh^{-1}\left(\frac{\omega}{M\cos(X)}\right),\ X \in [0, \pi/2),$$

and extend it by mirror symmetry to the interval $(-\frac{\pi}{2}, \frac{\pi}{2})$. Here, $\cosh^{-1}$ denotes the positive branch of the pre-image of cosh. It is clear that α is a well-defined, smooth, even function. Furthermore, it satisfies $\lim_{X \to \pm\pi/2} \alpha(X) = \infty$, and it takes on its infimum Y^* at $X = 0$. From these considerations, we see that the only

equilibrium point of the system (4.18) is $Q = (0, Y^*)$, and Q is in fact a saddle point. Recalling that system (4.18) has a Hamiltonian structure, we see that Q is a critical point of $F(X, Y)$, and the Hessian of F, D^2F, at the point Q is given by

$$D^2F(Q) = \begin{pmatrix} -M\sinh(Y^*) & 0 \\ 0 & M\sinh(Y^*) \end{pmatrix},$$

and so Q is nondegenerate. By Morse's lemma [89], in a neighbourhood of Q there exists a diffeomorphic change of coordinates sending level sets of F to hyperbolas. Q is thus a saddle point. Now, we have that $\dot{X}(X, Y) < 0$ whenever $X \in [-\pi, -\pi/2] \cup [\pi/2, \pi]$. We also see that $\dot{X} < 0$ whenever $Y < \alpha(X)$. Any trajectory intersecting $X = 0$ below Q can be traced backwards in time to $X = \pi$, the same being true for trajectories intersecting $\alpha(X)$. Therefore there exists a separatrix separating two different types of trajectories, and connecting the line $X = \pi$ with the point Q. The separatrix consists of the points $\{(X, Y) : F(X, Y) = F(Q)\}$, and intersects the line $X = \pi$ at the point (π, β), with β implicitly defined by $F(Q) = -M\sinh(\beta) - \omega\beta$. A trajectory that intersects $X = 0$ above Q can be followed forward in time above $\alpha(X)$ and is therefore unbounded. Similarly, trajectories intersecting $\alpha(X)$ are unbounded. There is thus a second, unbounded separatrix, emerging from Q above $\alpha(X)$ and separating the trajectories intersecting $X = 0$ from those intersecting $\alpha(X)$.

To conclude our discussion, we note that in order for dynamical system (4.18) to be compatible with the physical model, we require the surface wave to lie beneath the separatrix. Since the crest is located at $(X, Y) = (0, k(a + h))$, it is enough to require that

$$k(a + h) < Y^*$$

or equivalently,

$$\frac{a}{h}\cosh(k(a + h)) < \frac{\sinh(kh)}{kh}.$$

Conditions similar to the above have arisen in [26, 54], and provide a quantifiable measure of how small the amplitude of the velocity field must be in order for linear wave solutions to exist and be physically valid.

Negative vorticity $\gamma < 0$

We now study our dynamical system (4.17) in the case $\gamma < 0$.

$$\begin{cases} \dot{X} = M\cos(X)\cosh(Y) + \gamma Y - \omega, \\ \dot{Y} = M\sin(X)\sinh(Y). \end{cases} \tag{4.19}$$

Using a comparison argument in the style of [36], we can show that the salient properties of system (4.19) are the same as those of system (4.18). Indeed, it is

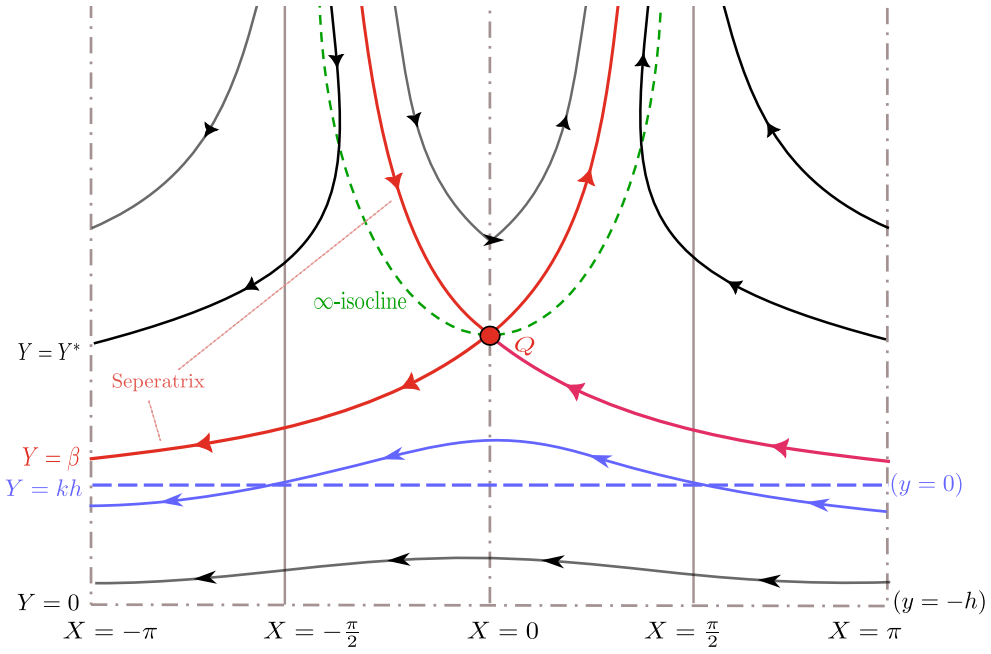

Figure 4.4: Phase portrait for the lower-fluid layer in the irrotational and negative-vorticity cases. The ∞-isocline (– – –) is shown as a dashed green line, and the 0-isoclines (– · –) as grey dot-dashed lines. The internal wave profile (——) is shown with mean water level at $y = 0$ in physical variables.

clear that the 0-isocline is unchanged from the irrotational case. At any fixed point on the phase plane with $Y > 0$, we have (where the subscripts correspond to negative vorticity and irrotationality, respectively)

$$\dot{X}_{\text{neg}} < \dot{X}_{\text{irr}},$$

and so the velocity field is conserved wherever $\dot{X}_{\text{irr}} < 0$ in the irrotational phase portrait. When it comes to the ∞-isocline, we can therefore conclude that there are no points satisfying $X \in [-\pi, -\pi/2] \cup [\pi/2, \pi]$. For fixed $X \in (-\pi/2, \pi/2)$, one observes that the map

$$Y \mapsto M \cos(X) \cosh(Y) + \gamma Y - \omega$$

is convex, negative at $Y = 0$, and goes to ∞ as $Y \to \infty$. Therefore, for each fixed $X \in (-\pi/2, \pi/2)$, there exists a unique $Y > 0$ such that (X, Y) lies on the ∞-isocline, and this unique value of Y decreases as γ decreases. We conclude that the ∞-isocline in the case $\gamma < 0$ is basically unchanged from the case $\gamma = 0$, and is given by a convex graph lying above the one for $\gamma = 0$.

Positive vorticity $\gamma > 0$

The case of positive vorticity $\gamma > 0$ is more delicate. We begin with the following

result, which we state without proof.

Lemma 4.5.1. *[36, Lemma 4.6] Let $\gamma > 0$, and suppose*

$$\frac{\gamma}{M}\sinh^{-1}\left(\frac{\gamma}{M}\right) - \sqrt{1+\left(\frac{\gamma}{M}\right)^2} - \frac{\omega}{M} > 0. \tag{4.20}$$

The ∞-isocline of (4.17) for $X \in [0,\pi]$ consists of two disjoint pairs:

(a) the graph of an increasing function $Y_a(X)$ defined for $X \in [0,\pi]$ and

(b) the graph of a decreasing function $Y_b(X)$ defined in $(\pi/2, \pi]$.

We have $Y_a(X) < Y_b(X) \to \infty$ as $X \to \frac{\pi}{2}^+$, and for any $\delta > 0$ there exists $Y^* > 0$ and a small enough amplitude a such that

$$0 < \frac{\partial Y}{\partial X} < \frac{\delta}{\pi} \quad in \quad [0,\pi] \times [Y^*, Y^* + \delta].$$

If (4.20) does not hold, then the qualitative features of dynamical system (4.17) within the fluid region are the same as the case $\gamma \leq 0$, so we shall omit the details. Suppose therefore that (4.20) is true. By symmetry, in analysing dynamical system (4.17) we may restrict to values $X \in [0,\pi]$. We begin by noting that there are three critical points, given by

$$\begin{aligned} P_1 &= (0, Y_1), \\ P_2 &= (\pi, Y_2), \\ P_3 &= (\pi, Y_3), \end{aligned}$$

where $M\cosh(Y_1) + \gamma Y_1 - \omega = 0$, and Y_2, Y_3 are the smallest and largest roots of $M\cosh(Y) - \gamma Y + \omega = 0$, respectively. In $\mathcal{R} = [0,\pi] \times [0,\infty)$ we have $\dot{Y} > 0$, while from Lemma 4.5.1 we see $\dot{X}$ is negative below $Y_a(X)$ and above $Y_b(X)$, and it is positive everywhere else in $\mathcal{R}$. Recall that dynamical system (4.17) has a Hamiltonian structure with

$$F(X,Y) = M\cos(X)\sinh(Y) + \frac{\gamma}{2}Y^2 - \omega Y.$$

We can now use Morse theory [89] to analyse the critical points P_1, P_2, P_3. Recalling that the Hessian of F is given by

$$D^2F = \begin{pmatrix} -M\cos(X)\sinh(Y) & -M\sin(X)\cosh(Y) \\ -M\sin(X)\cosh(Y) & M\cos(X)\sinh(Y) + \gamma \end{pmatrix},$$

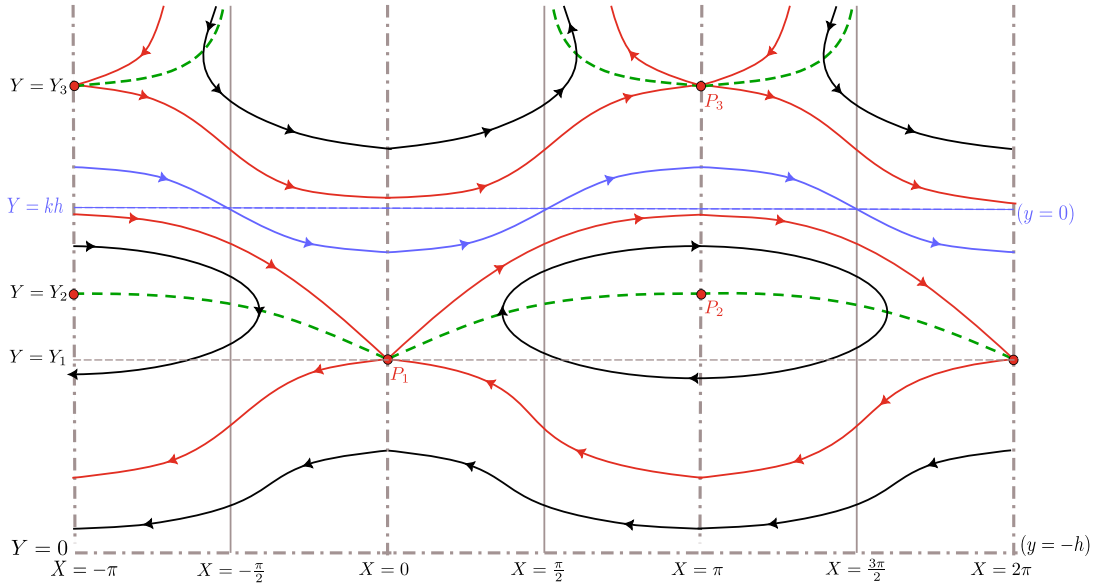

Figure 4.5: Phase portrait for the lower-fluid layer in the case of positive vorticity. The ∞-isocline (– – –) is shown as a dashed green line, and the 0-isoclines (– · –) as grey dot-dashed lines. The separatrices $\sigma_1, \ldots, \sigma_4$ (——) are shown as solid red lines, and the internal wave profile (——) is shown with mean water level at $y = 0$ in physical variables. We note the resemblance to Kelvin's cat's-eye flow.

we first observe that $D^2F(P_1)$ is diagonal with one negative and one positive eigenvalue, so Morse's Lemma [89] tells us P_1 is a saddle point. We may similarly conclude that P_2 is a centre, and that P_3 is another saddle point. This gives rise to four separatrices $\sigma_1, ..., \sigma_4$, which are trajectories demarcating regions of differing qualitative behaviours. The first, σ_1, is a trajectory which can be followed back in time from P_1 below $Y_a(X)$, connecting P_1 to $X = \pi$ below P_2. The second, σ_2, is a trajectory which can be followed forward in time from P_1 above $Y_a(X)$. σ_3 is a trajectory which can be followed back in time from P_3 below $Y_b(X)$, while σ_4 is a trajectory which starts at P_3, is above $Y_b(X)$, and encloses a family of unbounded trajectories starting from $X = \pi$ above P_3. Finally, there exists a family of trajectories starting at $X = 0$ above P_1 which reaches $X = \pi$ in finite time between P_2 and P_3.

Remark 4.5.2. If instead we assume that $\mathfrak{c} < 0$, (and therefore $M < 0$ in (4.17)), this corresponds to a horizontal shift in the phase portrait and the dynamical system has three critical points given by

$$P_1^- = (\pi, Y_1),$$
$$P_2^- = (0, Y_2),$$
$$P_3^- = (0, Y_3).$$

Furthermore, the sign of $\dot{Y}$ changes and so the flow direction is reversed vertically. Qualitatively, this phase portrait is identical to the phase portrait for $\mathfrak{c} > 0$ after it has been shifted in the horizontal direction by π, cf. Fig.4.5 and Fig.4.6.

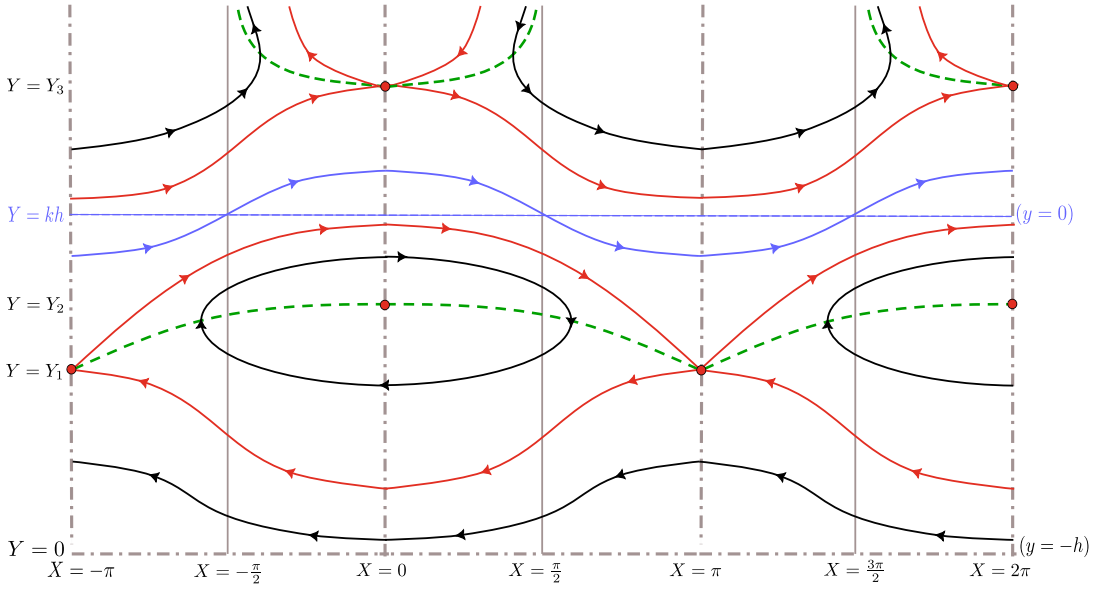

Figure 4.6: Phase portrait for the lower-fluid layer in the case $\gamma > 0$ with $\mathfrak{c} < 0$. The portrait is shifted by π along the horizontal axis relative to the $\mathfrak{c} > 0$ case, cf. Fig. 4.5.

4.5.2 Upper layer

To analyse the upper fluid layer, we make the change of variables

$$X(t) = kx(t) - \omega t, \quad Y_1(t) = k(h_1 - y(t)) \tag{4.21}$$

which transforms the dynamical system (4.16) into the following nonlinear autonomous system

$$\begin{cases} \dot{X} = a_1 k^2 \mathfrak{c}[A\cosh(Y_1) - \sinh(Y_1)]\cos(X) - k\mathfrak{c} \\ \dot{Y_1} = a_1 k^2 \mathfrak{c}[A\sinh(Y_1) - \cosh(Y_1)]\sin(X). \end{cases} \tag{4.22}$$

Note that this reverses the orientation of the vertical coordinates. The properties of dynamical system (4.22) are sensitive to the exact value of A, in particular whether or not $A < 1$, $A = 1$ or $A > 1$. As shown in Theorem 4.4.2 above, all three cases may arise provided $\gamma \neq 0$. For $\mathfrak{c} > 0$, dynamical system (4.22) was subjected to a detailed analysis in all three cases in [54], and from (4.22) it is clear that $\mathfrak{c} < 0$ simply corresponds to a reversal of the flow direction. We again stress that the investigation in [54] was concerned with the irrotational case $\gamma = 0$,

where values $A \leq 1$ do not arise as shown in Theorem 4.4.1, and $\mathfrak{c} = c > 0$. We shall therefore recall the salient features of system (4.22) here (assuming $\mathfrak{c} > 0$), and refer the reader to [54] for a full discussion. Dynamical system (4.22) once again has a Hamiltonian structure, as is easily seen by defining

$$G(X, Y_1) = a_1 k^2 \mathfrak{c}[A \sinh(Y_1) - \cosh(Y_1)] \cos(X) - k\mathfrak{c} Y_1,$$

so that

$$\dot{X} = \frac{\partial G}{\partial Y_1}, \quad \dot{Y_1} = -\frac{\partial G}{\partial X}.$$

Similar to system (4.17), since system (4.22) is periodic with respect to X, it is sufficient to confine our study to the set

$$\{(X, Y_1) |\ -\pi \leq X \leq \pi,\ -\mathfrak{e}_1 \cos(X) \leq Y_1 \leq kh_1 - \mathfrak{e} \cos(X)\},$$

where $\mathfrak{e}_1 = a_1 k$.

The case $A < 1$

When it comes to the 0-isocline of system (4.22), we note that $A \sinh(Y_1) - \cosh(Y_1) < 0$, and so the 0-isocline consists of the vertical lines $X = \{0, \pm\pi\}$. To determine the ∞-isocline, we observe that for fixed X, the function $Y_1 \mapsto A \cosh(Y_1) - \sinh(Y_1)$ is strictly decreasing and satisfies

$$\lim_{Y_1 \to \pm\infty} A \cosh(Y_1) - \sinh(Y_1) = \mp\infty.$$

By Bolzano's Theorem, for each fixed value of X there is a unique value Y_1^* satisfying

$$a_1 k^2 \mathfrak{c}[A \cosh(Y_1^*) - \sinh(Y_1^*)] \cos(X) = k\mathfrak{c},$$

and since we have $k\mathfrak{c} > 0$, we consider two cases: $X \in [-\pi, -\pi/2) \cup (\pi/2, \pi]$ and $X \in (-\pi/2, \pi/2)$, since we can clearly exclude the cases $X = \pm\frac{\pi}{2}$. For $X \in (-\pi/2, \pi/2)$, we have

$$A \cosh(Y_1^*) - \sinh(Y_1^*) = \frac{k\mathfrak{c}}{a_1 k^2 \mathfrak{c} \cos(X)} = \frac{1}{\mathfrak{e}_1 \cos(X)} > \frac{1}{\mathfrak{e}_1} \gg 1,$$

which excludes the point (X, Y_1^*) from our physical region $-\mathfrak{e}_1 \cos(X) \leq Y_1 \leq kh_1 - \mathfrak{e} \cos(X)$, since

$$A \cosh(-\mathfrak{e}_1 \cos(X)) - \sinh(-\mathfrak{e}_1 \cos(X)) \approx A + \mathfrak{e}_1.$$

For $X \in (\pi/2, \pi]$, we note that the ∞-isocline consists of a curve which tends to ∞ as $X \to \frac{\pi}{2}^+$, and has a minimum at the unique critical point for which

$X = \pi$, call it P_π^+. By symmetry, for $X \in [-\pi, \pi/2)$, the ∞-isocline consists of a curve with minimum at the unique critical point for which $X = -\pi$, call it P_π^-, and which tends to ∞ as $X \to -\frac{\pi}{2}^-$. To determine the nature of the critical points $P_\pi^\pm$, we once again appeal to Morse theory by exploiting the Hamiltonian structure of our dynamical system (4.22). Since

$$D^2G = \begin{pmatrix} -a_1k^2\mathfrak{c}[A\sinh(Y_1) - \cosh(Y_1)]\cos(X) & -a_1k^2\mathfrak{c}[A\cosh(Y_1) - \sinh(Y_1)]\sin(X) \\ -a_1k^2\mathfrak{c}[A\cosh(Y_1) - \sinh(Y_1)]\sin(X) & a_1k^2\mathfrak{c}[A\sinh(Y_1) - \cosh(Y_1)]\cos(X) \end{pmatrix},$$

we have that D^2G is diagonal at both critical points $P_\pi^\pm$, with one positive and one negative eigenvalue, and therefore both are saddle points.

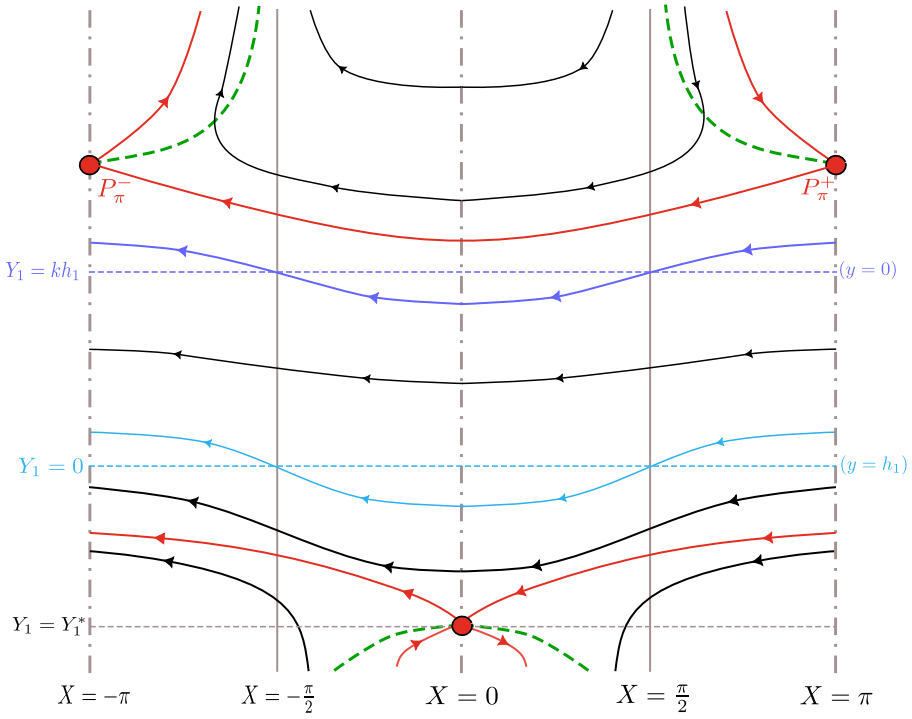

Figure 4.7: Phase portrait for the upper-fluid layer in the case $A < 1$. The ∞-isoclines (– – –) are shown as dashed green lines, and the 0-isoclines (– · –) as grey dot-dashed lines. The internal wave profile (——) is shown in dark blue with mean water level at $y = 0$, and the surface wave profile (——) in light blue with mean water level at $y = h_1$, in physical variables. Note that under the change of variables (4.21), the streamline representing the surface wave lies below that of the internal wave in the transformed variables (X, Y_1).

The case $A = 1$

In this special case, dynamical system (4.22) reduces to

$$\begin{cases} \dot{X} = a_1k^2\mathfrak{c}e^{-Y_1}\cos(X) - k\mathfrak{c}, \\ \dot{Y}_1 = -a_1k^2\mathfrak{c}e^{-Y_1}\sin(X). \end{cases}$$

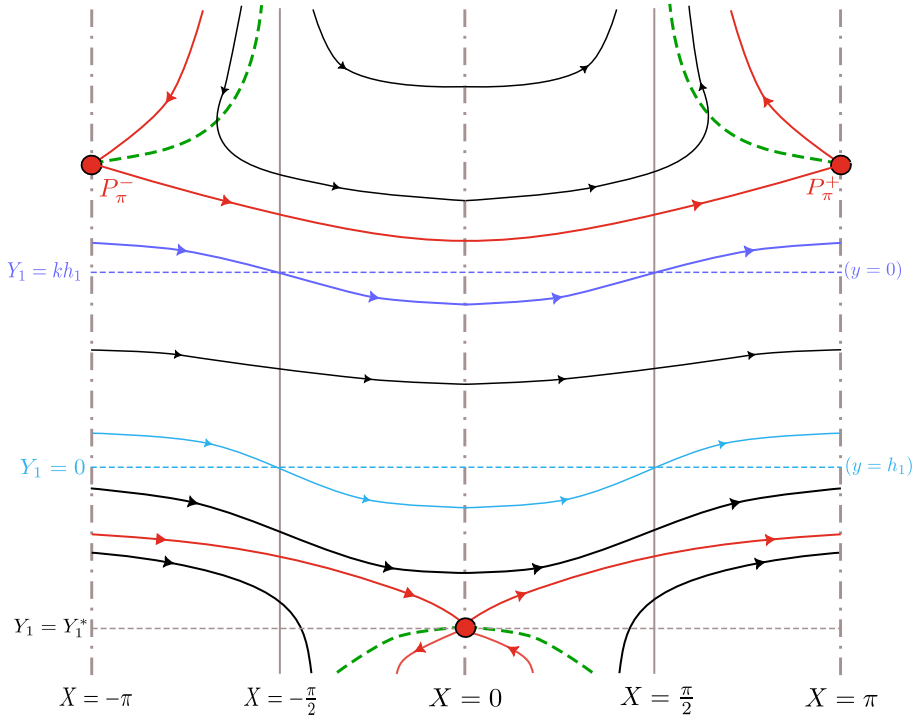

Figure 4.8: Phase portrait for the upper-fluid layer in the case $A < 1$ with $\mathfrak{c} < 0$. The flow direction is reversed relative to the $\mathfrak{c} > 0$ case, cf. Fig. 4.7.

As above, since $\sinh(Y_1) - \cosh(Y_1) < 0$, the 0-isocline consists of the vertical lines $X = \{0, \pm\pi\}$. The ∞-isocline consists of points satisfying

$$e^{-Y_1}\cos(X) = \frac{1}{\mathfrak{e}_1},$$

which clearly excludes any points for which $X \in [-\pi, -\pi/2] \cup [\pi/2, \pi]$. For every $X \in (-\pi/2, \pi/2)$, the above relation has a unique solution, but once again since $1/\mathfrak{e}_1 \gg 1$ and $-\mathfrak{e}_1\cos(X) \leq Y_1$, we are outside our physical region. It is clear that as $Y_1 > 0$ increases, the above dynamical system converges to the uniform system $\dot{X} = -k\mathfrak{c}$ and $\dot{Y}_1 = 0$, which is a series of horizontal lines.

The case $A > 1$

In the case $A > 1$, when it comes to the 0-isocline of system (4.22), we note that we no longer have $A\sinh(Y_1) - \cosh(Y_1) < 0$. The 0-isocline still contains the vertical lines $X = \{0, \pm\pi\}$, but also the horizontal line defined by $A\sinh\left(\overline{Y_1}\right) = \cosh\left(\overline{Y_1}\right)$, which is given explicitly by

$$\overline{Y_1} = \frac{1}{2}\ln\left(\frac{A+1}{A-1}\right).$$

So the 0-isocline is the union of vertical lines with a horizontal line. To study the ∞-isocline, we first note that since $A > 1$, we have that $A\cosh(Y_1) - \sinh(Y_1) > 0$,

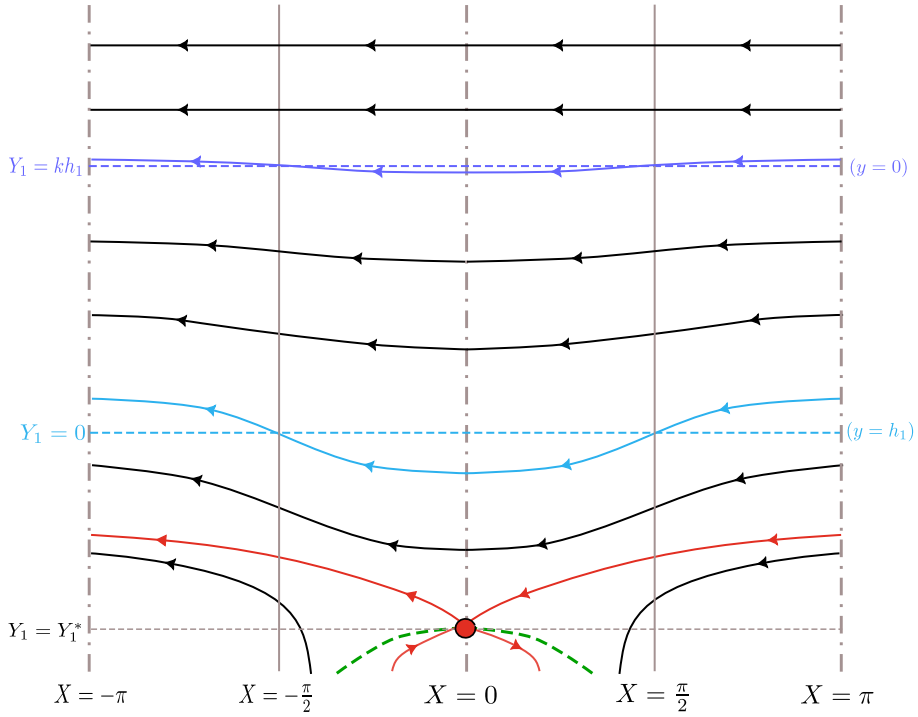

Figure 4.9: Phase portrait for the upper-fluid layer in the case $A = 1$. The ∞-isocline (– – –) is shown as a dashed green line, and the 0-isoclines (– · –) as grey dot-dashed lines. The internal wave profile (——) is shown in dark blue with mean water level at $y = 0$, and the surface wave profile (——) in light blue with mean water level at $y = h_1$, in physical variables. Note that under the change of variables (4.21), the streamline representing the surface wave lies below that of the internal wave in the transformed variables (X, Y_1).

so we can immediately exclude points satisfying $X \in [-\pi, -\pi/2] \cup [\pi/2, \pi]$. For $X \in (-\pi/2, \pi/2)$, we are looking for points satisfying

$$(A\cosh(Y_1) - \sinh(Y_1))\cos(X) = \frac{1}{\mathfrak{e}_1}.$$

For fixed $X \in (-\pi/2, \pi/2)$, the function $f(Y_1) = (A\cosh(Y_1) - \sinh(Y_1))\cos(X)$ satisfies

$$\lim_{Y_1 \to \pm\infty} f(Y_1) = +\infty,$$

and has minimum value

$$\sqrt{A^2 - 1}\cos(X),$$

with this minimum value obtained on the horizontal component of the 0-isocline. Therefore, once we have

$$\sqrt{A^2 - 1}\cos(X) \leq \frac{1}{\mathfrak{e}_1}$$

for some $X \in (-\pi/2, \pi/2)$, the ∞-isocline is non-empty. Given a value $A > 1$, if

it happens that

$$\sqrt{A^2-1}\cos(X) = \frac{1}{\mathfrak{e}_1}$$

for some value $\tilde{X} \in [0, \pi/2)$ (and therefore for $-\tilde{X}$ also), then the points

$$\left(\pm\tilde{X}, \frac{1}{2}\ln\left(\frac{A+1}{A-1}\right)\right)$$

are critical points of the system (4.22). At these points we have that $\mathrm{tr}(D^2G) = 0$ and $\det(D^2G) < 0$, so they are saddle points. If it instead happens that

$$\sqrt{A^2-1} < \frac{1}{\mathfrak{e}_1},$$

then there are no critical points with $X \neq 0$. For $X = 0$, however, there are two corresponding values $Y_1^{\pm}$ such that

$$(0, Y_1^{\pm})$$

are critical points, which are once again saddle points. We note that for physically relevant parameter values, these critical points lie outside the fluid domain.

4.6 Physical particle trajectories

When it comes to irrotational waves in the single fluid layer setting, it is by now well known that there are no closed particle trajectories, and that particles experience a slight forward drift (see [26]), which is consistent with the classical Stokes drift [102]. This was later shown to be the case for irrotational waves in the two layer setting also [54]. We will see, though, that the presence of a background current and vorticity in the lower fluid layer significantly changes this picture.

We begin by noting that the analysis of Section 4.5 can be used to infer information about the physical particle trajectories by reversing the transformations using

$$x(t) = \frac{X(t)+\omega t}{k}, \quad y(t) = \frac{Y(t)}{k} - h, \tag{4.23}$$

in the lower layer and

$$x(t) = \frac{X(t)+\omega t}{k}, \quad y(t) = h_1 - \frac{Y_1(t)}{k}, \tag{4.24}$$

in the upper layer. Next, we observe that for a physically relevant solution $(X(t), Y(t))$ of (4.17), one has $\dot{X} < 0$ at all points, while for a physically relevant solution $(X(t), Y_1(t))$ of (4.22), one has $\dot{X}\mathfrak{c} < 0$ at all points, recalling that

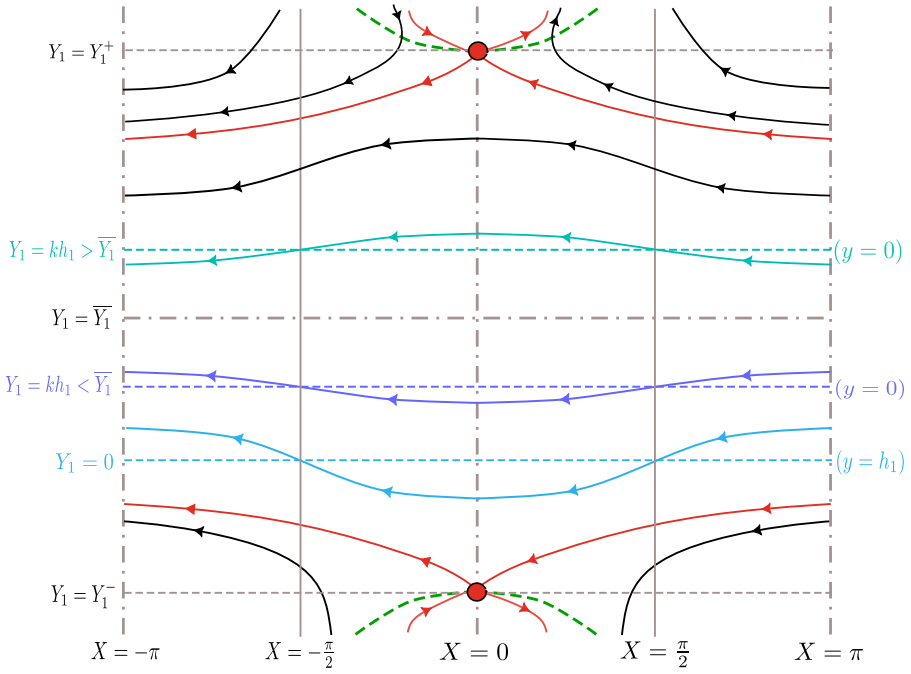

Figure 4.10: Phase portrait for the upper-fluid layer in the case $A > 1$. The ∞-isoclines (– – –) are shown as dashed green lines, and the 0-isoclines (– · –) as grey dot-dashed lines. The surface wave profile (——) is shown in light blue with mean water level at $y = h_1$. The internal wave profile is shown for two cases, both with mean water level at $y = 0$: in dark blue (——) when $Y_1 = kh_1 < \overline{Y}$, and in teal (——) when $Y_1 = kh_1 > \overline{Y}$. All profiles are shown in physical variables. Note that under the change of variables (4.21), the streamline representing the surface wave lies below that of the internal wave in the transformed variables (X, Y_1).

$\mathfrak{c} = c - \gamma h$.

Our next claim is that in the moving frame of reference, assuming we are in the regime where $\dot{X} < 0$, the time taken for a trajectory beginning at $(X(0), Y(0)) = (\pi, Y_0)$ to intersect the line $X = -\pi$ is equal to $\frac{2\pi}{\omega}$ if and only if $(x(t), y(t))$ describes a closed trajectory i.e it is a periodic solution of the governing dynamical system. We will call this time $\tau = \tau(Y_0)$. This is true in both layers, so we will only prove this in the lower layer. To see that this is true, suppose we have some solution $(X(t), Y(t))$ of (4.17) with initial data (π, Y_0) which intersects the line $X = -\pi$ at time $\tau > 0$. By symmetry, we have $Y(\tau) = Y_0$ and so $y(0) = y(\tau)$ from (4.23). Assuming that $\tau = \frac{2\pi}{\omega}$, we see from (4.23) that

$$k(x(\tau) - x(0)) = X(\tau) + 2\pi - X(0) = 0.$$

Conversely, suppose we have a periodic solution of (4.15) with period $\theta > 0$. We have that $y(0) = y(\theta)$ so that $\theta = n\tau$ for some integer $n \geq 1$, where $\tau > 0$ is the time taken for $(X(t), Y(t))$ to intersect $X = -\pi$. We thus have $X(\theta) = X(0) - 2n\pi$, and from (4.23) it easily follows from periodicity that $\tau = \frac{2\pi}{\omega}$.

From (4.24) it is clear that if $\dot{X} > 0$, then $\dot{x} > 0$ at all times, and so closed physical trajectories are not possible. This can only occur in the upper fluid layer and when $\mathfrak{c} < 0$.

4.6.1 Lower layer

In the lower fluid layer, due to the presence of vorticity, a rich variety of trajectories may occur. We begin by showing that for positive vorticity, i.e $\gamma > 0$, there are no closed particle trajectories, just like in the irrotational case $\gamma = 0$. The set of permissible trajectories is radically different than in the irrotational setting, however, and depends on the sign of $\mathfrak{c} = c - \gamma h$. The picture is even more different in the case of negative vorticity, where we shall see that closed particle trajectories can in fact occur.

Theorem 4.6.1. *If $\gamma \geq 0$, there are no closed particle paths in the lower fluid layer.*

Proof. We first assume that $\mathfrak{c} > 0$, since in this case the entire fluid region is below the lowest separatrix as described in Section 4.5. Let $(X(t), Y(t))$ be a solution of (4.17) satisfying $X(0) = \pi$ and $Y(0) = 0$, i.e the streamline is located on the flat bed. As above, let $\tau(0)$ denote the time taken for this solution to intersect the line $X = -\pi$. One then has

$$\tau(0) = \int_{-\pi}^{\pi} \frac{ds}{\omega - M\cos(s)} = 2\pi\sqrt{\frac{1}{\omega^2 - M^2}} > \frac{2\pi}{\omega},$$

recalling that $M < \omega$. So the claim holds at the flat bed, since $\tau = \frac{2\pi}{\omega}$ is a necessary and sufficient condition for closed paths to exist. Consider now a solution of (4.17) for which $X(0) = \pi$ and $Y(0) = Y_0 > 0$. The trajectory $(X(t), Y(t))$ intersects the line $X = \pi/2$ at some point $(\pi/2, Y_1)$ with $Y_1 > Y_0$. Now, if $\tilde{X}(t)$ is the unique solution of the Cauchy problem

$$\begin{cases} \dfrac{d\tilde{X}}{dt} = M\cos\Big(\tilde{X}\Big)\cosh(Y_1) - \omega, \\ \tilde{X}(0) = \pi, \end{cases}$$

we in fact have

$$X(t) \geq \tilde{X}(t) \quad \text{for } t \geq 0.$$

To see this, we note that

$$\frac{dX}{dt} = M\cos(X)\cosh(Y) + \gamma Y - \omega \geq M\cos(X)\cosh(Y_1) - \omega$$

in view of the fact the trajectory $(X(t), Y(t))$ lies below the line $Y = Y_1$ for $X \in [-\pi, -\pi/2) \cup (\pi/2, \pi]$, and lies above this line for $X \in (-\pi/2, \pi/2)$. By comparison, we have $X(t) \geq \tilde{X}(t)$ for all $t \geq 0$. It is clear therefore that $\tau(Y_0)$ is greater than or equal to the time it takes for $\tilde{X}(t)$ to reach $\tilde{X} = -\pi$. But repeating the same argument as above, we can explicitly compute this time as being greater than $\frac{2\pi}{\omega}$, and the result follows. Now suppose $\mathfrak{c} < 0$. As noted at the beginning of Section 4.5, this corresponds to a horizontal shift of the phase portraits so that the wave crest lies at $X = \pi$ instead of $X = 0$. It is now possible for parts of the fluid domain to exist above the lowest separatrix. In the part of the fluid region below the lowest separatrix, the above argument may be adapted to arrive at the same result. If we are between the lowest and second to lowest separatrices, then any trajectory $(X(t), Y(t))$ is bounded and passes $X(0) = \pi$, so we have

$$x(t) = \frac{X(t) + \omega t + X(0) - X(0)}{k} = \frac{\pi + \omega t + (X(t) - X(0))}{k},$$

where $|X(t) - X(0)| \leq \pi$. Since $\dot{X} = 0$ at P_1 and P_2, we have $\dot{x} > 0$ near these points, and so the physical particles move straight forward. Finally, if we are above the second separatrix and below the third then $\dot{X} > 0$, and so $\dot{x} > 0$ for all times $t > 0$. This finishes the proof. □

In turns out that when $\gamma \geq 0$, the horizontal drift experienced by a particle over one wave period is a strictly decreasing function of depth, as we now show. This appears to be a new observation for system (4.15) in the case of positive vorticity. The proof of this result is a straight forward adaptation of [17, Lemma 3.3], which dealt with the $\gamma = 0$ case in the infinite depth setting. See also [54, Proposition 5.3].

Theorem 4.6.2. *Let $\gamma \geq 0$. The horizontal drift experienced by a fluid particle in the lower fluid layer over one wave period is a strictly decreasing function of depth.*

Proof. Let $(X(t), Y(t))$ be a solution of (4.17) satisfying $(X(0), Y(0)) = (\pi, Y_0)$, with $Y_0 > 0$, and denote by $D(Y_0)$ the drift experienced by the corresponding fluid particle, given by

$$D(Y_0) = \frac{\tau(Y_0)\omega - 2\pi}{k},$$

where as before $\tau(Y_0)$ denotes the time taken to reach the line $X = -\pi$. Using the inverse function theorem and the implicit function theorem, we may express this drift as

$$D(Y_0) = \frac{1}{k} \int_{-\pi}^{\pi} \frac{M \cos(s) \cosh(Y) + \gamma Y}{\omega - M \cos(s) \cosh(Y) - \gamma Y} \, ds$$

where $s = X$ and $Y = Y(s)$ (implying $Y(\pi) = Y_0$ when viewed as a function of $s = X$). Consider now a sequence of streamlines $\tilde{Y}_n = \tilde{Y}_n(X)$ satisfying $\tilde{Y}_n(\pi) = Y_n$, where the initial depths Y_n satisfy $0 < Y_n < Y_0$ for all $n \geq 1$, and $\lim_{n\to\infty} Y_n = Y_0$. For any fixed $n \geq 1$ one has

$$\frac{k}{\omega}(D(Y_0)-D(Y_n)) = \int_{-\pi}^{\pi} \frac{M(\cosh(Y) - \cosh\Big(\tilde{Y}_n\Big))\cos(s) + \gamma(Y - \tilde{Y}_n)}{(\omega - M\cos(s)\cosh(Y) - \gamma Y)(\omega - M\cos(s)\cosh\Big(\tilde{Y}_n\Big) - \gamma\tilde{Y}_n)}\, ds,$$

so our goal is to show that the above expression is in fact positive. It is enough to show the above expression is positive for sufficiently large n. Using the uniqueness of solutions to system (4.17), the above integral will have the same sign as

$$\lim_{n\to\infty} \int_{-\pi}^{\pi} \frac{M(\cosh(Y) - \cosh\Big(\tilde{Y}_n\Big))\cos(s) + \gamma(Y - \tilde{Y}_n)}{(\omega - M\cos(s)\cosh(Y) - \gamma Y)(\omega - M\cos(s)\cosh\Big(\tilde{Y}_n\Big) - \gamma\tilde{Y}_n)(Y - \tilde{Y}_n)}\, ds,$$

which using Lebesgue's dominated convergence theorem and the Cauchy-Schwarz inequality we find

$$\begin{aligned}
&\lim_{n\to\infty} \int_{-\pi}^{\pi} \frac{M(\cosh(Y) - \cosh\Big(\tilde{Y}_n\Big))\cos(s) + \gamma(Y - \tilde{Y}_n)}{(\omega - M\cos(s)\cosh(Y) - \gamma Y)(\omega - M\cos(s)\cosh\Big(\tilde{Y}_n\Big) - \gamma\tilde{Y}_n)(Y - \tilde{Y}_n)}\, ds \\
&= \int_{-\pi}^{\pi} \frac{M\cos(s)\sinh(Y) + \gamma}{(\omega - M\cos(s)\cosh(Y) - \gamma Y)^2}\, ds \\
&> \gamma\frac{\tau(Y_0)^2}{2\pi} + \int_{-\pi}^{\pi} \frac{M\cos(s)\sinh(\mathcal{Y})}{(\omega - \gamma\mathcal{Y})^2}\, ds \\
&\geq 0.
\end{aligned}$$

From the above we conclude that for n sufficiently large one has $D(Y_0) > D(Y_n)$, completing the proof. □

Heuristically, the above result is not surprising. Knowing that the particle drift is a decreasing function of depth in the case $\gamma = 0$, a positive shear current which gets weaker with depth should preserve this property. Our next result, which is valid for particles near the flat bed $y = -h$, applies to all values of γ. Our next result, which is valid for particles near the flat bed $y = -h$, applies to all values of γ.

Theorem 4.6.3. *There are no closed particle paths in the lower fluid layer for particles sufficiently close to the flat bed $y = -h$, with all particles displaying a forward drift.*

Proof. At the flat bed $y = -h$, we may argue as in the proof of Theorem 4.6.1 to find $\tau(0) > \frac{2\pi}{\omega}$, and then use a continuity argument (c.f [36, Lemma 5.1]) to

conclude $\tau(Y_0) > \frac{2\pi}{\omega}$ for sufficiently small values of $Y(0) = Y_0 > 0$. □

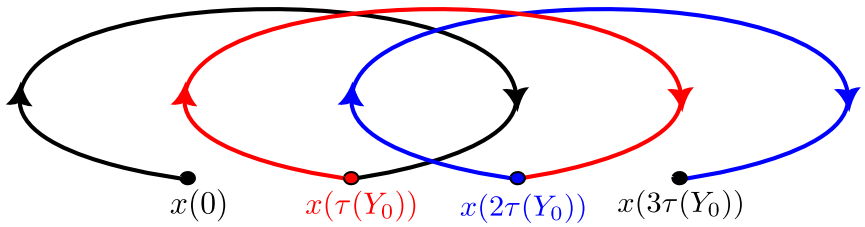

Figure 4.11: A typical particle trajectory exhibiting forward drift, arising from $\tau(Y_0) > 2\pi/\omega$.

Theorem 4.6.4. *If $\gamma < 0$ is large enough, then in the lower fluid layer closed trajectories are possible.*

Proof. From our considerations in Section 4.5, there exists a unique critical point $Q = (0, Y^*)$ of system (4.17), where Y^* satisfies

$$M\cosh(Y^*) + \gamma Y^* - \omega = 0.$$

Note that Q may lie outside the fluid domain. By continuity, for trajectories $(X(t), Y(t))$ lying close to Q, the time τ it takes to travel from $X(0) = \pi$ to $X = -\pi$ can be made arbitrarily large, and there is thus a forward drift for the corresponding trajectories $(x(t), y(t))$. For trajectories near the flat bed $y = -h$, by Theorem 4.6.3, there is always a forward drift. Let $\delta > 0$ and $0 < Y_0 < Y^*$, and suppose $a \ll 1$ is small enough to ensure

$$M\cosh(Y_0 + \delta) < \delta.$$

Suppose $\gamma < 0$ is large enough so that $-\gamma Y_0 - \delta > \pi$ and $Y^* > Y_0 + \delta$. We then have

$$\left|\frac{\partial Y}{\partial X}\right| = \left|\frac{M\sin(X)\sinh(Y)}{M\cos(X)\cosh(Y) + \gamma Y - \omega}\right| < \frac{\delta}{\pi},$$

so that using Lemma 4.5.1, a trajectory $(X(t), Y(t))$ satisfying $Y(0) = Y_0 + \delta$ remains in $[Y_0, Y_0 + \delta]$, where $\dot{X} < -\pi - \omega$. We therefore have that $\dot{x} < 0$ for the physical particle, and there is a constant negative drift. Since we can choose δ, Y_0 so that $Y_0 + \delta < k(h - a)$, we are guaranteed the existence of trajectories with a negative drift within the fluid domain. The existence of closed particle trajectories now follows by continuity. □

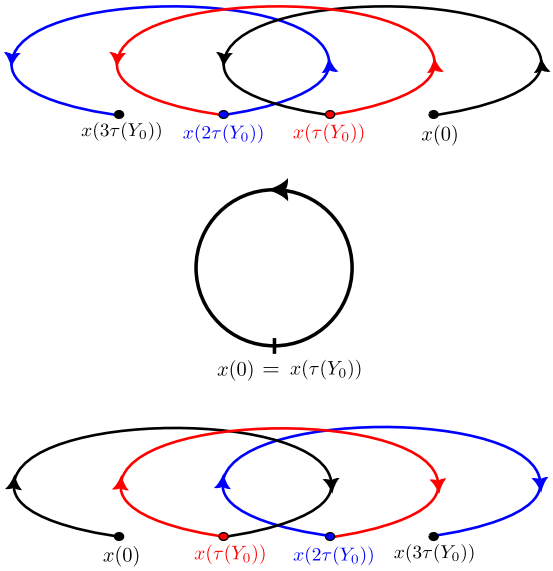

Figure 4.12: For large negative vorticity, particles may undergo negative drift, while Theorem 4.6.3 ensures that particles near the flat bed $y = -h$ undergo positive drift. By continuity there exists closed particle paths.

4.6.2 Upper layer

The picture in the upper layer is quite delicate, which it to be expected since it possesses two free boundaries. The behaviour of the physical particles is sensitive to the value of A as discussed before, but also to the sign of $\mathfrak{c} = c - \gamma h$ and the sign of γ. So even though the upper layer is irrotational, the presence of a background current drastically affects the particle behaviour. We begin by reemphasising that for $\mathfrak{c} < 0$, the assumption $\mathfrak{e}_1 \ll 1$ ensures that within the fluid domain, any solution $(X(t), Y_1(t))$ of (4.22) will satisfy $\dot{X} > 0$, which from (4.24) ensures $\dot{x} > 0$ for the corresponding physical trajectory, and so closed trajectories clearly do not occur. When it comes to the case $\mathfrak{c} > 0$, it remains true that closed trajectories exist if and only if $\tau = \frac{2\pi}{\omega}$, where like before, we define τ to be the time it takes a trajectory $(X(t), Y_1(t))$ to travel from $X(0) = \pi$ to $X = -\pi$. From (4.22) and (4.24) we see

$$\dot{x} = \frac{\dot{X} + \omega}{k} = \mathfrak{e}_1 \mathfrak{c}[A\cosh(Y_1) - \sinh(Y_1)]\cos(X) + \gamma h, \tag{4.25}$$

so if $\gamma h < 0$ and $|\gamma h|$ is large enough, then $\dot{x} < 0$ at all times, and once more closed trajectories cannot occur. In this case the particles are moving constantly backwards. Due to the complicated nature of the expression (4.25), it is difficult in general to draw strong conclusion about the sign of $\dot{x}$ in specific regions, since it may happen that $\mathfrak{e}_1 \mathfrak{c}$ and $\gamma h < 0$ are comparable in magnitude. For non-negative vorticity we have the following result.

Theorem 4.6.5. *Let $\gamma \geq 0$. Then there are no closed particle trajectories in the upper fluid layer, and the particles always experience a positive horizontal drift.*

Proof. As discussed above, when $\mathfrak{c} < 0$, we have $\dot{x} > 0$ at all points for trajectories within the fluid domain. Suppose then that $\mathfrak{c} > 0$, so that $\dot{X} < 0$ at all points. In principle, we need to consider separately the three cases $A > 1$, $A = 1$ and $A < 1$, but in all three cases the proof follows similar lines to the proof of Theorem 4.6.1.

The case $A > 1$

Recall that the fluid domain lies in the region $Y_1 \in [-\mathfrak{e}_1 \cos(X), kh_1 - \mathfrak{e}\cos(X)]$, and define

$$\overline{Y}_1 = \frac{1}{2}\ln\left(\frac{A+1}{A-1}\right).$$

We consider two cases here. First, suppose $kh_1 \leq \overline{Y}_1$, and assume we have a solution $(X(t), Y_1(t))$ of (4.22) for which $Y_1(0) < \overline{Y}_1$. In this setting the surface and internal waves are in-phase, recalling the discussion at the end of Section 4.3. We thus have that $\dot{Y}_1 < 0$ for $X \in (0, \pi)$ while $\dot{Y}_1 > 0$ for $X \in (-\pi, 0)$. Now, let $(\pi/2, \mathcal{Y}_1)$ denote the point at which the trajectory intersects the line $X = \pi/2$. Arguing in an analogous fashion to Theorem 4.6.1, we arrive at $\tau(Y_1(0)) > \frac{2\pi}{\omega}$. If it happens that $Y_1(0) = \overline{Y_1}$, then the streamline is the flat 0-isocline $Y_1 = \overline{Y_1}$, and the result still holds.

Now suppose that $kh_1 > \overline{Y}_1$. In this case, the upper fluid layer consists of two regions with qualitatively different streamlines, and the surface and internal waves are out of phase. For the region containing the free surface, the above argument applies and so $\tau(Y_1(0)) > \frac{2\pi}{\omega}$ for these streamlines. In the second region, there is a reversal in the vertical direction of motion compared to the first region, so a slight adaptation of the proof of Theorem 4.6.1 is needed, but the same conclusion follows.

The case $A = 1$

As in Section 4.5, in this special case the analysis is simplified, and we recall from Section 4.3 that the surface and internal waves are necessarily in-phase. Let $(X(t), Y_1(t))$ be a solution of (4.22) satisfying $X(0) = \pi$ and $Y_1(0) \in [\mathfrak{e}_1, kh_1 + \mathfrak{e}]$. We have

$$\begin{cases} \dot{X} = a_1 k^2 \mathfrak{c} e^{-Y_1}\cos(X) - k\mathfrak{c}, \\ \dot{Y}_1 = -a_1 k^2 \mathfrak{c} e^{-Y_1}\sin(X), \end{cases}$$

and so $\dot{Y}_1 < 0$ for $X \in (0, \pi)$ while $\dot{Y}_1 > 0$ for $X \in (-\pi, 0)$. Reusing notation from above, the trajectory $(X(t), Y_1(t))$ intersects the line $X = \pi/2$ at some point $(\pi/2, \mathcal{Y}_1)$, and the comparison argument from the proof of Theorem 4.6.1 may be

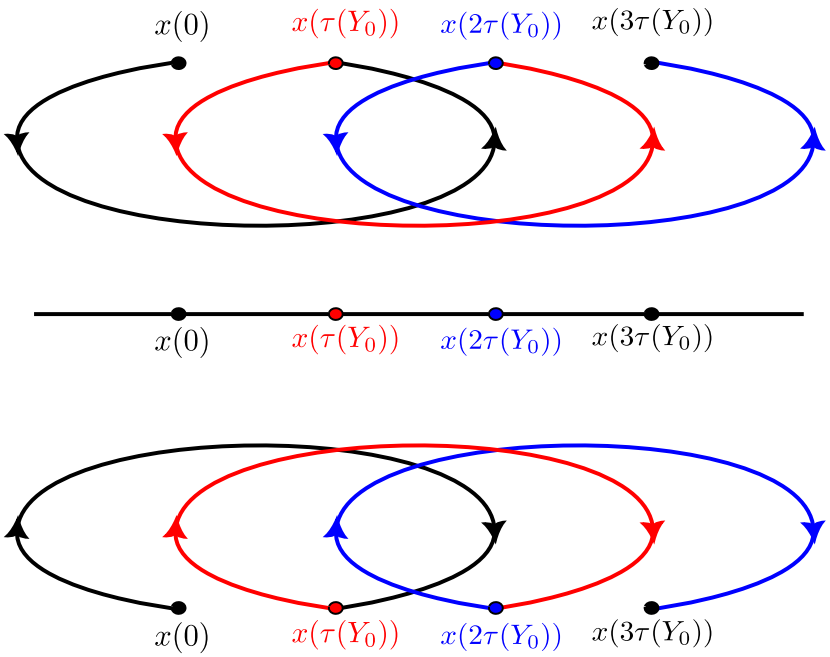

Figure 4.13: Particle trajectories for $A > 1$ in the case $kh_1 > \overline{Y}_1$.

used to conclude

$$\tau(Y_1(0)) > 2\pi\sqrt{\frac{1}{k^2\mathfrak{c}^2 - (a_1k^2\mathfrak{c}e^{-\mathcal{Y}_1})^2}} > \frac{2\pi}{k\mathfrak{c}} > \frac{2\pi}{\omega}.$$

The case $A < 1$

Once again, the surface and internal waves are necessarily in-phase, and arguing similarly to above, we can conclude that $\tau(Y_1(0)) > \frac{2\pi}{\omega}$ for each $Y_1(0) \in [\mathfrak{e}_1, kh_1 + \mathfrak{e}]$.

□

Unlike in the lower layer, the drift experienced by fluid particles in the upper fluid layer is not necessarily a monotonic function, as our next result outlines.

Theorem 4.6.6. *Let $\gamma \geq 0$.*

- *If $A > 1$, the horizontal drift experienced by a fluid particle in the upper fluid layer over one wave period decreases with depth in the region below the 0-isocline, and it increases with depth in the region above the 0-isocline. The minimum horizontal drift thus occurs at $Y_1 = \overline{Y}_1$.*
- *If $A = 1$, the horizontal drift experienced by a fluid particle in the upper fluid layer over one wave period decreases with depth.*
- *If $A < 1$, the horizontal drift experienced by a fluid particle in the upper fluid layer over one wave period decreases with depth for streamlines which*

stay below the line defined by $\tanh(Y_1) = A$*, and it increases with depth for streamlines which stay above the line defined by* $\tanh(Y_1) = A$*.*

Proof. The proof of this result follows along similar lines to the proof of Theorem 4.6.2, so we omit the full details. Alternatively we point to [54, Propositions 5.5, 5.7 and 5.9]. We only note that here, unlike in [54], one must treat the cases $\mathfrak{c} > 0$ and $\mathfrak{c} < 0$ separately, though the same conclusions follow in both cases. □

Remark 4.6.7. The comparison argument used in the proof of Theorem 4.6.5 holds even for $\gamma < 0$. The reason the entire proof does not hold in this case is that the estimate

$$\tau(Y_1(0)) > \frac{2\pi}{k\mathfrak{c}}$$

does not rule out the possibility $\tau(Y_1(0)) = \frac{2\pi}{kc}$ when $\gamma < 0$. In principle, for specified parameter values and a given initial value $Y_1(0)$, the value $\tau(Y_1(0))$ can be estimated more sharply, but a rigorous proof for all values $\gamma < 0$ is still an open problem.

As we have just seen, particles in the upper fluid layer always experience a positive horizontal drift when $\gamma \geq 0$. The shapes of the trajectories of the particles, though, are very much contingent on the values of A, $\mathfrak{c}$ and γ, as we shall now outline. Let us begin by discussing the case $\mathfrak{c} < 0$, since in this case $\dot{X} > 0$ and hence $\dot{x} > 0$ at all times for all trajectories within the fluid domain.

Suppose that $A > 1$, and consider some trajectory $(X(t), Y_1(t))$ with initial conditions $X(0) = -\pi$ and $Y_1(0) \in [\mathfrak{e}_1, kh_1 + \mathfrak{e}]$. Further assume that $kh_1 > \overline{Y}_1$. If it happens that $kh_1 \leq \overline{Y}_1$, one may simply restrict the following discussion to streamlines satisfying $Y_1(0) \in [\mathfrak{e}_1, \overline{Y}_1)$. For streamlines in this region (closest to the free surface) one has $\dot{y} > 0$ for $X(t) \in (-\pi, 0)$ and $\dot{y} < 0$ for $X(t) \in (0, \pi)$. If our trajectory lies on the 0-isocline, i.e $Y_1(0) = \overline{Y}_1$, then by definition one has $\dot{y} = 0$ at all times. For streamlines satisfying $Y_1(0) \in (\overline{Y}_1, kh_1 + \mathfrak{e}]$, one has $\dot{y} < 0$ for $X(t) \in (-\pi, 0)$ and $\dot{y} > 0$ for $X(t) \in (0, \pi)$.

In the case $A \leq 1$ the picture is simplified, and one always has $\dot{y} > 0$ for $X(t) \in (-\pi, 0)$ while $\dot{y} < 0$ for $X(t) \in (0, \pi)$.

Suppose now that $\mathfrak{c} > 0$. In this case, as discussed previously the situation is more delicate, so we further assume $\gamma h \geq 0$. Let $(X(t), Y_1(t))$ be a solution of (4.16) satisfying $X(0) = \pi$ and $Y_1(0) \in [\mathfrak{e}_1, kh_1 + \mathfrak{e}]$. We have that $\dot{X} < 0$ at all points for all trajectories within the fluid domain, but from (4.22) and (4.24) we see the sign of $\dot{x}$ is determined by the expression (4.25). If $A \geq 1$, we clearly have $\dot{x} > 0$ for $X \in (-\frac{\pi}{2}, \frac{\pi}{2})$, with $\dot{x} = \gamma h$ at $X = \pm\frac{\pi}{2}$. For $X \in (-\pi, -\frac{\pi}{2}) \cup (\frac{\pi}{2}, \pi)$, the sign of $\dot{x}$ may be positive or negative depending on the exact parameter values. It is straight forward to see that if $A \geq 1$ and $\gamma < 0$, then $\dot{x} < 0$ for

$X \in (-\pi, -\frac{\pi}{2}] \cup [\frac{\pi}{2}, \pi)$, while for $X \in (-\frac{\pi}{2}, \frac{\pi}{2})$ the exact parameter values again become important. When it comes to the case $A < 1$, the sign of $\dot{x}$ is now sensitive to whether or not Y_1 is less than or equal to $\operatorname{artanh}(A)$.

The sign of $\dot{y}$ is more straight forward, being the opposite of

$$\dot{Y}_1 = a_1 k^2 \mathfrak{c}[A \sinh(Y_1) - \cosh(Y_1)] \sin(X).$$

If $A \leq 1$, this implies $\dot{y} < 0$ for $X(t) \in (-\pi, 0)$ while $\dot{y} > 0$ for $X(t) \in (0, \pi)$.

Suppose now that $A > 1$. Further assume, again for the sake of generality, that $kh_1 > \overline{Y}_1$. For streamlines satisfying $Y_1(0) \in [\mathfrak{e}_1, \overline{Y}_1)$, we have $\dot{y} > 0$ for $X(t) \in (0, \pi)$ while $\dot{y} < 0$ for $X(t) \in (-\pi, 0)$. Particles in this region return to their lowest position after time $\tau(Y_1(0))$ having experienced a positive horizontal drift

$$x(\tau(Y_1(0))) - x(0) = \frac{\tau(Y_1(0))\omega - 2\pi}{k} > 0.$$

At the 0-isocline $Y_1 = \overline{Y}_1$ one has $\dot{y} = 0$ by definition. Particles located here experience a positive horizontal drift

$$x(\tau(\overline{Y}_1)) - x(0) = \frac{\tau(\overline{Y}_1)\omega - 2\pi}{k} > 0.$$

For streamlines satisfying $Y_1(0) \in (\overline{Y}_1, kh_1 + \mathfrak{e}]$ (near the interface) we have $\dot{y} < 0$ for $X(t) \in (0, \pi)$ while $\dot{y} > 0$ for $X(t) \in (-\pi, 0)$. Fluid particles in this region return to their highest position after time $\tau(Y_1(0))$ having experienced a positive horizontal drift $x(\tau(Y_1(0))) - x(0) = \frac{\tau(Y_1(0))\omega - 2\pi}{k} > 0$.

Chapter 5

Conclusions and future work

In Chapter 2 we constructed two new exact, nonlinear, three-dimensional Pollard-like solutions for internal waves propagating zonally on a stratified, rotating ocean in the presence of a latitudinal current. The solutions are presented in Lagrangian coordinates and the prescribed particle trajectories solve the Euler equations in the sense that a compatible pressure distribution can be derived and compatibility of the pressure across the internal interface yields an implicit expression for the dispersion relation. The presence of currents complicates the models significantly, as reflected in the dispersion relation, which now takes the form of a polynomial of degree six, in contrast to the fourth order polynomial in the case of no currents [65]. The result of this added complexity is that in both models the zonal current mediates an intrinsically nonlinear slow inertial wave mode of wave motion that is absent also from the linear theory. We also prove in the hydrostatic setting that the Lagrangian flow map is a global diffeomorphism and therefore the flow is dynamically possible.

Such exact solutions as presented in Chapter 2 are necessarily highly idealised, and require restrictive prescriptions on the flow, but their value lies in the analytical tractability that they afford. They may provide a rigorous starting point from which more physically realistic flows can be investigated, whether through perturbative analysis, the inclusion of additional physical effects, or numerical computation seeded by the analytical solution. The explicit Lagrangian description inherent to the Gerstner framework further offers direct access to particle trajectories and material surfaces, information which is often obscured in Eulerian formulations and of considerable physical relevance.

In Chapter 3 we extended a recently derived exact solution modelling nonlinear atmospheric mountain waves to a moist atmosphere. We recast the governing equations into a form compatible with the presence of water vapour in the air and the latent heat released as this vapour changes phase either to liquid through precipitation or to ice through deposition. The pressure distribution is derived in

two distinct ways; first from the Euler equations and the detailed dynamics prescribed in the Lagrangian framework and second, using the Clausius-Clapeyron and the specific temperature dependent enthalpy of the phase transition. Compatibility between these pressure distributions leads us to an explicit description of the temperature throughout the saturated atmospheric domain.

One possible avenue for future research would be to adapt the moist atmosphere analysis and associated enthalpy effects presented here to a recently derived linear, Helmholtz-type formulation of mountain waves, in which trapped lee waves emerge alongside vertically propagating ones [27]. This framework has been rigorously analysed in the context of a dry atmosphere, and the incorporation of precipitating moisture is currently in the early stages of investigation.

In Chapter 4 we studied the flow generated by coupled surface and internal small amplitude water waves in a stably stratified two layer ocean configuration in which the lower layer has a constant non-zero vorticity, while the upper layer is irrotational. We linearise the equations through means of a classical linearisation procedure, and reformulate the problem into a Hamiltonian framework using variational techniques. It transpires that although the equations of motion have been linearised, the resulting dynamical systems that govern the fluid motion are nonlinear. We then obtain a detailed Eulerian description of the underlying kinematics for the linear travelling waves, and establish a qualitative picture of individual particle motion through a Lagrangian analysis of the relevant nonlinear dynamical systems.

We anticipate that in the course of future work the results for a stably stratified ocean model where vorticity is absent from the upper layer, might be extended to the case of non-zero piecewise constant vorticity throughout both upper and lower layers. Another potential avenue of study would be the consideration of the flow underlying a single, continuously stratified fluid layer with vorticity.

Bibliography

[1] M.H.P. Ambaum. Thermal Physics of the Atmosphere. In *Advancing Weather and Climate Science*, volume 1. Wiley, 2010.

[2] P. Atkins. *The Laws of Thermodynamics: A Very Short Introduction*. Oxford Press, Oxford, 2010.

[3] A. Barcilon and D. Fitzjarrald. A nonlinear steady model for moist hydrostatic mountain waves. *Journal of the Atmospheric Sciences*, 42:58–67, 1985.

[4] G.K. Batchelor. *An Introduction to Fluid Dynamics*. Cambridge Mathematical Library. Cambridge University Press, Cambridge, 2000.

[5] A. Bennett. *Lagrangian Fluid Dynamics*. Cambridge University Press, Cambridge, 2006.

[6] D. Bolton. The computation of equivalent potential temperature. *Monthly Weather Review*, 108:1046–1053, 1980.

[7] M. Bramberger, A. Dörnbrack, H. Wilms, S. Gemsa, K. Raynor, and R. Sharman. Vertically Propagating Mountain Waves—A Hazard for High-Flying Aircraft? *Journal of Applied Meteorology and Climatology*, 57(9):1957–1975, 2018.

[8] F. Bretherton. Momentum transport by gravity waves. *Quarterly Journal of the Royal Meteorological Society*, 95(404):213–243, 1969.

[9] W. Brutsaert. Evaporation Into the Atmosphere: Theory, History, and Applications. *Environmental Fluid Mechanics*, 1, 1982.

[10] A. Constantin. Edge waves along a sloping beach. *Journal of Physics A: Mathematical and Theoretical*, 34:9723, 2001.

[11] A. Constantin. The trajectories of particles in stokes waves. *Inventiones mathematicae*, 166(3):523–535, 2006.

[12] A. Constantin. Nonlinear Water Waves with Applications to Wave-Current Interactions and Tsunamis. *Society for Industrial and Applied Mathematics, Philadelphia*, 2011.

[13] A. Constantin. An exact solution for Equatorially trapped waves. *Journal of Geophysical Research: Oceans*, 117:C05029, 2012.

[14] A. Constantin. Some three-dimensional nonlinear Equatorial flows. *Journal of Physical Oceanography*, 43:165–175, 2013.

[15] A. Constantin. Some nonlinear, Equatorially trapped, nonhydrostatic internal geophysical waves. *Journal of Physical Oceanography*, 44:781–789, 2014.

[16] A. Constantin. Exact nonlinear mountain waves propagating upwards. *Journal of Physics A: Mathematical and Theoretical*, 56:245702, 2023.

[17] A. Constantin, M. Ehrnström, and G. Villari. Particle trajectories in linear deep-water waves. *Nonlinear Anal. Real World Appl.*, 9(4):1336–1344, 2008.

[18] A. Constantin and P. Germain. Instability of some equatorially trapped waves. *Journal of Geophysical Research: Oceans*, 118, 2802, 2013.

[19] A. Constantin and R. I. Ivanov. Equatorial wave-current interactions. *Comm. Math. Phys.*, 370(1):1–48, 2019.

[20] A. Constantin and R.I. Ivanov. A Hamiltonian approach to wave-current interactions in two-layer fluids. *Physics of Fluids*, 27(8):086603, 2015.

[21] A. Constantin, R.I. Ivanov, and C.I. Martin. Hamiltonian Formulation for Wave-Current Interactions in Stratified Rotational Flows. *Archive for Rational Mechanics and Analysis*, 221(3):1417–1447, 2016.

[22] A. Constantin and R.S. Johnson. An exact, steady, purely azimuthal flow as a model for the Antarctic Circumpolar Current. *Journal of Physical Oceanography*, 46:3585–3594, 2016.

[23] A. Constantin and R.S. Johnson. On the propagation of nonlinear waves in the atmosphere. *Proceedings of the Royal Society A: Mathematical, Physical and Engineering Sciences*, 478(2260), 2022.

[24] A. Constantin and R.S. Johnson. Nonlinear Atmospheric Flow Patterns Confined to Zonal Cloud Bands. *Journal of the Atmospheric Sciences*, 82(1):3–15, 2025.

[25] A. Constantin and S.G. Monismith. Gerstner waves in the presence of mean currents and rotation. *Journal of Fluid Mechanics*, 820:511–528, 2017.

[26] A. Constantin and G. Villari. Particle trajectories in linear water waves. *J. Math. Fluid Mech.*, 10(1):1–18, 2008.

[27] A. Constantin and J. Weber. On the propagation of mountain waves: Linear theory. *Differential and Integral Equations*, 39(7-8):457–495, 2026.

[28] R.M. Corless, G.H. Gonnet, D.E.G. Hare, D.J. Jeffrey, and E. Knuth. On the Lambert W function. *Advances in Computational Mathematics*, 5:329–359, 1996.

[29] J.A. Curry and P.J. Webster. Thermodynamics of Atmospheres and Oceans. *International Geophysics Series*, 65, 1999.

[30] B. Cushman-Roisin and J.M. Beckers. *Introduction to Geophysical Fluid Dynamics. Physical and Numerical Aspects*, volume 101. Academic Press, 2010.

[31] J.M.K. Dake. Evaporative cooling of a body of water. *Water Resources Research*, 8:1087–1091, 1972.

[32] J.D. Doyle and D.R. Durran. The Dynamics of Mountain-Wave-Induced Rotors. *Journal of the Atmospheric Sciences*, 59(2):186–201, 2002.

[33] D.R. Durran. Mountain meteorology | Lee Waves and Mountain Waves. In G.R. North, J. Pyle, and F. Zhang, editors, *Encyclopedia of Atmospheric Sciences*, pages 95–102. Academic Press, Oxford, 2nd edition, 2015.

[34] D.R. Durran and J.B. Klemp. The effects of moisture on trapped mountain lee waves. *Journal of the Atmospheric Sciences*, 39:2490–2506, 1982.

[35] D.R. Durran and J.B. Klemp. On the effects of moisture on the Brunt-Väisälä frequency. *Journal of the Atmospheric Sciences*, 39:2152–2158, 1982.

[36] M. Ehrnström and G. Villari. Linear water waves with vorticity: rotational features and particle paths. *J. Differential Equations*, 244(8):1888–1909, 2008.

[37] V.W. Ekman. On dead water. In F. Nansen, editor, *The Norwegian North Polar Expedition 1893–1896, Scientific Results*, volume 5, pages 1–152. Longmans, Green and Co., Christiania, 1904.

[38] A.V. Fedorov and J.N. Brown. Equatorial waves. In *Encyclopedia of Ocean Sciences*, pages 3679–3695,. Academic Press, 2009.

[39] F. Genoud and D. Henry. Instability of equatorial water waves with an underlying current. *Journal of Mathematical Fluid Mechanics*, 16:661–667, 2014.

[40] F. Gerstner. Theorie der Wellen. *Annalen der Physik*, 32:412–445, 1809.

[41] A.E. Gill. Atmosphere-Ocean Dynamics. *International Geophysics Series*, 30, 1982.

[42] I.G. Gradshteyn and I.M Ryzhik. *Table of Integrals, Series, and Products*. Academic Press, Boston, 8th edition, 2015.

[43] M.V. Guarino, M.A.C. Teixeira, and M.H.P. Ambaum. Turbulence generation by mountain wave breaking in flows with directional wind shear. *Quarterly Journal of the Royal Meteorological Society*, 142(700):2715–2726, 2016.

[44] S.V. Haziot and K. Marynets. Applying the stereographicprojection to modeling of the flow of the Antarctic Circumpolar Current. *Oceanography*, 31:68–75, 2018.

[45] B. Henderson-Sellers. A new formula for latent heat of vaporization of water as a function of temperature. *Quarterly Journal of the Royal Meteorological Society*, 110:1186–1190, 1984.

[46] D. Henry. On gerstner's water wave. *Journal of Nonlinear Mathematical Physics*, 15(Suppl 2):87–95, 2008.

[47] D. Henry. An exact solution for Equatorial geophysical water waves with an underlying current. *European Journal of Mechanics, B/Fluids*, 38:18–21, 2013.

[48] D. Henry. Internal equatorial water waves in the f-plane. *Journal of Nonlinear Mathematical Physics*, 22:499–506, 2015.

[49] D. Henry. Equatorially trapped nonlinear water waves in a β-plane approximation with centripetal forces. *Journal of Fluid Mechanics*, 804:1–11, 2016.

[50] D. Henry. Exact solutions modelling nonlinear atmospheric gravity waves. *Journal of Mathematical Fluid Mechanics*, 26, 6, 2023.

[51] D. Henry, R.I. Ivanov, and Z.N. Sakellaris. Rotational flow underlying coupled surface and internal waves. i: Eulerian perspective. *Journal of Differential Equations*, 453:113871, 2026.

[52] D. Henry, R.I. Ivanov, and G. Villari. Flow kinematics for equatorial coupled surface and internal waves. *Differential Integral Equations*, 39(7-8):511–542, 2026.

[53] D. Henry and T. Lyons. Pollard waves with underlying currents. *Proceedings of the American Mathematical Society*, 149:1175–1188, 2021.

[54] D. Henry and G. Villari. Flow underlying coupled surface and internal waves. *Journal of Differential Equations*, 310:404–442, 2022.

[55] D. Henry and G. Villari. Flow dynamics for coupled surface and internal deep-water waves. *Ann. Mat. Pura Appl. (4)*, 202(2):711–736, 2023.

[56] J.R. Holton. The role of gravity wave induced drag and diffusion in the momentum budget of the mesosphere. *Journal of the Atmospheric Sciences*, 39:791–799, 1982.

[57] J.R. Holton and G.J. Hakim. *An Introduction to Dynamic Meteorology*. Academic Press, Boston, 2012.

[58] R.A. Horn and C.R. Johnson. *Matrix Analysis*. Cambridge University Press, 1st edition, 1985.

[59] H.-C. Hsu. An exact solution for nonlinear internal Equatorial waves in the f-plane approximation. *Journal of Mathematical Fluid Mechanics*, 16:463–471, 2014.

[60] D. Ionescu-Kruse. On Pollard's wave solution at the equator. *Journal of Nonlinear Mathematical Physics*, 22:523–530, 2015.

[61] D. Ionescu-Kruse. Instability of Pollard's exact solution for geophysical ocean flows. *Physics of Fluids*, 28(086601), 2016.

[62] D. Ionescu-Kruse. On the short-wavelength stabilities of some geophysical flows. *Philosophical Transactions of the Royal Society A: Mathematical, Physical and Engineering Sciences*, 376(2111):20170090, 2017.

[63] R.S. Johnson. *A modern introduction to the mathematical theory of water waves*. Number 19. Cambridge university press, 1997.

[64] M. Kluczek. Exact and explicit internal equatorial water waves with underlying currents. *Journal of Mathematical Fluid Mechanics*, 19:305–314, 2017.

[65] M. Kluczek. Exact Pollard-like internal water waves. *Journal of Nonlinear Mathematical Physics*, 26:133–146, 2019.

[66] M. Kluczek. Nonhydrostatic Pollard-like internal geophysical waves. *Discrete and Continuous Dynamical Systems*, 39:5171–5183, 2019.

[67] M. Kluczek and A. Rodríguez-Sanjurjo. Global Diffeomorphism of the Lagrangian Flow-map for a Pollard-like Internal Water Wave. In D. Henry, K. Kalimeris, E.I. Părău, J.M. Vanden-Broeck, and E. Wahlén, editors, *Nonlinear Water Waves*, pages 19–34. Springer International Publishing, Cham, 2019. Series Title: Tutorials, Schools, and Workshops in the Mathematical Sciences.

[68] M. Kluczek and R. Stuhlmeier. Mass transport for Pollard waves. *Applicable Analysis*, 101:984–993, 2020.

[69] D. Lamb and J. Verlinde. *Physics and Chemistry of Clouds*. Cambridge University Press, Cambridge, 2011.

[70] K.G. Lamb. Internal wave breaking and dissipation mechanisms on the continental slope/shelf. *Annual Review of Fluid Mechanics*, 46(1):231–254, 2014.

[71] R.J. List. Smithsonian meteorological tables. *Smithsonian Miscellaneous Collections*, 114:1–527, 1951.

[72] T. Lyons. Particle trajectories in extreme Stokes waves over infinite depth. *Discrete Contin. Dyn. Syst.*, 34(8):3095–3107, 2014.

[73] T. Lyons. Geophysical internal equatorial waves of extreme form. *Discrete and Continuous Dynamical Systems*, 39:4471–4486, 2019.

[74] T. Lyons. Nonlinear mountain waves with active precipitation. Nonlin. *Nonlinear Analysis: Real World Applications*, 85, 104351, 2025.

[75] T. Lyons and J. McCarney. Temperature dependent precipitation in exact nonlinear mountain waves. *Journal of Mathematical Fluid Mechanics*, 27(41), 2025.

[76] T. Lyons and J. McCarney. Nonlinear temperature-dependent enthalpies in exact nonlinear mountain wave. *Differential and Integral Equations*, 39(7-8):589–608, 2026.

[77] S. Manabe and R.T. Wetherald. Thermal equilibrium of the atmosphere with a given distribution of relative humidity. *Journal of the Atmospheric Sciences*, 24:241–259, 1967.

[78] C.I. Martin. Dynamics of the thermocline in the equatorial region of the pacific ocean. *Journal of Nonlinear Mathematical Physics*, 22:516–522, 2015.

[79] C.I. Martin and R. Quirchmayr. Explicit and exact solutions concerning the Antarctic Circumpolar Current with variable density in spherical coordinates. *Journal of Mathematical Physics*, 60(101505), 2019.

[80] C.I. Martin and R. Quirchmayr. Exact solutions and internal waves for the Antarctic Circumpolar Current in spherical coordinates. *Studies in Applied Mathematics*, 148:1021–1039, 2022.

[81] A.V. Matioc. An exact solution for geophysical equatorial edge waves over a sloping beach. *Journal of Physics A: Mathematical and Theoretical*, 45(365501), 2012.

[82] A.V. Matioc. Exact geophysical waves in stratified fluids. *Applicable Analysis*, 92:2254–2261, 2013.

[83] A.V. Matioc. On the particle motion in geophysical deep water waves traveling over uniform currents. *Quarterly of Applied Mathematics*, 72(3):455–469, 2014.

[84] A.V. Matioc and B.V. Matioc. On periodic water waves with coriolis effects and isobaric streamlines. *Journal of Nonlinear Mathematical Physics*, 19(Suppl 1):89–103, 2012.

[85] J. McCarney. Exact internal waves in the presence of mean currents and rotation. *Journal of Mathematical Physics*, 64(7):073101, 2023.

[86] J. McCarney. Nonhydrostatic internal waves in the presence of mean currents and rotation. *Journal of Mathematical Physics*, 65(4):043101, 2024.

[87] D.H. McIntosh and A.S. Thom. Essentials of Meteorology. *Wykeham Science Series*, 3, 1969.

[88] J.D. Meiss. *Differential dynamical systems*. SIAM, 2007.

[89] J.W. Milnor. *Morse theory*. Number 51. Princeton university press, 1963.

[90] E. Mollo-Christensen. Gravitational and geostrophic billows: Some exact solutions. *Journal of the Atmospheric Sciences*, 35:1395–1398, 1978.

[91] D.M. Murphy and T. Koop. Review of the vapour pressures of ice and supercooled water for atmospheric applications. *Quarterly Journal of the Royal Meteorological Society*, 131:1539–1565, 2005.

[92] T.N. Palmer, G.J. Shutts, and R. Swinbank. Alleviation of a systematic westerly bias in general circulation and numerical weather prediction models through an orographic gravity wave drag parametrization. *Quarterly Journal of the Royal Meteorological Society*, 112:1001–1039, 1986.

[93] R.T. Pollard. Surface waves with rotation: An exact solution. *Journal of Geophysical Research*, 75:5895–5898, 1970.

[94] P. Queney. The problem of air flow over mountains: A summary of theoretical studies. *Bull. Amer. Meteor. Soc*, 29:16–26, 1948.

[95] R. Quirchmayr. A steady, purely azimuthal flow model for the Antarctic Circumpolar Current. *Monatshefte fur Mathematik*, 187:565–572, 2018.

[96] A. Rodríguez-Sanjurjo. Global diffeomorphism of the Lagrangian flow-map for Pollard-like solutions. *Annali di Matematica Pura ed Applicata (1923 -)*, 197(6):1787–1797, 2018.

[97] A. Rodríguez-Sanjurjo. Internal equatorial water waves and wave–current interactions in the f-plane. *Monatshefte fur Mathematik*, 186:685–701, 2018.

[98] A. Rodríguez-Sanjurjo and M. Kluczek. Mean flow properties for equatorially trapped internal water wave–current interactions. *Applicable Analysis*, 96:2333–2345, 2017.

[99] H. Rothe, E. *Introduction to Various Aspects of Degree Theory*. American Mathematical Society, 1986.

[100] R.B. Smith. Hydrostatic airflow over mountains. In *Advances in Geophysics*, volume 31, pages 1–41. Elsevier, 1989.

[101] R.B. Smith. 100 years of progress on mountain meteorology research. *Meteorological Monographs*, 59(20):– 20 73,, 2019.

[102] G.G. Stokes. On the theory of oscillatory waves. *Transactions of the Cambridge Philosophical Society*, 8:441–455, 1847.

[103] R. Stuhlmeier. Internal Gerstner waves: applications to dead water. *Applicable Analysis*, 93:1451–1457, 2014.

[104] B. R Sutherland. *Internal gravity waves*. Cambridge university press, 2010.

[105] M.A.C. Teixeira. The physics of orographic gravity wave drag. *Frontiers in Physics*, 2, 2014.

[106] G.K. Vallis. *Atmospheric and Oceanic Fluid Dynamics: Fundamentals and Large-Scale Circulation*. Cambridge University Press, Cambridge, 2nd edition, 2017.

[107] J.M. Wallace and P.V. Hobbs. *Atmospheric Science: An Introductory Survey*, volume 92. Elsevier Academic Press, Amsterdam, 2nd edition, 2006.

[108] C. Zhang, L. Spanu, and G. Galli. Entropy of liquid water from ab initio molecular dynamics. *Journal of Physical Chemistry B*, 115:14190–14195, 2011.